

X-RAY ABSORPTION METHODS FOR THE MOLECULAR CHARACTERIZATION OF CATALYST SYNTHESIS

J. R. Regalbuto¹, J. T. Miller², and A. J. Kropf³

¹Dept. of Chem. Eng., U. of Illinois at Chicago, 810 S. Clinton Street, Chicago, IL 60607

²BP Research Center, E-1F, 150 W. Warrenville Rd., Naperville, IL 60563

³Argonne National Laboratory, CMT, 9700 Cass Ave., Argonne, IL 60439

Introduction

Often heard in the field of catalysis is the call to “transform the art of catalyst characterization into a science.” State of the art x-ray absorption techniques at the Advanced Photon Source (APS) at Argonne National Laboratory are precisely the tools for molecular-level characterization that make this transformation possible. The brilliance of the APS permits analysis of solutions and solid samples at previously unattainable dilutions and speed. The use of x-ray absorption methods at the APS for catalyst characterization has been reviewed recently [1].

In this paper extended x-ray absorption fine structure (EXAFS) and x-ray absorption near edge structure (XANES) analysis have been used to achieve new insight into the synthesis of supported Pt catalysts. Three veins of work will be discussed; in the first, EXAFS was performed on solutions of chloroplatinic acid (H_2PtCl_6) to better understand the speciation pathway of this hydrolyzable coordination complex [2]. Changes in the Pt coordination sphere that occurred as the Pt complexes were adsorbed over alumina were used to postulate the mechanism of adsorption. In a second vein, in-situ, real time XANES has been used to distinguish a slow chemical reduction of adsorbed Pt(IV) complexes on carbon supports from rapid physical adsorption [3]. In a final example, EXAFS and XANES have been used to track the evolution of the Pt phase after calcination at different temperatures and to estimate final Pt crystallite size as complexes of Pt tetraammine adsorbed onto silica are converted to Pt metal crystallites by various calcination and reduction treatments [4]. From this data a mechanism for the control of Pt crystallite size has been proposed.

Experimental

EXAFS measurements were performed at the MRCAT undulator beam-line equipped with a double-crystal Si (111) monochromator with resolution of better than 4 eV at 11.5 keV (Pt L_3 edge). Spectra of the metal solutions contained in plastic cuvettes were taken in fluorescence mode and those of solids as pressed powders in transmission mode. Phase-shift and backscattering amplitudes were obtained from various solid reference compounds. Details of the experimental and fitting procedures can be found in references [2-4]. Typical data and fitted Fourier transform are shown in figure 1 for a 200 ppm CPA solution.

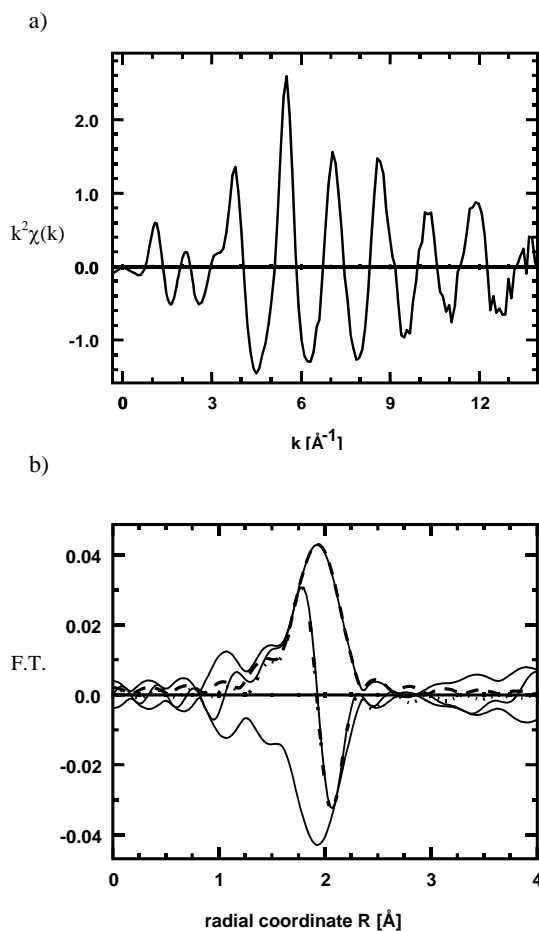


Figure 1. EXAFS data for 200 ppm CPA at pH = 1.5 HCl; a) raw EXAFS, b) typical fit (data-solid and fit-dashed; k^2 : $\Delta k = 3.0$ -10.7, $\Delta r = 1.0$ -2.7), from [2].

Chloroplatinic acid (CPA) and platinum tetraammine (PTA) chloride were used as Pt sources. Supports were common varieties of γ -alumina, amorphous silica, and activated carbon. The pH of impregnating solutions was adjusted with HCl and NaOH.

Results and Discussion

CPA Speciation in Solution and Adsorbed on Alumina.

Chloroplatinic acid is normally considered to be a strong acid with the Pt present as the hexachloroplatinate anion. It was found that when diluted to 200 ppm, hydrolysis occurs quickly and extensively [2]. The EXAFS spectra in Figure 2 clearly reveal the differences in 200 ppm CPA at the various conditions. The fits of the Pt coordination geometry are consistent with octahedral coordination, thus at a pH of 1.5 in HCl, CPA is present at PtCl_6^{2-} , while at a pH of 12, the average Pt coordination is 1.8 Pt-Cl and 4.2 Pt-O bonds. At its “natural” diluted pH of 2.6, the calculated average coordination is 2.7 Cl^- and 3.3 OH or H_2O ligands. From EXAFS it is not possible to distinguish between Pt-OH and Pt-OH₂ ligands.

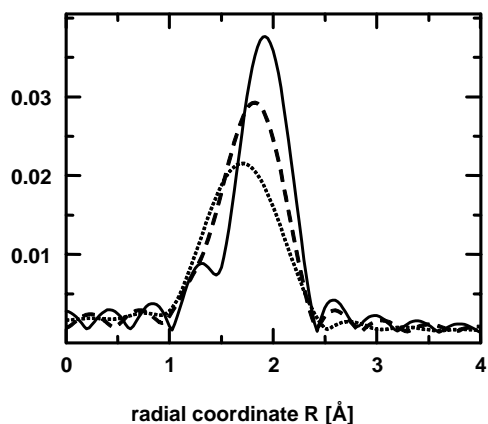


Figure 2. EXAFS of Pt coordination sphere in 200 ppm solutions: solid-CPA at pH=1.5 in HCl (k^2 : $\Delta k = 3.0$ -10.7, $\Delta r = 1.0$ -2.7); dashed-CPA at pH=2.6 as diluted (k^2 : $\Delta k = 3.0$ -10.0, $\Delta r = 1.0$ -2.4); dotted-CPA at pH=12.5 in NaOH (k^2 : $\Delta k = 3.0$ -8.6, $\Delta r = 1.0$ -2.4). From [2].

Fresh and aged 200 ppm CPA solutions were analyzed and their Pt-Cl coordination numbers (CNs) are shown in figure 3 as a function of pH [5]. This data reveals that extensive and rapid hydrolysis occurs above a pH of 2, and continues slowly over time. Also shown on this plot are the Pt-Cl CNs of Pt complexes adsorbed onto alumina. These are plotted at the calculated pH of the adsorption plane [5]. Half these samples began as fully chlorided complexes using an excess of 0.03 M NaCl (filled squares), the others as the half-chlorine, half-oxygen complexes of the diluted CPA (unfilled squares). Both series of samples fall closely together between curves of the fresh and aged liquid phase samples. Our hypothesis is that at the adsorption plane, little chloride is present (the dianionic Pt complexes adsorb much more strongly) and the pH is higher than the bulk, so the

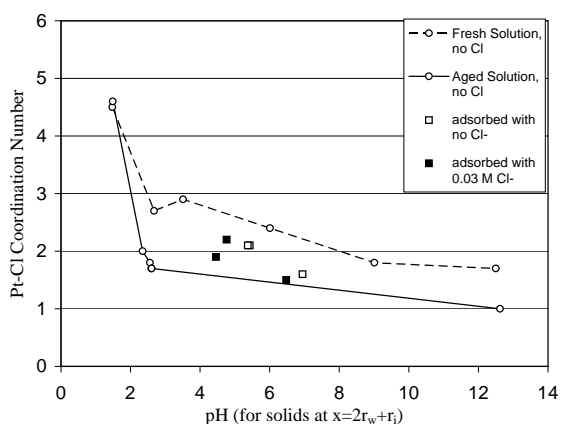


Figure 3. Comparison of the chlorine coordination numbers of adsorbed (series A) and fresh and aged liquid phase (200 ppm) CPA complexes, from [5].

complexes speciate accordingly. Since this series was prepared with an excess of liquid, the chloride could be far from the surface and much would be removed when the solid was filtered from the solution.

Reduction of CPA Adsorbed on Carbon. A chemical mechanism has been cited for CPA adsorption over carbon; XPS studies reveal the presence of Pt^{+2} in samples dried at 100 °C [6]. We have employed real-time, in-situ XANES to try to determine if Pt reduction accompanied adsorption, or occurred after it. A representative set of XANES spectra is shown in figure 4. CPA was adsorbed onto activated carbon at an initial pH below 3.0. The decrease in the white line intensity (from back to front) indicates an almost complete reduction of Pt^{+4} to Pt^{+2} over a time span of two hours. Chloride appears to be the predominant ligand at all times.

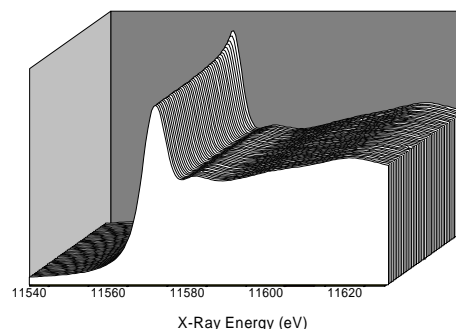


Figure 4. XANES spectra illustrating the reduction of Pt^{+4} to Pt^{+2} during contact with an activated carbon surface, over a 2 hour period (back to front).

The adsorption of CPA onto carbon was much more rapid than the time scale of this change, attaining about 95% of equilibrium adsorption in about 10 minutes. Since the time scales for adsorption and reduction are very different, we conclude that adsorption and reduction are independent phenomenon and can be modeled as such.

By following the white line intensity versus time the reduction rates of the different carbon samples can be compared [3]. Figure 5 is a summary plot of log (percent Pt (IV)) versus number of scans. The curves can be divided into two groups; activated carbons have a smaller slope compared to that of Vulcan, a carbon black and Asbury, which is graphitic. There are two possible explanations to account for the differences in rate. First, the higher surface area, smaller pore activated carbons exhibit resistance to mass transfer, or second, redox reactions with Pt are more favorable over graphitized surfaces than activated carbon surface considering the electron donor property of the surface π -complexes [3].

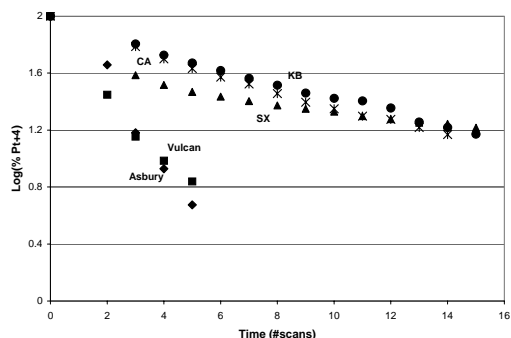


Figure 5. In-situ XANES analysis: reduction of Pt on various carbons. CA, KB, and SX are activated carbon, Vulcan is carbon black, and Asbury is graphitic. From [3].

Sintering Pathway of PTA Adsorbed onto Silica. Highly dispersed Pt on silica can be synthesized by conducting an impregnation at the optimal pH value for “strong electrostatic adsorption” (SEA) of PTA cations over a negatively charged silica surface [4]. The effect of metal loading and calcination on dispersion is shown in Figure 6 for 1 and 2% Pt on silica prepared by adsorption of PTA at a pH of 9.5 with NH_4OH . As the metal loading increases, the dispersion is lower at calcination temperatures up to about 500°C , above which the dispersion is not dependent on the metal loading.

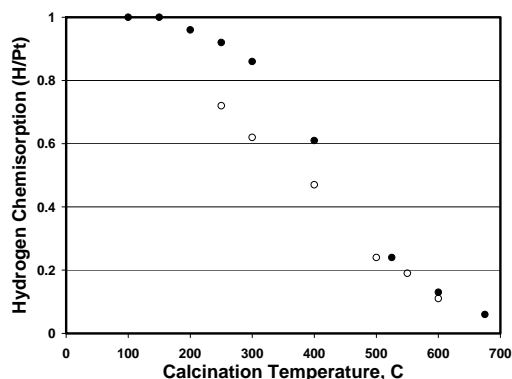


Figure 6. The effect of calcination temperature and metal loading on dispersion for 1% Pt (solid circles) and 2% Pt (open circles) on silica prepared by adsorption.

XANES and EXAFS spectra of samples calcined at 100, 300, and 600°C are shown in figure 7. As the calcination temperature increases, there is a continual increase in white line intensity confirming the oxidation of PTA by calcination. EXAFS analysis confirms a parallel increase in the Pt-O coordination number. Pt^{+4} oxide with 6 Pt-O bonds is formed at 300°C and remains the dominant species up to calcination temperature of 525°C . Calcination at temperatures higher than 525°C leads to formation of metallic Pt-Pt bonds at 2.77 \AA .

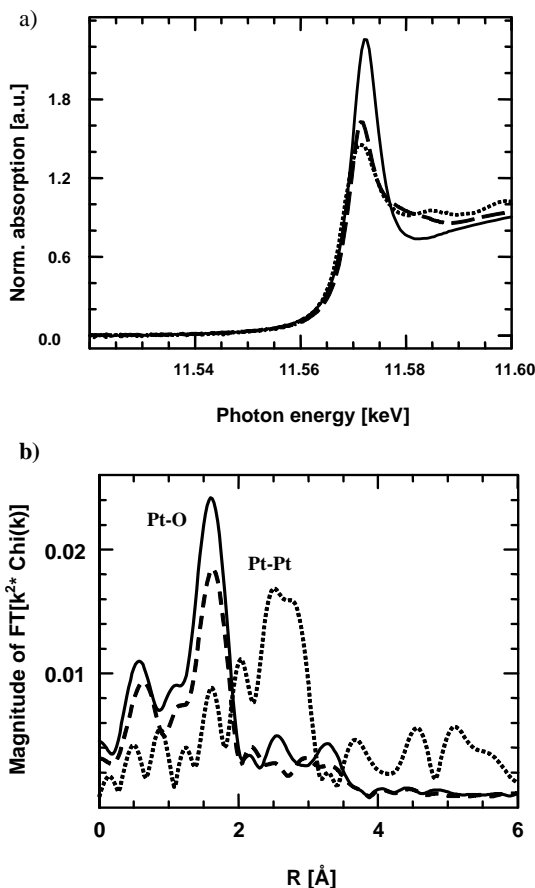


Figure 7. Analysis of 1% Pt on silica prepared by SEA with PTA at a pH = 9.5 and calcined at 100°C (dashed), 300°C (solid) and 600°C (dotted) a) normalized XANES spectra, b) EXAFS spectra.

The reduction of the intermediate Pt^{+4} phase leads to the formation of large metallic particles with a dispersion of about 0.4 [4]. Calcination above 525°C , leads to even larger metallic particles. By combination of the adsorption method of preparation and calcination temperature, very small to large metallic nanoparticles can be prepared.

Conclusions

Molecular characterization of a variety of Pt containing catalysts by EXAFS and XANES performed at the APS has yielded much fundamental insight on the synthesis of these materials.

Acknowledgements

JRR gratefully acknowledges the support of the National Science Foundation (NSF CTS-024341). Use of the Advanced Photon Source was supported by the U. S. Department of Energy, Office of Science, Office of Basic Energy Sciences, under Contract No. W-31-109-Eng-38. Work performed at MRCAT is supported, in part by funding from the Department of Energy under grant number DE-FG02-04ER46106.

The submitted manuscript has been created by the University of Chicago as Operator of Argonne National Laboratory under Contract No. W-31-109-Eng-38 with the U.S. Department of Energy. The U.S. Government retains for itself, and others acting

on its behalf, a paid-up, nonexclusive, irrevocable worldwide license in said article to reproduce, prepare derivative works, distribute copies to the public, and perform publicly and display publicly, by or on behalf of the Government.

References

1. Miller, J.T.; Neylon, M.K.; Marshall, C.L. and Kropf, A.J, in *Dekker Encyclopedia of Nanoscience and Nanotechnology*, Marcel Dekker, Inc., 3952, 2004.
2. Spieker, W. A., Liu, J., Hao, X., Miller, J. T., Kropf, A. J., and Regalbuto, J. R., *Appl. Catal. A: Gen.*, 232,2002, 219.
3. Hao, X., and Regalbuto, J.R., manuscript in preparation.
4. Miller, J. T., Kropf, A. J., Scheier, M., and Regalbuto, J.R., *J. Catal.* 225, 2004, 203.
5. Spieker, W. A., Liu, J., Hao, X., Miller, J. T., Kropf, A. J., and Regalbuto, J. R., *Appl. Catal. A: Gen.*, 243, 2003, 53.
6. Fraga, M. A., et al., *Journal of Catalysis* 209 (2002), 355.

IN SITU X-RAY ABSORPTION SPECTROSCOPY OF CATALYSTS

C. L. Marshall, M. K. Neylon, M. J. Castagnola, A. J. Kropf

Chemical Engineering Division
Argonne National Laboratory
Argonne, IL 60439-4837

Introduction

Much of the productivity improvements in the chemical industry within the last century could not have occurred without the help of catalysts. Catalytic materials provide improvements in reaction rate and product selectivity by lowering the activation energy by which chemical reactions occur. A wide variety of chemical substances show catalytic activity, but most industrial processes employ heterogeneous catalysts that are comprised of metal, metal oxide, or metal sulfide nano-sized particles on porous, high-surface area supports.

Of interest to most catalyst researchers is the structure of the active site, especially under reaction conditions. While a number of instrumental methods are used to characterize the active site in nanoparticles, many of these methods require idealized materials or conditions such as thin films, ultra-high vacuum, low temperature, etc. This is in contrast with typical catalyst operating conditions, normally requiring high reaction pressures and temperatures. Data obtained under ambient conditions may differ significantly from those obtained under realistic operating conditions. X-ray Absorption Spectroscopy (XAS), however, can be used to determine the average local electronic and structural environment of a catalytic metal site under realistic conditions, thus overcoming both the pressure and materials gap. As a result, the use of XAS as a key method for nanoparticle characterization of heterogeneous catalysts has grown considerably in the last decade. Several excellent reviews describe XAS in the context of catalyst characterization (1-11). The increase in the use of XAS in catalysis is in part also due to the increased availability of synchrotrons, improved data quality, and improvements in both hardware and software for data analysis.

While more catalysis researchers are using XAS characterization, there is still a push for the development of in situ data collection methods to observe the catalyst under reaction conditions. Since one must allow x-rays access to the sample and detect x-rays from inside the sample chamber, reactor design can be quite involved. Any material that intercepts the x-ray beam, including the sample in transmission XAS, must be somewhat transparent at the x-ray energy being used. There are a limited number of materials that are nearly transparent to x-rays, non-reactive, and with high mechanical strength. Transmission measurements are relatively simple, since there need be only a small window for x-ray entrance and exit. Catalyst samples are typically mounted as self-supporting wafers to reduce the detrimental absorption from a support.

Experimental

Work was done at the Advanced Photon Source (APS) at Argonne National Laboratory at the Materials Research Collaborative Access Team (MR-CAT) insertion device beam line. The procedures used and the data analysis have been summarized elsewhere (12).

Initial work in our laboratory utilized a single sample holder in a controlled atmosphere cell. The cell was capable of controlling a mixture of gasses at atmospheric pressure at temperatures up to 800 °C. Using this set up, we obtained our first

on line data on Cu-ZSM-5 reduction (12). Analysis of this data revealed much about the nature of the Cu in the oxidized and reduced states and the analysis of this data will form the basis of this talk.

To improve throughput at the beam line, a multi-sample holder was developed. This sample holder (Figure 1) has two advantages. First, it allowed four samples to be analyzed at once resulting in time savings of up to 70% over the single sample mode. More importantly, the four-sample holder ensures that the four catalysts being compared are treated exactly the same (temperature, pressure, gas composition).

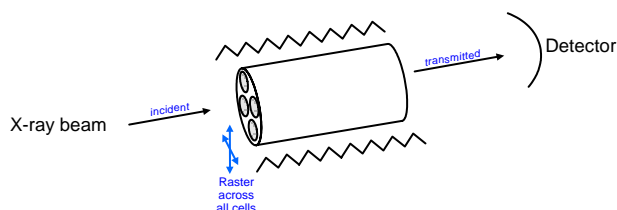


Figure 1. Multi sample holder for in situ XAS.

Results and Discussion

XANES Analysis. Figure 2 shows the composite plot of the TPR for Cu-ZSM-5 from room temperature up to 600 °C. At room temperature, the XANES spectrum is typical of only Cu²⁺. As the temperature is increased in H₂ flow, a pre-edge feature (~8980 eV) typical of Cu⁺ begins to grow in and the Cu²⁺ feature slowly disappears. At even higher temperatures, the Cu⁺ feature decreases and metallic Cu⁰ becomes the dominant species.

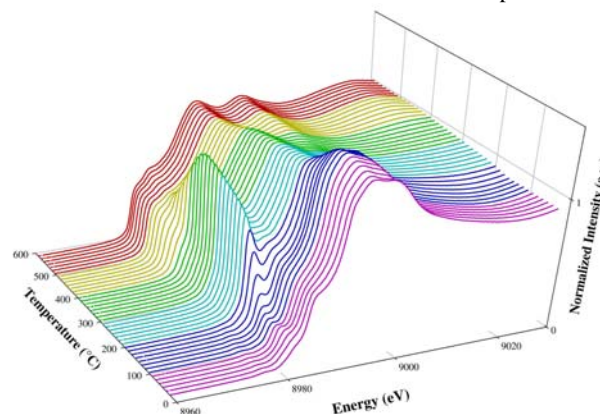


Figure 2. Normalized XANES spectra across the Cu K edge collected during the temperature programmed reduction of Cu-ZSM-5 in 5% H₂/He at a rate of 3°C/min. From [12].

The visualization of this type of data is informative with respect to gross analysis of when reduction of the metal occurs. In order to be quantitative, however, we have utilized the technique of principle component analysis (PCA) to understand the amount of each oxidation state for a given temperature. PCA was performed using methods similar to those from Malinowski (13). The normalized data were collected in a matrix, and singular value decomposition was used to find the associated eigenvalues and eigenvectors. Using empirical selection rules as discussed below, either 3 or 4 eigenvalues and eigenvectors were selected to be the basis set for the system. While, ideally, for XANES analysis, pure phases of the species in question should be selected, the pure Cu

states have significantly different XANES behavior than the zeolite counterparts, and would drastically affect the factor analysis results. Instead, iterative key set factor analysis (IKSFA) (13) was used to determine which of the initial XANES data sets were most fundamental, and the other data in the set were fitted using a least squares analysis on a linear sum of these fundamental vectors.

Factor analysis of the H_2 TPR data showed that no less than 3 components were present in the various XANES spectra. However, 3 components did not account for the entire variance in the data; using a 4th component resulted in a more complete accounting. Using empirical methods, it was determined that using five or more components was over-compensating for the experimental error. For comparison, both a 3-component and 4-component fit were investigated. For both cases, IKSFA resulted in a low-temperature ($<100^\circ\text{C}$) and high-temperature ($>500^\circ\text{C}$) component. The remaining one or two components, respectively, were found in the moderate temperature range of $200\text{--}300^\circ\text{C}$. We have assigned the lowest temperature component as predominantly Cu^{2+} and the highest temperature component as predominantly Cu^0 , given the similarity of these spectra to expected spectra for those oxidation states. The intermediate peaks we have assigned as either Cu_3A or Cu_4A and Cu_4B (not shown) for the intermediate states for either 3- or 4-component fits, respectively; these states appear to be related to Cu^{1+} , as the Cu^{1+} pre-edge feature is predominate in each, but may have some Cu^{2+} nature, as well.

Using the selected component states, the remaining XANES spectra were fitted to a linear combination of these states in order to determine the composition of each state, as shown in Figure 3 for the 3-component fits. Note that because no true reference materials were used, the composition of the basis components appears to be a single phase, but may actually be a composition of multiple true phases, as indicated by the analysis of the XANES structure. However, these compositions can still be used to observe the step-wise transformation of the spectra between the 3 or 4 states.

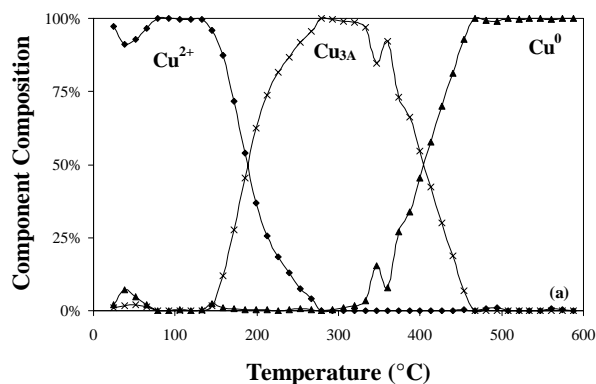


Figure 3. Phase composition of each XANES spectra during H_2 -TPR of Cu-ZSM-5 as determined from factor analysis. (a) Compositions determined using a 3-component fit. From [12].

EXAFS Analysis

While analysis of the XANES spectra provides information on the oxidation state of the metal at a given set of conditions, in order to learn about the coordination of the metal, analysis of the Extended X-ray Absorption Fine Structure (EXAFS) is required. The EXAFS regime is normally defined as at least 50 eV above the edge step.

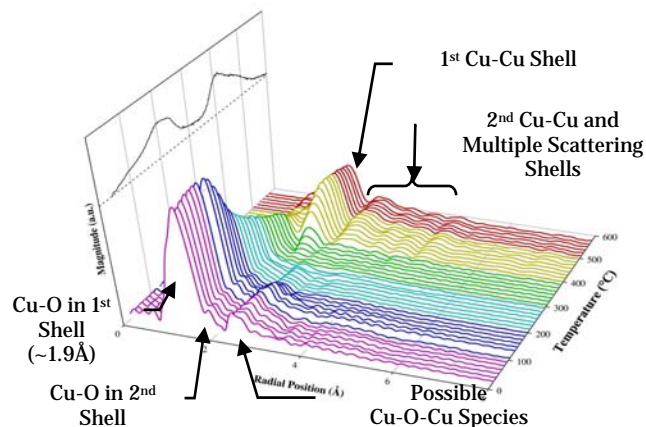


Figure 4. Fourier transform magnitude plot of the EXAFS spectra collected at the Cu K edge during the temperature programmed reduction of Cu-ZSM-5 in 5% H_2 /He at a rate of $3^\circ\text{C}/\text{min}$. Radial positions have not been corrected for phase shift. From [12].

The Fourier transform of the EXAFS data for the H_2 TPR of Cu-ZSM-5 is shown in Figure 4. The fitted parameters along with error estimates are presented in Table 1. The fits were able to account for all but 5% of the variance in the data, even in the worst cases. The goodness-of-fit parameter \mathcal{R} calculated from the sum of the squares of the difference between the experimental data and the fit, and normalized to the amplitude of the data, is also given in Table 1. Initially, there is a large contribution from Cu-O bonds at 1.95 \AA as well as from a longer Cu-O bond at 2.85 \AA . There are also a set of scattering paths in the $3.5\text{--}5.0 \text{ \AA}$ range; while additional paths from CuO and Cu_2O were used to try to fit these paths, no successful model could be discovered. Previous EXAFS studies in the literature suggest that the shells in this region are associated with scattering from Cu-O-Cu bridges that can easily exist in Cu-ZSM-5 and other exchanged zeolites (14-18). No Cu-Cu scattering path could be fitted in the $1.2\text{--}5.0 \text{ \AA}$ range at low temperatures, which suggests that the Cu exists mostly as isolated Cu species on the zeolite framework, as opposed to small CuO particles. For comparison, several Cu-ZSM-5 species that were drastically overexchanged were examined separately. The strong presence of a Cu-Cu shell and additional shells at $R > 3 \text{ \AA}$ in these materials indicate the presence of long-range order from CuO or Cu_2O cluster formation. In contrast, these cluster features are not present on the ca. 100% exchanged Cu-ZSM-5 sample used in this study, demonstrating the isolation of the Cu species. The initial coordination number of 4.8 for the first Cu-O shell is larger than the expected value of 4 for CuO, but other researchers have found coordination numbers up to 6 for Cu-O in ZSM-5 when charge-balanced by hydroxyl groups (14, 15, 19).

Conclusions

In situ analysis using high energy synchrotron energies can have a profound impact on the understanding of heterogeneous catalysis. We have provided an example in which the use of in situ XAS has elucidated much regarding the nature of the Cu in Cu-ZSM-5 catalysts; we identified the Cu^{1+} state as the active state. We have also determined that the onset of deactivation occurs concurrently with growth of metallic copper particles.

The rapid increase of XAS in the literature on the characterization of heterogeneous supported catalytic nanoparticles

is testament to the increasing availability of synchrotrons, improved data quality, and user-friendly software. The number and availability of new synchrotrons is expected to continue to increase within the next 10 years. In addition, data quality continues to improve and data acquisition time continues to decrease. Spectra that once took several hours to collect can be now obtained within a few minutes. These developments combine to make synchrotron methods a very attractive tool for catalyst characterization.

Acknowledgement. The submitted manuscript has been created by the University of Chicago as Operator of Argonne National Laboratory ("Argonne") under Contract No. W-31-109-Eng-38 with the U.S. Department of Energy. The U.S. Government retains for itself, and others acting on its behalf, a paid-up, nonexclusive, irrevocable worldwide license in said article to reproduce, prepare derivative works, distribute copies to the public, and perform publicly and display publicly, by or on behalf of the Government.

References

1. Fernández-García, M. XANES Analysis of Catalytic Systems under Reaction Conditions. *Catal. Rev.* 2002, 44(1), 59.
2. Iwasawa, Y. X-Ray Absorption Fine Structure for Catalysis and Surfaces, World Scientific: Singapore, 1996.
3. Vlaic, G.; Andreatta, D.; Colavita, P.E. Characterization of Heterogeneous Catalysts by EXAFS. *Catal. Today* 1998, 41(1-3), 261.
4. Conesa, J.C.; Esteban, P.; Dexpert, H.; Bazin, D. Characterization of Catalyst Structures by Extended X-Ray Absorption Spectroscopy. *Stud. Surf. Sci. Catal.* 1990, 57(Spectrosc. Charact. Heterog. Catal., Pt. A), A225.
5. Iwasawa, Y. Applications of X-Ray Absorption Fine Structure to Catalysts and Model Surfaces. *Journal de Physique IV* 1997, 7(C2, X-Ray Absorption Fine Structure, Vol. 1), 67.
6. See papers in Koningsberger, D.C.; Mojet, B.L. *Topics in Catal.* 2000, 10, 143.
7. Chao, K.j.; Wei, A.C. Characterization of Heterogeneous Catalysts by X-Ray Absorption Spectroscopy. *Journal of Electron Spectroscopy and Related Phenomena* 2001, 119(2-3), 175.
8. Meitzner, G. Experimental Aspects of X-Ray Absorption Spectroscopy. *Catal. Today* 1998, 39(4), 281.
9. Johnston, P.; Wells, P.B. EXAFS Spectroscopy of Supported Metal Catalysts. *Radiat. Phys. Chem.* 1995, 45(3), 393.
10. Izumi, Y. X-Ray Absorption Fine Structure Spectroscopy as a Probe of Chemical State of Catalysts. *Trends in Inorganic Chemistry* 1998, 5, 43.
11. Bertagnolli, H.; Ertel, T.S. X-Ray Absorption Spectroscopy of Amorphous Solids, Liquids, and Catalytic and Biochemical Systems: Capabilities and Limitations. *Angew. Chem.* 1994, 106(1), 15.
12. "In Situ EXAFS Analysis of the Temperature Programmed Reduction of Cu-ZSM-5," M. K. Neylon, C. L. Marshall, and A. J. Kropf, *J. Amer. Chem. Soc.*, 124(19), 5457-5465 (2002).
13. Malinowski, E.R. *Factor Analysis in Chemistry*, 2nd Edition; John Wiley and Sons: New York, 1991.
14. Turnes Palomino, G.; Fiscaro, P.; Bordiga, S.; Zecchina, A.; Giamello, E.; Lamberti, C. *J. Phys. Chem. B* 2000, 104, 4064-4073.
15. Grünert, W.; Hayes, N.W.; Joyner, R.W.; Shpiro, E.S.; Rafiq, M.; Siddiqui, H.; Baeva, G.H. *J. Phys. Chem.* 1994, 98, 10832-10846.
16. Kuroda, Y.; Yoshikawa, Y.; Konno, S.I.; Hamano, H.; Maeda, H.; Kumashiro, R.; Nagao, M. *J. Phys. Chem.* 1995, 99, 10621-10628.
17. Kuroda, Y.; Maeda, H.; Yoshikawa, Y.; Kumashiro, R.; Nagao, M. *J. Phys. Chem. B* 1997, 101, 1312-1316.
18. Huang, Y.J.; Wang, H.P. *J. Phys. Chem. A* 1999 103, 6514-6516.
19. Yamashita, H.; Matsuoka, M.; Tsuji, K.; Shioya, Y.; Anpo, M.; Che, M. *J. Phys. Chem.* 1996, 100, 397-402.

Table 1. EXAFS fitting parameters for selected temperatures during H₂ TPR reduction of Cu-ZSM-5. (^a × 10⁻² Å²)

Temp.	Cu-O First Shell			Cu-O Second Shell			Cu-Cu			R ²
	N	R (Å)	σ ² ^a	N	R (Å)	σ ² ^a	N	R (Å)	σ ² ^a	
25°C	4.8 ± 0.5	1.95 ± 0.01	0.51	3.0 ± 0.5	2.85 ± 0.01	0.75	n.f.	n.f.	n.f.	0.8
100°C	5.4 ± 0.6	1.96 ± 0.01	0.60	2.7 ± 0.5	2.91 ± 0.02	0.89	n.f.	n.f.	n.f.	0.6
200°C	3.9 ± 0.4	1.94 ± 0.01	0.72	1.9 ± 0.7	2.85 ± 0.04	1.07	n.f.	n.f.	n.f.	1.9
300°C	2.8 ± 0.3	1.96 ± 0.01	0.84	0.3 ± 0.5	2.85 ± 0.08	1.27	n.f.	n.f.	n.f.	3.9
400°C	1.6 ± 0.2	1.97 ± 0.01	0.98	n.f.	n.f.	n.f.	4.0 ± 0.3	2.51 ± 0.01	1.67	4.1
500°C	0.3 ± 0.2	1.97 ± 0.02	1.12	n.f.	n.f.	n.f.	8.2 ± 0.3	2.51 ± 0.01	1.94	0.9
600°C	0.3 ± 0.2	1.97 ± 0.02	1.23	n.f.	n.f.	n.f.	8.3 ± 0.4	2.50 ± 0.01	2.22	1.4

SURFACE STRUCTURES OF VANADIUM OXIDE SUPPORTED ON ALUMINAS CHARACTERIZED BY ULTRAVIOLET AND VISIBLE RAMAN SPECTROSCOPY

Zili Wu¹, Hack-Sung Kim¹, Sreekala Rugmini², S. David Jackson² and Peter C. Stair*¹

¹Center for Catalysis and Surface Science, Northwestern University, Evanston, IL 60208, USA. pstair@northwestern.edu

²Department of Chemistry, Joseph Black Building, The University, Glasgow G12 8QQ, Scotland, UK

Introduction

Supported vanadia catalysts have attracted significant interest in recent decades due to their good catalytic performance in many redox reactions,¹ such as dehydrogenation and oxidative dehydrogenation of alkanes to olefins, oxidation of methanol to formaldehyde, ammoxidation of aromatic hydrocarbons, and selective reduction of NO_x. A better understanding of the catalytic properties of supported vanadium oxides requires determination of the structure-reactivity relationships of the supported VO_x catalysts. Raman spectroscopy has been successfully and frequently employed by many research groups for characterization of the molecular structure of supported vanadium oxides.^{1–8} Most conventional Raman studies of supported VO_x catalysts were carried out using a single excitation wavelength in the visible region (either 514 or 532 nm).^{1–6} However, several recent studies^{7, 8} suggest that more complete and sometimes new structural information of supported metal oxides can be achieved by using multiple excitation wavelengths. The reason lies in the strong electronic absorptions in the UV and visible wavelength regions exhibited by most transition metal oxides that make it possible to measure resonance-enhanced Raman spectra. Under circumstances where supported VO_x species are present in a distribution of cluster sizes or coordination geometries, it is likely that these species also possess a corresponding distribution of electronic absorption wavelengths. Excitation of Raman spectra within the absorption region will produce resonance-enhanced spectra from the subset of VO_x species with absorptions at the excitation wavelength. By measuring the Raman spectra at several wavelengths, more information can be obtained about the various VO_x species in the distribution. Moreover, when UV excitation is employed, even Raman spectra from supported VO_x at low loadings (<1% wt) on oxides having strong fluorescence are possible because of the avoidance of fluorescence and enhanced sensitivity.⁹

The present work aims at a further study of the structure of VO_x supported on alumina (δ -, α -, and γ -Al₂O₃) using both UV- (244 nm) and visible- (488 nm) excited Raman. Interpretation of the Raman spectra was also aided by UV-Visible diffuse reflectance spectroscopy (UV-Vis DRS) and temperature-programmed reduction (TPR) measurements.

Experimental

All supported VO_x samples were prepared via incipient wetness impregnation of aluminas (δ -Al₂O₃: Johnson Matthey, UK, S_{BET} = 101 m²/g, γ -Al₂O₃: Engelhard, S_{BET} = 220 m²/g, and α -Al₂O₃: Aldrich, S_{BET} = 11 m²/g) with aqueous NH₄VO₃ solutions. Surface VO_x density varied in the range 0.01 – 14.2 V/nm².

Raman Studies. The samples were studied by both UV (244 nm) and visible (488 nm) Raman spectroscopy under hydrated and dehydrated conditions. Both UV and visible Raman spectra were collected using the fluidized bed reactor and UV Raman instrument built at Northwestern University^{8–10}.

UV-Vis DRS. DRS spectra in the range of 200–800 nm were taken from the samples in a transparent vial on a Varian Cary 1E UV-Vis spectrophotometer equipped with a diffuse-reflectance attachment, using MgO as a reference.

H₂-TPR. H₂-TPR was carried out in a H₂/Ar (5%) flow of 40 ml/min from room temperature to 1023 K with a ramp of 8 K/min after the sample was calcined at 773 K for 2h.

Results and Discussion

The visible Raman spectra of dehydrated δ -Al₂O₃ are shown in Fig. 1. The spectra of V/ δ -Al₂O₃ with surface VO_x density lower than 0.16 V/nm² are dominated by fluorescence from the δ -Al₂O₃ support. Samples with surface VO_x densities above 0.16 V/nm² start to show Raman bands due to VO_x species: a weak broad band centered at 915 cm⁻¹, a V=O vibration at 1023 cm⁻¹ for 0.16V, 1030 cm⁻¹ for 1.2V, and 1035 cm⁻¹ for 4.4V and 8.8V samples, and an intense band at 994 cm⁻¹ characteristic of V₂O₅ for 4.4V and above. The broad band at ~915 cm⁻¹ has previously been ascribed to V–O–V stretching modes and used as a proof for the presence of polymerized VO_x species.^{1–5} Here we assign it to the interface mode, V–O–Al, in accord with recent DFT calculations of the VO_x-Al₂O₃ system.¹¹ This assignment is confirmed by the UV Raman results described below. For hydrated samples (spectra not shown), a broad Raman feature centered at 900 cm⁻¹ covers the whole spectral range (800 – 1050 cm⁻¹) at surface VO_x densities of 0.16 and 1.2 V/nm². The broad band can be due to hydrated, polymerized VO_x species³ and becomes a shoulder on the lower wavenumber side of the V₂O₅ band at 994 cm⁻¹ at higher VO_x density.

UV Raman spectra of dehydrated V/ δ -Al₂O₃ are shown in Fig. 2. It is striking to note that some Raman features due to surface VO_x species can be distinguished for V/ δ -Al₂O₃ samples at extremely low surface density even down to 0.01 V/nm², i.e., a weak Raman band at 1013 cm⁻¹ and a broad shoulder at around 912 cm⁻¹ (Fig. 2A-b). These Raman features cannot be detected in the visible Raman spectra (see Fig. 1). The broad feature centered at 912 cm⁻¹ is present with medium intensity at all loadings, suggesting that this broad Raman feature cannot be exclusively assigned to V–O–V stretching and supported the theoretical assignment to V–O–Al bonds. The 1013-cm⁻¹ band, assigned to the V=O stretching mode of surface VO_x species, shifts gradually to higher wavenumber as the surface VO_x density increases. This band remains observable at ca. 1026 cm⁻¹ for a surface VO_x density of 14.2 V/nm², a result which is clearly different from the visible Raman spectra (Fig. 1) where the V=O band is above 1030 cm⁻¹ for surface VO_x densities greater than 1.2

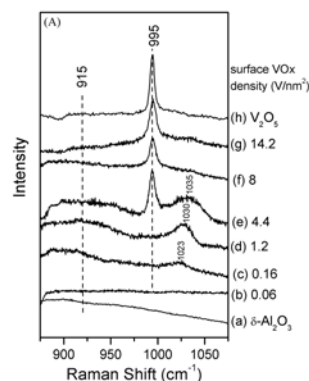


Figure 1. Visible ($\lambda_{\text{excitation}} = 488$ nm) Raman spectra of dehydrated V/ δ -Al₂O₃ as a function of surface VO_x density (V/nm²).

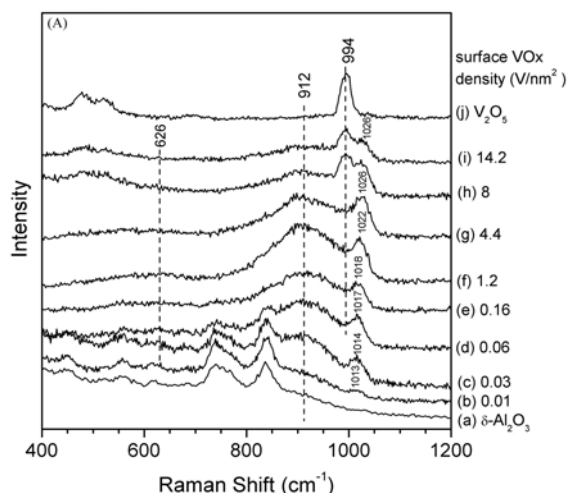


Figure 2. UV ($\lambda_{\text{excitation}} = 244 \text{ nm}$) Raman spectra of dehydrated $\text{V}/\delta\text{-Al}_2\text{O}_3$ as a function of surface VO_x density (V/nm^2).

V/nm^2 and disappears above monolayer loading ($8 \text{ V}/\text{nm}^2$). The differences in Raman shift and in intensity vs. VO_x density between visible- and UV-excited Raman spectra suggest the presence of different types of surface VO_x species on the Al_2O_3 support. At medium surface VO_x densities ($0.16 - 4.4 \text{ V}/\text{nm}^2$), a weak broad feature appears near 625 cm^{-1} , indicating the formation of polymerized VO_x species on the surface. When the surface VO_x density is above $8 \text{ V}/\text{nm}^2$, the formation of crystalline V_2O_5 is evident from the characteristic band at 994 cm^{-1} and additional bands in the range $400 - 600 \text{ cm}^{-1}$.

UV Raman spectra of hydrated $\text{V}/\delta\text{-Al}_2\text{O}_3$ are in a manner similar to the visible spectra. Broad Raman features due to surface, hydrated polyvanadate species dominate the spectra (not shown).

Results from both UV and visible Raman studies give us an evolving picture of surface VO_x species on $\delta\text{-Al}_2\text{O}_3$: $\text{V}/\text{Al}_2\text{O}_3$ with a surface density lower than $1.2 \text{ V}/\text{nm}^2$ possesses mainly isolated VO_x in tetrahedral coordination. At surface densities higher than $1.2 \text{ V}/\text{nm}^2$, a mixture of polyvanadates with different polymerization degrees participates to a larger extent on the surface, and V_2O_5 forms at a surface VO_x density above $4.4 \text{ V}/\text{nm}^2$. This picture is further confirmed by our UV-Vis DRS and TPR measurements (not shown here) of $\text{V}/\delta\text{-Al}_2\text{O}_3$ samples.

Comparing the UV and visible Raman spectra of $\text{V}/\delta\text{-Al}_2\text{O}_3$ samples, two kinds of $\text{V}=\text{O}$ band shift can be distinguished: a shift as a function of excitation wavelength for the same sample and a shift as a function of surface VO_x density for different samples. The former shift is caused by different VO_x structures selectively detected at different excitations as evidenced by UV-Vis DRS spectra. It appears that visible excited Raman spectra are more sensitive to polymeric or cluster VO_x and UV excited Raman spectra are more sensitive to isolated and less polymerized VO_x species. The latter shift, from 1012 to 1027 cm^{-1} as the surface VO_x density increases from 0.01 to $14.2 \text{ V}/\text{nm}^2$ in the case of UV-excited Raman spectra (Fig. 2), can be ascribed to the continuous evolution of VO_x structures on the surface.

The Raman, UV-Vis DRS and H_2 -TPR results show that the structure, distribution, and reducibility of surface VO_x species on $\gamma\text{-Al}_2\text{O}_3$ are quite similar to those on $\delta\text{-Al}_2\text{O}_3$. This similarity is understandable since both $\delta\text{-}$ and $\gamma\text{-Al}_2\text{O}_3$ have a spinel structure

with similar types (but different distribution) of surface hydroxyl groups which are the bonding sites for VO_x species on the aluminas. However, Raman (both UV and Visible) and TPR results for VO_x on $\alpha\text{-Al}_2\text{O}_3$ are quite different from those of VO_x on $\delta\text{-}$ and $\gamma\text{-Al}_2\text{O}_3$, suggesting different surface VO_x species on $\alpha\text{-Al}_2\text{O}_3$. The different bulk structure (corundum) and surface properties (few hydroxyl groups) of $\alpha\text{-Al}_2\text{O}_3$ may account for the difference. Insights into the nature of the VO_x species on $\alpha\text{-Al}_2\text{O}_3$ require further investigations.

Acknowledgement. This work is financially supported by ATHENA and the Chemical Sciences, Geosciences and Biosciences Division, Office of Basic Energy Sciences, Office of Science, U.S. Department of Energy under Grant No. DE-FG02-97ER14789. The Athena project is funded by the Engineering & Physical Sciences Research Council (EPSRC) of the U.K. and Johnson Matthey plc

References

- (1) Weckhuysen, B. M.; Keller, D. E. *Catal. Today* **2003**, 78, 25.
- (2) Wachs, I. E. *Catal. Today* **1996**, 27, 437.
- (3) Deo, G.; Wachs, I. E. *J. Phys. Chem.* **1991**, 95, 5889
- (4) Olthof, B.; Khodakov, A.; Bell, A. T.; Iglesia, E. *J. Phys. Chem. B* **2000**, 104, 1516.
- (5) Cortez, G. G.; Bañares, M. A. *J. Catal.* **2002**, 209, 197.
- (6) Bañares, M. A.; Wachs, I. E. *J. Raman Spectrosc.* **2002**, 33, 359.
- (7) Xiong, G.; Li, C.; Li, H. Y.; Xin, Q.; Feng, Z. C. *Chem. Commun.* **2000**, 677.
- (8) Chua, Y. T.; Stair, P. C.; Wachs, I. E. *J. Phys. Chem. B* **2001**, 105, 8600.
- (9) Li, C.; Stair, P. C. *Stud. Surf. Sci. Catal.* **1996**, 101, 881.
- (10) Chua, Y. T.; Stair, P. C. *J. Catal.* **2000**, 196, 66.
- (11) Magg, N.; Immaraporn, B.; Giorgi, J. B.; Schroeder, T.; Bäumer, M.; Döbler, J.; Wu, Z. L.; Kondratenko, E.; Cherian, M.; Baerns, M.; Stair, P. C.; Sauer, J.; Freund, H. J. *J. Catal.* **2004**, 226, 88.

TRANSFORMATIONS OF NITROGEN AND SULFUR FORMS IN PEAT DURING MILD THERMOLYSIS

S. R. Kelemen¹, M. L. Gorbaty¹, M. Afeworki^{1,2}, M. Sansone¹,
C. C. Walters¹ and A. D. Cohen²

¹ ExxonMobil Research and Engineering Co., Annandale, NJ 08801

² Department of Geological Sciences, University of South Carolina,
Columbia, South Carolina 29208

Abstract

A combination of XPS and ¹⁵N NMR were used to characterize the nitrogen forms in peats and mildly pyrolyzed peats (equivalent R_o ≤ 1.0). For unaltered peat, the ¹⁵N NMR spectrum and XPS nitrogen (1s) spectrum are consistent with the presence of amide nitrogen. Upon pyrolysis, the main peak in the ¹⁵N NMR spectrum broadens and shifts from -260 to -245 ppm. This change is consistent with the loss of some amide nitrogen and the appearance of pyrrolic nitrogen forms. Upon pyrolysis a new XPS peak appears at 398.6 eV characteristic of pyridinic nitrogen. Together these results indicate that a thermal transformation of amide nitrogen into pyrrolic and pyridinic forms occurs after thermal stress roughly equivalent to the bituminous stage of coalification. Sulfur XANES from unaltered peat indicates the presence of disulfide, mercapto, aliphatic, and aromatic organic sulfur. Sulfite and sulfate were present in most samples. Mild thermolysis results in elimination of disulfides, aliphatic sulfur and sulfite.

Introduction

Peat is a sedimentary deposit composed primarily of plant derived material and is a precursor to coal. Most organic nitrogen is derived from living organisms and decomposition processes hamper analytical attempts to trace nitrogen in lignites and coals back to their biological origins [1-5]. The processes that govern the initial diagenetic transformations of nitrogen forms are not well understood. Recent advances in ¹⁵N NMR [1-4, 6-9] and X-ray Photoelectron Spectroscopy (XPS) [10-13] have provided new tools to probe the chemical structure of nitrogen forms in complex solid and non-volatile carbonaceous systems. Much of the nitrogen in deposited biomass is lost quickly to biodegradation. Amide groups in proteins and peptides represent an abundant initial source of nitrogen but are thought to be susceptible to rapid deamination [1-5]. Numerous studies have shown that amide forms of nitrogen are present in recently deposited organic matter and peat [1-4, 6,7]. In general, these studies have demonstrated that some chemical environments containing amide groups, once created, are resistant to microbial degradation and survive through early diagenesis. For coals, the distribution of nitrogen forms depends on rank. In low rank coal, pyrrolic nitrogen is the most abundant nitrogen form followed by pyridinic and quaternary nitrogen [11,12]. The sulfur forms in peats are largely unstudied. For coal it is well established that aliphatic and aromatic sulfur forms are present and that the relative amount of aromatic sulfur increases with increasing coal rank [14, 15]. The possible connections between the nitrogen and sulfur forms present in peats and those in coal are explored in the present study by characterizing and comparing unaltered peats with peats that have been thermally stressed to roughly the bituminous stage of coalification.

Experimental

The peat samples were obtained from the peat sample bank of the University of South Carolina [16]. Nitrogen and sulfur elemental data for the peat and pyrolyzed peat samples are shown in Table 1. These peats differ significantly in composition due to the variety of

source plants and depositional settings. The peat samples were homogenized and ground into fine powders using a Wig-L-Bug® prior to analysis. Pyrolysis was done in an inert atmosphere for 5 minutes and 75 minutes at 400 °C. These conditions correspond to R_o=0.7 and 1.0, respectively, using the EasyR_o method [17].

XPS results were obtained with a Kratos Axis Ultra system using monochromatic Al K alpha radiation. A general description of XPS curve resolution methods for nitrogen appear elsewhere [11-13]. Solid-state ¹⁵N CPMAS NMR spectra were recorded using a Chemagnetics CMXII-200 spectrometer operating at a static magnetic field of 4.7 T (20.2 MHz ¹⁵N). The spectra are reported relative to nitromethane. The sulfur XANES spectra were obtained at beam line 6-2 of the Stanford Synchrotron Radiation Laboratory (SSRL) using methods developed previously for speciation and quantification of organically bound sulfur forms in coals [14].

Table 1. XPS Results for Nitrogen, Sulfur and Aromatic Carbon

	Per 100 Carbon			
	¹³ C NMR Aromatic Carbon	XPS Aromatic Carbon	XPS Nitrogen	XPS Sulfur
Lox. Nym. (Unaltered)	24	23	4.9	0.5
Lox. Nym (Ro=0.7)	67	53	5.0	0.5
Lox. Nym. (Ro=1.0)	n.d.	73	5.6	0.6
Oke. Tax. (Unaltered)	29	25	2.5	0.1
Oke. Tax. (Ro=0.7)	64	59	2.7	0.1
Oke. Tax (Ro=1.0)	n.d.	69	3.3	0.1
Coot Bay (Unaltered)	28	33	2.6	1.8
Coot Bay (Ro=0.7)	48	49	3.1	1.7
Coot Bay (Ro=1.0)	n.d.	80	3.5	2.3
N.C. 1st Col. (Unaltered)	36	29	1.8	0.1
N.C. 1st Col. (Ro=0.7)	70	60	1.4	<0.1
N. C. 1st Col. (Ro=1.0)	n.d.	75	1.8	<0.1

Results and Discussion

Table 1 shows that the XPS and ¹³C NMR results for aromatic carbon are in good general agreement for unaltered and pyrolyzed peats. There is a progressive increase in the level of aromatic carbon with increasing thermal stress. The relative amounts of nitrogen and sulfur remain constant upon thermolysis.

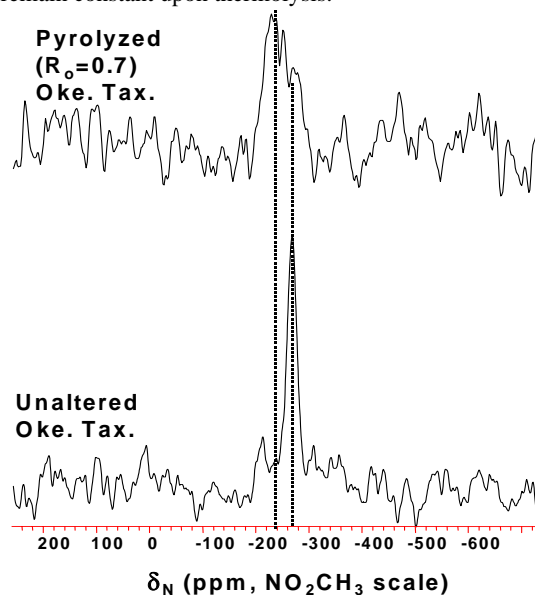


Figure 1. ¹⁵N NMR spectrum of unaltered and pyrolyzed Oke. Tax. peat

Figure 1 shows the ^{15}N CPMAS NMR spectrum for unaltered and pyrolyzed Oke. Tax. peat. A peak occurs in the ^{15}N NMR spectrum at -260 ppm and this position is consistent with the presence of amide nitrogen. Upon pyrolysis, the main peak in the ^{15}N NMR spectrum broadens and shifts to -245 ppm. This change is consistent with the loss of some amide nitrogen and the appearance of pyrrolic nitrogen forms. The same qualitative appearance of the ^{15}N NMR signal shown in Figure 1 is observed for unaltered and pyrolyzed Lox. Nym peat. The results of curve resolution of the XPS nitrogen (1s) spectrum are shown in Table 2. The spectra for all unaltered peats are dominated by a peak at 400.2 eV, consistent with the presence of amide and pyrrolic nitrogen. After pyrolysis, a new peak appears at 398.6 eV, characteristic of pyridinic nitrogen, and its relative intensity increases with thermal stress. These results indicate that thermal stressing of peat to a stage of coalification roughly equivalent to a bituminous coal can transform some of the amide nitrogen into pyrrolic and pyridinic forms.

Table 2 - XPS Nitrogen (1s) Curve Resolution Results

	Mole Percent		
	(398.6 eV) Pyridinic	(400.2 eV) Amide/ Pyrrolic	(401.4 eV) Quaternary
Lox. Nym. (Unaltered)	2	87	9
Lox. Nym (Ro=0.7)	36	61	3
Lox. Nym. (Ro=1.0)	43	53	2
Oke. Tax. (Unaltered)	4	80	14
Oke. Tax. (Ro=0.7)	37	58	5
Oke. Tax (Ro=1.0)	40	56	4
Coot Bay (Unaltered)	3	88	8
Coot Bay (Ro=0.7)	40	54	5
Coot Bay (Ro=1.0)	49	44	5
N.C. 1st Col. (Unaltered)	6	86	7
N.C. 1st Col. (Ro=0.7)	38	57	5
N. C. 1st Col. (Ro=1.0)	41	54	5

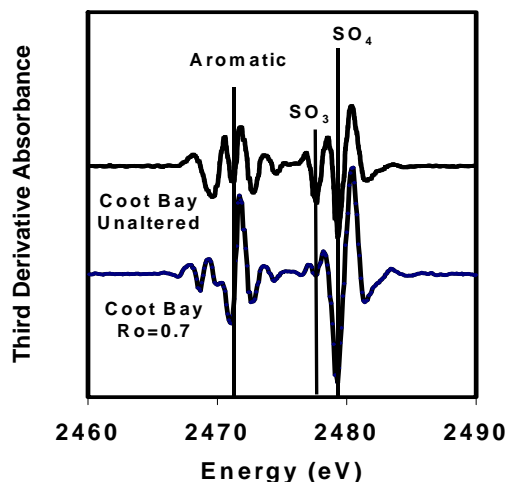


Figure2. Sulfur XANES 3rd Derivative Spectrum

Figure 2 shows the third derivative sulfur XANES spectra for unaltered and pyrolyzed Coot Bay peat. Indicated are the positions expected for sulfate, sulfite, and aromatic sulfur. It is clear that the SO_3 peak decreases upon pyrolysis and that there are significant changes in the appearance of the spectra below 2470 eV, a region where non-aromatic and non-oxidized sulfur forms appear. Table 4 shows the sulfur XANES analyses from unaltered and pyrolyzed

peat. Disulfide, mercapto, aliphatic, aromatic, sulfite and sulfate sulfur forms must be included to obtain a good fit to the spectrum from the unaltered peat samples (Table 3). Mercapto, disulfide, and sulfite are likely related to preserved biomass resistant to degradation. In contrast, only mercapto, aromatic and sulfate sulfur forms are needed to fit the spectrum of pyrolyzed peat. Disulfide and sulfite forms are thermally unstable and aromatic sulfur is the dominant sulfur form in peats thermally stressed to a state roughly equivalent to the bituminous stage of coalification.

Table 3 - S-XANES 3rd Derivative Curve Fitting

	Mole Percent					
	Cysteine mercapto	Cystine disulfide	Al	Ar	SO_3^{2-}	SO_4^{2-}
Lox. Nym. Unaltered	12	21	7	6	37	17
Lox. Nym (Ro=0.7)	10	0	0	23	0	67
Oke. Tax. Unaltered	16	24	0	10	47	3
Oke. Tax. (Ro=0.7)	39	0	0	59	0	2
Coot Bay Unaltered	8	19	15	7	29	22
Coot Bay (Ro=0.7)	16	0	0	27	0	57
N.C. 1st Unaltered	24	24	0	13	33	6
N.C. 1st (Ro=0.7)	40	0	0	60	0	0

Conclusions

^{15}N NMR and XPS results together indicate that thermal stress roughly equivalent to the bituminous stage of coalification can transform amide nitrogen in peat into pyrrolic and pyridinic forms. Sulfur XANES results show that mild thermolysis causes the elimination of disulfides, aliphatic sulfur and sulfite. Aromatic sulfur is the dominant sulfur form after mild thermolysis.

Acknowledgements. We wish to thank B. Liang for obtaining the ^{15}N NMR data, and P. J. Kwiatek for obtaining the XPS data.

References

- (1) Knicker, H.; Hatcher, P. G.; Scaroni, A. W., *Energy Fuels* **1995**, 9, 999.
- (2) Knicker, H.; Ludemann, H. D., *Org. Geochem.* **1995**, 23, 329.
- (3) Knicker, H.; Hatcher, P. G.; Scaroni, A. W., *Int. J. Coal Geology.*, **1996**, 32, 255.
- (4) Knicker, H.; Scaroni, A. W.; Hatcher, P. G., *Org. Geochem.* **1996**, 24, 661.
- (5) Baxby, M.; Patience, R. L.; Bartle, K. D., *J. Pet. Geol.* **1994**, 17, 211.
- (6) Knicker, H.; Ludemann, H. D., *Naturwissenschaften*, **1993**, 80, 219.
- (7) Knicker, H.; Almendros, G.; Gonzalez-Vila, F. J.; Ludemann, H. D.; Martin, F., *Organic Geochem.* **1995**, 23, 1023.
- (8) Solum, M. S.; Pugmire, R. J.; Grant, D. M.; Kelemen, S. R.; Gorbaty, M. L.; Wind, R. A *Energy Fuels* **1997**, 11, 493.
- (9) Kelemen, S. R.; Afeworki, M.; Gorbaty, M. L.; Kwiatek, P. J.; Solum, M. S.; Hu, J. Z.; Pugmire, R. J., *Energy Fuels*, **2002**, 16, 1507.
- (10) Wilhelms, A.; Patience, R. L.; Larter, S. R.; Jorgensen, S., *Geochimica Acta* **1992**, 56, 3745.
- (11) Kelemen, S. R.; Gorbaty M. L.; Kwiatek, P. J. *Energy. Fuels*, **1994**, 4, 897.
- (12) Pels, J. R.; Kapteijn, F.; Moulijn, J. A.; Zhu, Q.; Thomas, K., *Carbon* **1995**, 33 1641.
- (13) Kelemen, S. R.; Gorbaty, M. L.; Kwiatek, P.; Fletcher, T. H.; Watt, M.; Solum, M. S.; Pugmire, R. J., *Energy Fuels*, **1998**, 12, 159.
- (14) George, G. N.; Gorbaty, M. L.; Kelemen, S. R.; Sansone, M., *Energy Fuels*, **1991**, 5, 93.
- (15) Huffman, G. P.; Mitra, S.; Huggins, F. E.; Shah, N.; Vaidya, F.; Lu, F., *Energy and Fuels*, **1991**, 5, 574.
- (16) Cohen, A. D.; Rollins, M. S.; Durig, J. R.; Raymond, R., *J. Coal Quality*, **1991**, 10, 145.
- (17) Sweeney, J. J.; Burnham, A. K., *Bull. Am. Ass. Pet. Geologists*, **1990**, 74, 1559.

KINETICS OF NANOCOMPOSITES IN TWO-DIMENSION BY SAXS AND GISAXS

Jin Wang

Experimental Facilities Division, Argonne National Laboratory,
Argonne, IL 60439

Introduction

Metal nanoparticles dispersed in polymeric matrices or in liquid suspension can self-assemble to form complex nanocomposites or superlattices, which are of great interest in the fabrication of novel electronic, magnetic, photonic and fuel cell devices. Since the entire ordering process takes place far from equilibrium conditions, a controlled self-assembly of nanostructures in two dimensions has to be guided by a thorough understanding of ordering kinetics and nanoparticle dynamics in the composites. This requires measurement of their lateral diffusion and transport in situ and in real time with subnanometer spatial resolution, which has been difficult because of the paucity of the particles (often consisting of a sub-monolayer) and of the random particle distribution before they become ordered. The nanoparticle distribution has almost been exclusively studied by transmission electron microscopy (TEM), which often suffers from lack of time resolution and statistical information during a dynamic event. To overcome these difficulties, we have developed and used a novel method combining x-ray wave-guiding-based resonance-enhanced x-ray scattering (REXS) and grazing-incidence small-angle x-ray scattering (GISAXS) to elucidate the real-time lateral distribution and diffusion of a gold nanoparticle monolayer embedded in an ultrathin film polymer matrix.¹ The dynamics of superlattice formation during the evaporation of nanocrystal colloidal droplets was studied by in situ small-angle x-ray scattering experiment with unprecedented spatial and temporal resolutions. We showed that the evaporation kinetics has an important effect on the dimensionality of the superlattices.²

Experimental Methods

In thin films, REXS can be achieved either in a low electron density layer (LEDL, e.g., polymer) deposited onto an x-ray mirror with high electron density (Type I) or in a LEDL sandwiched between a thin cap layer with high electron density and an x-ray mirror (Type II). When the period of the x-ray standing waves, formed in the LEDL due to total external reflection upon the mirror, coincides with a submultiple of the thickness of the LEDL, a significant enhancement between 10 and 100 times of the electric field intensity can be observed and be used to increase the x-ray scattering intensity proportionally, so that weakly scattering structures can be probed in a time-resolved manner. The system of investigation is a submonolayer of Au nanoparticles synthesized by thermal evaporation and sandwiched between two layers of poly (tert-butyl acrylate) (PtBA) of equal thickness of ca. 350 Å, all deposited on a Ag mirror. The morphology of as-deposited Au nanoparticles in the polymer matrix is revealed by TEM, where the diameter of the nanoparticles ranges from 2 to 4 nm and the average distance between the particles is ca. 6 nm. The sample itself constitute a Type I x-ray waveguide where the morphology of the nanoparticle can be readily interrogated.

For studying the self-assembly kinetics of gold nanoparticles in suspension, Monodispersed gold nanocrystals were synthesized according to the digestive ripening procedure. We used gold nanocrystals with an average diameter of 7.5 nm and 5.8 nm in two different experimental runs and with the particle number concentration adjusted to be approximately 10^{13} mL⁻¹, just enough to form a monolayer. The volume concentration of thiol was 0.63%.

Both the GISAXS and SAXS experiments were conducted at the 1BM beamline of the Advanced Photon Source (APS).

Results and Discussion

The GISAXS data at the resonance condition, with experimental setup schematically shown in Fig. 1A, was collected as 2D images by an image plate detector. The sample cell, under internal He flow, was equipped with a resistive heater with temperature feedback accurate to within $\pm 0.5^\circ\text{C}$. Fig. 1B shows a remarkable scattering pattern when the sample was at a temperature well below T_g at 30°C and the incident angle was set to the first resonance mode. In the GISAXS patterns from particles confined within a disordered monolayer, the scattering intensity profile in the q_y direction reveals lateral correlation of the particles, while that in the q_z -direction yields information concerning the form factor in a direction normal to the surface. With the sample itself as the Type I waveguide, there are many distinct advantages. Firstly, no coupling is needed to port the x-ray beam from the waveguide. Therefore, there won't be any efficiency loss due to the coupling. Secondly, with the REXS effect, not only does the GISAXS signal become greatly enhanced inside the film due to the enhanced E-field intensity at the nanoparticle locations, but also the scattered x-rays exit the film only in certain discrete modes at a set of distinct angles. The values of these angles are equal to the incident angles at which REXS occurs in the thin film demonstrating beautiful optical reciprocity. At these exit angles, the measured scattering intensity is enhanced once more by multiple interference (analogous to the incident x-ray enhancement) of the scattered photons between the two interfaces of the nanocomposite film. To illustrate the second enhancement effect, a more rigorous simulation of the scattering pattern based on the distorted wave Born approximation (DWBA), shown in Fig. 1C, further demonstrates its excellent agreement with the measured data.

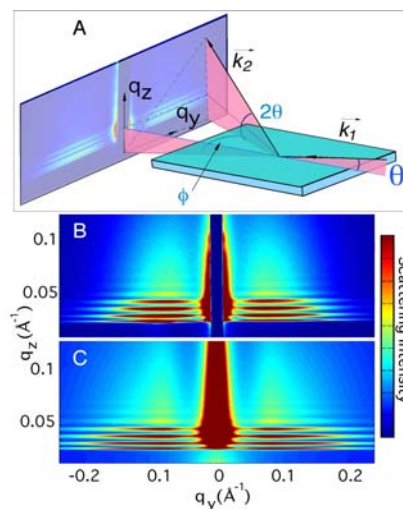


Figure 1. REX-GISAXS measurements: (A) Schematic. The incident and scattered wave vectors are k_1 and k_2 , θ is the grazing-incidence angle of the x-ray beam, ϕ and 2θ are, respectively, the scattering angles in and out of the scattering plane, q_y and q_z are, respectively, the lateral and vertical components of the momentum transfer; (B) and (C) Measured and simulated reciprocal space q_y - q_z color map of GISAXS pattern from an as-deposited PtBA sandwich sample.

Upon annealing well above T_g at 75°C , the lateral motion of the nanoparticles diffusing through the polymer matrix became evident. If the diffusion of nanoparticles were random as in Brownian motion, no change would be observed in the GISAXS spectra with time. The broadening of the intensity distribution along q_y as a function of annealing time implies that the lateral diffusion of the Au nanoparticles in the PtBA matrix is dominated by other mechanism. The driving force for the motion of

nanoparticles must be attributed to the attractive van der Waals interaction between the Au nanoparticles leading to their coalescence. It can also be deduced that the diffusion length within the time scale of the present measurement is less than the average particle separation since the average size of the Au nanoparticles has not changed. Thus, this would manifest in GISAXS as the average particle separation remaining the same accompanied by an increase in the distribution in the particle separation (σ_d). The resultant change in σ_d is a direct measure of the diffusion length of the nanoparticles. The nanoparticle diffusion or the coalescence coefficient can be defined as $D = \langle \sigma_d^2 \rangle / \Delta t$, where σ_d^2 is the mean square displacement of the nanoparticles over time Δt . Plots of the mean square displacement of the Au nanoparticles (in the lateral direction) vs. the annealing time (t) at the temperatures 65°C and 75°C are shown in Figs. 2A and 2B, respectively. For comparison, the mean square displacement of the Au nanoparticles in the out-of-plane direction measured precisely in a separate experiment is also shown. From a linear fit to the σ_d^2 - t plot, the diffusion coefficient at 75°C is determined to be $4 \times 10^{-17} \text{ cm}^2/\text{sec}$ in the lateral direction as opposed to $3 \times 10^{-18} \text{ cm}^2/\text{sec}$ in the out-of-plane direction.³ The much faster lateral motion of the Au nanoparticles and their tendency to coalesce could be attributed to the following factors: (i) the correlation between the Au nanoparticles exists only in the lateral direction as in a monolayer form, (ii) confinement of the nanoparticles in polymeric films with thicknesses only several times larger the R_g and a finite shear modulus of the highly viscous polymer owing to the viscoelastic nature of the polymer thin films results in the Au nanoparticles being dragged by the polymer chains.

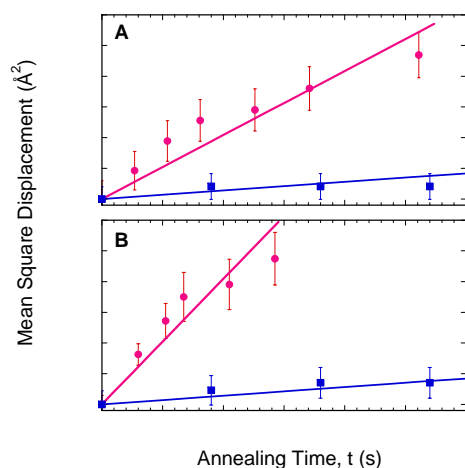


Figure 2. Mean-square-displacement of the Au nanoparticles in the lateral direction vs. the annealing time at temperatures 65°C (A) and 75°C (B). For comparison, the MSD as a function of time in the vertical direction measured using the technique of x-ray standing waves is also shown.

In the case of the dynamic assembling of the nanoparticle crystal superlattices, the process can be seen by positioning the incident beam at the bottom centre of the droplet to accommodate the changing meniscus of the droplet as it evaporates. Figure 3 shows a typical time evolution of the SAXS patterns after the droplet is deposited on the substrate. The droplet was evaporated in air at room temperature (30°C) under normal air circulation condition. The initial thickness of the droplet is typically more than 2 mm. The most dramatic change in the scattering patterns occurs in the first 10 minutes, corresponding to the time for the majority of the toluene solvent to evaporate, after which the droplet collapses into a thin liquid film less than 100 μm in thickness. No visible scattering pattern is observed in the first two

minutes indicating that initially there are no ordered superstructures in the droplet (Figure 3A). After that, an elliptically shaped diffraction ring is observed (Figure 3B). The section of the scattering ring near $q_y=0$ gradually becomes more diffuse in the q_x -direction and eventually disappears, while the intensity of the scattering corresponding to the in-plane long-range order increases dramatically (Figures 3C-3D). The scattering pattern in Figure 3D remains unchanged for hours during which a thin liquid film with a high concentration of dodecanethiol remains on the substrate surface. To illustrate the kinetics of the nanocrystal array growth, Figure 3E shows the experimental time evolution of the intensity of the (10) powder diffraction peak at $q_x=0$, plotted in natural log format. The scattering intensity increase exponentially with time before becoming saturated after 8 minutes (data not shown).

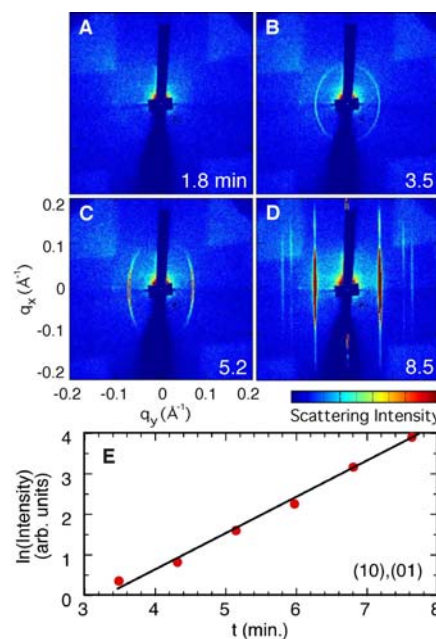


Figure 3. *In situ* SAXS patterns (A-D) of 2D NCSs formation during the droplet evaporation measured with a narrow x-ray beam at various time instances. Time in units of minutes is in reference to the deposition of colloid droplet onto the Si₃N₄ substrate. The exposure time for each frame on the image plate detector was 3 seconds. In this experiment, the average diameter of the nanocrystals is 7.5 nm determined by TEM. The visible cross bar feature in each frame is the shadow image of the beam stop, which was used to reduce the strong incident and specularly reflected beams; (E) Time-evolution of the normalized scattering intensity of the monolayer powder diffraction peak for (10) powder diffraction peak. The intensity (plotted in natural log scale) increases exponentially (solid line is a linear fit to the data) as soon as the formation of the ordered monolayer occurs (> 4 min). After 8 minutes, the intensity saturates indicating that self-assembly is completed in the area that is exposed to the x-ray beam. Data is not shown here due to the difficulty of determining the angle precisely for normalization.

Conclusions

It is the first time that in-plane nanoparticle motion has been elucidated in real time thanks to the resonance-enhancement in the sample-based wave-guide. In order to form laterally ordered nanostructures, it is important to have larger in-plane mobility. Dispersing the nanoparticles in a confined geometry is the key aspect to lateral ordering of the nanoparticles if a template presents. This study could thereby lead to a better understanding towards synthesizing controlled nanostructures for microelectronic applications. We note that the diffusive properties of these

nanoparticles in ultrathin polymer films can differ considerably from those in bulk polymers due to both the confined geometry in films with a thickness of only a few radius of gyration (R_g) of the polymer and interfacial interactions. Introducing small-sized nanoparticles or even no strongly scattering particles is essential so that properties of the polymer matrices are least perturbed. This nanoprobe of x-rays resulted from the resonance-enhancement can also be extended to study the dynamics of the nanoparticles over shorter time scales (milliseconds) during the initial diffusion through Brownian motion, by probing the time-correlated speckle patterns of coherent x-ray scattering from the nanoparticles in ultrathin films. This will also throw light on various fundamental problems, such as elucidating glass-transitions in polymer films.

In the case of the kinetics of the 2D nanoparticle superlattices self-assembly, the present measurements suggest kinetics of evaporation can strongly affect the structure of nanocrystal superlattices. 2D NCSs can form at the liquid-air interface if the evaporation is faster enough so that nanocrystals become accumulated at the liquid-air interface, whereas under a slow evaporation condition, nanocrystals can diffuse away from the interface and 3D NCSs can form in the droplet once the overall concentration of nanocrystals exceeds the crystallization limit. However, determining the evaporation boundary between these two cases requires a more quantitative monitoring of evaporation rate. Nevertheless, our in situ SAXS experiments have revealed for the first time that kinetics plays a significant role in macroscopic pattern formation using nanocrystal building blocks.

Acknowledgement. The collaborators of the research work include Suresh Narayanan, Xiao-Min Lin, Dong R. Lee of the ANL, Sunil Sinha of Univ. of California at San Diego and Rodney Guico and Ken Shull of Northwestern University. The author also thanks A. Gibaud and H. Jaeger for their discussions. This work and the use of the APS are supported by the U.S. Department of Energy under contract W-31-109-ENG-38.

References

- (1) Narayanan, S.; Lee, D.R.; Guico, R.; Sinha, S.K.; Wang, J. Submitted.
- (2) Narayanan, S.; Wang, J.; Lin, X.-M. *Phys. Rev. Lett.* **2004**, 93, 135503.
- (3) Guico, R.S.; Narayanan, S.; Wang, J.; Shull, K.R. *Macromolecule* **2004**, 37, 8357.

ANOMALOUS GRAZING INCIDENCE SMALL-ANGLE X-RAY SCATTERING STUDIES OF PLATINUM NANOPARTICLES FORMED BY CLUSTER DEPOSITION

Byeongdu Lee¹, Sönke Seifert¹, Stephen J. Riley^{2#}, George Y. Tikhonov², Nancy A. Tomczyk², Stefan Vajda², and Randall E. Winans^{1,2}

¹Experimental Facility Division and ²Chemistry Division, Argonne National Laboratory, 9700 South Cass Avenue, Argonne, Illinois 60439, USA.

Introduction

Metallic nanoparticles have been intensively studied for their optical, electronic and catalytic properties (see for example 1-2). These studies have shown that, for example, the catalytic activity and selectivity of the nanoparticles strongly depend on particle size, composition and shape, as well as the substrate material.² These extraordinary catalytic properties can be strongly altered, and the catalytic activity can be lost due to the sintering process taking place at elevated temperatures or upon exposure to mixtures of reactive gases.³ Therefore, size and shape measurements of the metallic nanoparticles in certain matrixes or on the substrates are indispensable in determining their physical properties. Grazing incidence small-angle x-ray scattering (GISAXS), which is an emerging technique for studying the shapes, sizes and spatial correlation of nanoparticles on the substrate,⁴ as well as in the substrate,⁵ can be used in combination with the anomalous technique.

A problem with GISAXS is a lack of a quantitative background subtraction method. When nanoparticles are supported on or buried in the substrate, scatterings from the substrate structures, such as surface roughness and morphological structures, are unavoidably mixed with that from particles except when the concentration of the studied particles is much higher than that of others. Up to now, scattering from substrate roughness, which is the one of the common sources of background, has been estimated and subtracted from the total signal by an approximation based on well-known power law behaviors.⁶ However, as the particle size becomes as small as several Å, a range comparable to that of the surface roughness, it is difficult to separate the background from the signal.

In this paper, we will show a way to differentiate the scattering of the particles from the other types of scattering, such as substrate roughness, using anomalous GISAXS (AGISAXS). We report the first AGISAXS results on Pt nanoparticles produced by the deposition of clusters on a SiO₂/Si(111) substrate.

Experimental

Pt samples. A beam of platinum clusters was produced in a cluster source with 1 cm channel length by vaporizing the metal from a platinum rod with a frequency-doubled YAG laser operating at a repetition rate of 50 Hz and using helium as a carrier gas. A substrate holder, capable of holding up to six substrates, was mounted on a translation stage and positioned at a distance of 5 cm from the nozzle of the source. Using a mask placed in front of the substrate, a 5.2-mm-diameter area of the substrate was exposed to the cluster beam. In this arrangement, the full distribution of clusters produced in the source was used for deposition. The substrate was a naturally oxidized silicon wafer (SiO₂/Si(111)). The degree of coverage of the substrate surface with clusters was controlled by varying the number of shots of the 50 Hz vaporization laser applied on the metal target rod (see Table 1). Samples with surface coverage up to 1.7×10^{16} Pt atoms/cm² were prepared in order to study the effect of the level surface coverage on the size of the nanoparticles formed on the SiO₂/Si(111) substrate.

AGISAXS measurement. The AGISAXS experiments were performed at the beamline 12ID-C at the Advanced Photon Source (APS) at Argonne National Laboratory using monochromatic x-ray energies near the *L*₃-absorption edge of Pt (*E*=11.564 keV). Before the scattering measurement, energies were calibrated by using the absorption edge of a standard Pt foil. Three detectors were used: an ion chamber for the measurement of incoming beam flux, a pin diode for the transmitted or reflected primary beam, and a 2D MarCCD(2k x 2k pixel) for AGISAXS images. The incident angle was kept at 0.14°, close to the critical angle of the SiO₂/Si(111) substrate for total reflection. A beam stop masked the intense specularly reflected beam and the diffuse scattering along the plane of specular x-ray beam. The data were corrected for dark current, nonuniform intensity, and pixel distortion. The camera length was calibrated using a standard (silver behenate) with known lattice spacing.

Results and Discussion

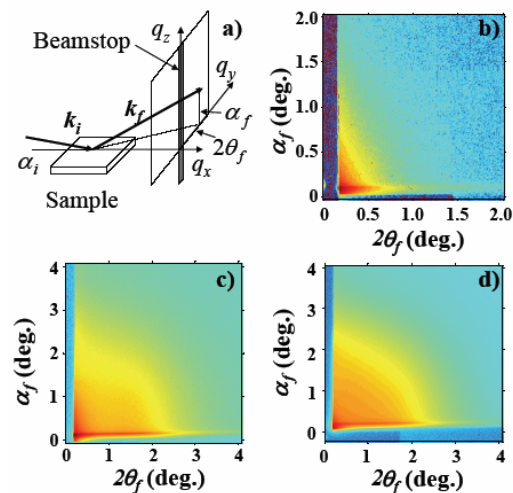


Figure 1. The geometry of GISAXS (a) and GISAXS images in log scales of SiO₂/Si(111) substrate (b), sample 3 (c) and sample 4 (d).

Figure 1(a) shows the geometry of GISAXS. The incident and exit x-ray beam is characterized by the wave vector k_i and k_f defined by the in-plane and out-of-plane angles, $2\theta_f$, α_i and α_f respectively. Figure 1(b)-(d) shows the scattering from a bare Si wafer, sample 3 and 4, respectively. The in-plane intensity in Fig.1(b) is comparable to the particle scattering when the particle size and concentration are small, as shown in Fig.1(c) and (d). This scattering from the surface roughness originates from the contrast between Si/SiO₂ and the vacuum. Thus it is strongest at the critical angle of Si of about 0.14° and is elongated along the out-of-plane direction. The surface roughness could be modeled as randomly positioned polydisperse corn-shaped particles. This model generates a similar pattern, as shown in Fig. 1(b).

We measured nine AGISAXS patterns for all samples near the *L*₃-absorption edge of Pt and 200 eV above the edge, which makes it possible to vary the contrast for scattering of that particular element. At the energy of the Pt *L*₃-edge, SAXS intensity of Pt clusters is minimized but is maximized below and above the edge. Fluorescence increases abruptly just above the edge. Figure 2 shows 1D profiles measured at two different energies of 11.342 and 11.564 keV, which will be designated as *E_L* and *E_H*, respectively. Even though it is difficult to see in the images in Fig. 1, the surface roughness scattering, which is energy independent, is easily determined in the horizontal cut at an exit angle of $\alpha_f = 0.14^\circ$ and shows a power-law slope of 2.

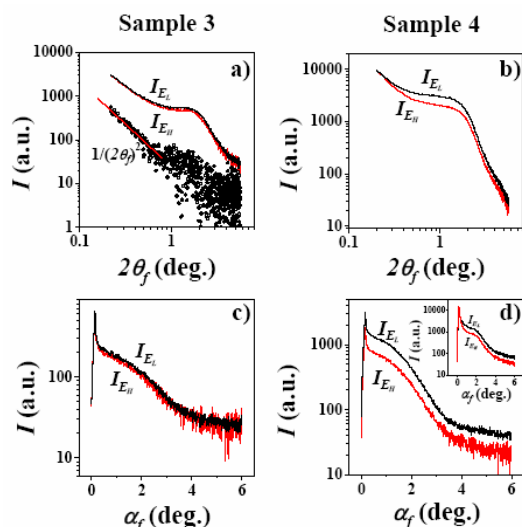


Figure 2. Fluorescence-subtracted horizontal cuts (a) and (b) at $\alpha_f = 0.14^\circ$, and vertical cuts (c) and (d) at $2\theta_f = 1^\circ$ of sample 3(a), (c) and sample 4(b), (d). Symbol data in (a) is the particle-scattering subtracted horizontal cut. Inset in (d) is the vertical cut at $2\theta_f = 0.217^\circ$.

For sample 1, the particle scattering occurred as a broad vertical rod, which corresponds to the interparticle distance in the plane. Its maximum is at about $2\theta_f = 1.7^\circ$ and shows a small energy dependence in the horizontal cut. For sample 2, the particle scattering is broader and overlaps with the scattering from the surface roughness and is more pronounced than that of sample 1 for the higher concentrations of particles. This anomalous effect is not clear in the vertical cuts at $2\theta_f = 1^\circ$ shown in Fig. 2(c) and (d). The two patterns measured at different x-ray energies are the same in shape and only differ in intensity, whereas the vertical cuts at $2\theta_f = 0.217^\circ$ plotted in inset of Fig. 2(d) show a clear energy independence near the critical angle of $\alpha_f = 0.14^\circ$. As the scattering pattern from the bare substrate in Fig. 1(b) shows, the roughness scattering is dominant in the small-angle region. As expected, sample 2, which has 2.5 times the number of shots as sample 1, shows a larger difference. The surface roughness scattering was negligible for sample 6, which has the largest number of Pt atoms in this experiment (the exact numbers are found in Table 1) and shows the critical angle shift to $\alpha_f = 0.29^\circ$, which is about 75% of the critical angle of pure Pt (the calculated critical angle of the Pt foil is 0.4°). The scattering from Pt particles is extracted by the subtraction of both backgrounds, which are the surface roughness scattering and the fluorescence measured at energies at E_L and E_H , as explained above, and are fitted by the polydisperse cylinder model with an assumption of coupling height with radius and distorted wave Born approximation for the reflection and refraction effect of a x-ray beam.⁴⁻⁶

Table 1 shows the summary of the fitting and Guinier analysis results. The calculated radii of gyration are close to those obtained from Guinier analysis. As the number of shots is increased, the size of the particles increases. Interparticle distances (D) become longer rather than shorter even though the populations of particles are increased, which also indicates that the islands formed by the cluster aggregation become larger. Interestingly height/radius (H/R) ratios increased, which means the small plate-like shapes of Pt clusters at a low number of shots become larger and become isotropic. Pt particles grown on different substrates are found in the literature.^{7,8} Though their sizes are bigger than a couple of nanometers, they clearly show

the substrate effect on island growth. On the substrate of γ - $\text{Al}_2\text{O}_3(111)/\text{NiAl}(111)$, which strongly interacts with a Pt cluster, islands grow epitaxially and their H/R ratio does not change.⁷ On the other substrate of amorphous SiO_2 , of which the surface energy is about 1.5 J/m^2 and is roughly 50% of that of Pt, they grow randomly.⁸ Our results interestingly tell that Pt islands are plate-like if their sizes are smaller than 1-2 nm even though they are randomly oriented.

Table 1. GISAXS results from best fits and Guinier analysis for Pt clusters deposited on a $\text{SiO}_2/\text{Si}(111)$ substrate with different levels of initial surface coverage. The parameter r_0 is the radius and its deviation σ from the cylinder model. The calculated radii of gyration from the fitted distribution is $R_{g,c}$ and that from the Guinier analysis is $R_{g,G}$. The interparticle distance obtained by maximum position of the structure factor is D .

S.	Surface coverage		Radius				Height		$D(\text{\AA})$
	# of shots	Pt atoms/cm ²	$r_0(\text{\AA})$	σ	$R_{g,c}(\text{\AA})$	$R_{g,G}(\text{\AA})$	H/R	$2R_{g,G}(\text{\AA})$	
1	100	1.4×10^{14}	6.4	0.33	8.2	7.8	1.16	11.7	29.1 ± 1
2	250	3.4×10^{15}	8.9	0.35	12.1	10.5	1.16	12.5	31 ± 3
3	500	6.8×10^{15}	6.7	0.59	18.2	17.3	1.4	27.2	-
4	1000	1.4×10^{16}	-	-	-	28.4	-	>54	-

Conclusions

In summary, we have shown that AGISAXS is a powerful method to understand GISAXS patterns containing mixed scattering from surface roughness and from supported particles. Particle scattering is separated quite well from surface-roughness scattering, as well as particle fluorescence. The AGISAXS technique allowed measurement of the particle size of less than 1 nm without any assumptions or sample distortion. This method can be applied and extended to the study of multicomponent systems or multilayered systems with embedded particles.

Acknowledgment. The authors express thanks for use of the APS and work at Argonne, which is supported by the U.S. Department of Energy, Office of Basic Energy Sciences, Division of Chemical Sciences, Geosciences, and Biosciences under Contract No. W-31-109-ENG-38. They also thank Don Graczyk and coworkers for performing the weight analysis of platinum deposits.

References

- Redl, F. X.; Cho, K.-S.; Murray, C. B.; and O'Brien, S. *Nature* **2003**, 423, 968.
- Wallace, W.T.; and Whetten, R. L. *J. Am. Chem. Soc.* **2002**, 124, 7499.
- Valden, M.; Pak, S.; Lai, X.; and Goodman, D. W. *Catal. Lett.* **1998**, 56, 7.
- Renaud, G.; Lazzari, R.; Revenant, C.; Barbier, A.; Noblet, M.; Ulrich, O.; Leroy, F.; Jupille, J.; Borensztein, Y.; Henry, C. R.; Deville, J.-P.; Scheurer, F.; Mane-Mane, J.; and Fruchart, O. *Science* **2003**, 300, 1416.
- Rauscher, M.; Salditt, T.; and Spohn, H. *Phys. Rev. B.* **1995**, 52, 16855.
- Sinha, S. K.; Sirota, E. B.; Garoff, S.; and Stanley, H. B. *Phys. Rev. B.* **1988**, 38, 2297.
- Klimenkov, M.; Kuhlbeck, H.; and Nepijko, S. A. *Surf. Sci.* **2003**, 539, 31.
- Phillips, M. A.; Ramaswamy, V.; Clemens, B. M.; and Nix, W. D. *J. Mater. Res.* **2000**, 15, 2540.
- Vajda, S.; Winans, R.E.; Elam, J.W.; Lee, B.; Pellin, M.J.; Riley, S.J.; Seifert, S.; Tikhonov, G.Y.; Tomczyk, N.A., *submitted*

IN SITU GISAXS STUDIES OF THE THERMAL STABILITY AND TEMPERATURE INDUCED GROWTH OF SUPPORTED CLUSTER-BASED PLATINUM AND GOLD NANOPARTICLES

Stefan Vajda^{1*}, Randall E. Winans^{1,3}, Jeffrey W. Elam², Byeongdu Lee³, Michael J. Pellin⁴, Stephen J. Riley¹, Sönke Seifert³, George Y. Tikhonov¹ and Nancy A. Tomczyk¹,

¹Chemistry Division, Energy Systems Division, ³Experimental Facility Division, and ⁴Materials Science Division Argonne National Laboratory, 9700 South Cass Avenue, Argonne, Illinois 60439, USA

Introduction

The physical and chemical properties of metallic nanoparticles have been intensively studied in the past two decades. These studies have shown that, for example, the reactivity of nanoparticles consisting of only a handful of atoms strongly depends on the particle size, composition as well as on the material of the support. The Achilles heel of these systems, including particles with up to a few nanometer diameter is their increased mobility at elevated temperatures or when exposed to mixtures of reactive gases. The mobility of the particles may cause their aggregation leading to the alteration or complete loss of their size-specific properties¹⁻³.

In the presented paper, the issue of thermal stability and kinetics of aggregation of supported platinum and gold nanoparticles produced by cluster deposition on oxide surfaces is addressed as a function of the level of surface coverage, temperature of the post-deposition heat treatment and time of heat treatment by employing synchrotron X-ray radiation. As support materials, naturally oxidized surface of silicon wafer (SiO₂/Si(111)) and 1 monolayer of alumina film grown by atomic layer deposition technique⁴ (Al₂O₃/SiO₂/Si(111)) were used for platinum and gold clusters, respectively.

Experimental

Production and deposition of Pt clusters. The experimental setup and the design of the cluster source has been described in details elsewhere^{5,6} and only details concerning the cluster deposition are given here. An oxidized surface of a silicon wafer (SiO₂/Si(111)) was used as the substrate for cluster deposition. The beam of platinum clusters was produced in a cluster source with 1 cm channel length by vaporizing the metal from a platinum rod with a frequency doubled YAG laser operating at a repetition rate of 50 Hz, and helium was used as a carrier gas. A substrate holder, capable of holding up to six substrates was mounted on a translation stage and positioned at a distance of 5 cm from the nozzle of the source. Using a mask placed in front of the substrate, a 5.2 mm diameter area of the substrate was exposed to the cluster beam. In this arrangement, the full distribution of clusters produced in the source was used for deposition. Samples with surface coverages ranging from 1.4×10¹⁴ to 1.4×10¹⁶ Pt atoms/cm² were produced.

Deposition of narrow size distributions of Au clusters. The continuous beam of gold clusters was generated in a high-throughput laser vaporization cluster source utilizing a Nd YAG laser operating at 4.5 kHz. The charged clusters were deflected into an ion-optics setup with an incorporated mass spectrometer. This setup allows the mass analysis of the cluster ions present in the beam as well as the pre-selection of narrow cluster distributions or clusters of one single size for deposition in the mass range up to 2000 amu (Au_n⁺, n=1,2,...10). In the experiments involving narrow gold cluster distributions, two to five dominant cluster sizes can be mass pre-

selected. As support, one atomic monolayer of Al₂O₃ on SiO₂/Si(111) prepared by atomic layer deposition was used.

GISAXS measurement. The GISAXS experiments were performed in a vacuum chamber equipped with a sample holder mounted on a goniometer. The sample holder is made of a brass rod with a milled flat surface on its end and with built-in heaters, allowing heating of the sample up to 500 °C. The samples were heated gradually in 20 °C increments with a 10 minute wait time between steps. During heat treatment, scattering data can be collected as a function of temperature. The kinetics of aggregation can be monitored in real time by heating up the sample to a desired temperature and monitoring the time evolution of the X-ray data. X-rays produced in an undulator (12.0 keV) pass through a double-crystal monochromator ($\Delta E/E \sim 10^{-4}$) and a focusing mirror. The beam was scattered off the surface of the sample at and near the critical angle of the silicon substrate. The scattered X-rays are detected by a nine-element mosaic CCD detector (150 x 150 mm) with a maximum resolution of 3000 x 3000 pixels.⁷ The data are analyzed by taking cuts in the q_{xy} direction for horizontal information and in the q_z direction for vertical information (see Figure 1). From these data the radius of gyration (R_g) was calculated using a Guinier analysis. Silver behenate is used to calibrate both horizontal and vertical q values for the given camera length.

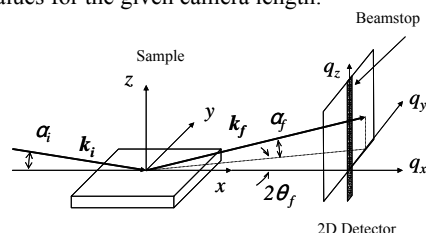


Figure 1. Schematic of GISAXS experiment. Incident X-ray beam (k_i) angle and scattered beam (k_f) are α_i and α_f respectively. Scattering vectors q are calculated from $(4\pi/\lambda)\sin\theta_f$ where θ_f is the scattering half angle and λ is the wavelength of the X-rays.

Results and Discussion

Thermal stability of supported Pt nanoparticles. The thermal stability region was determined on a sample of Pt nanoparticles with surface coverage 6.8×10^{14} ($\pm 10\%$) Pt atoms per cm², which corresponds to 34% of one atomic monolayer. Such level of surface coverage can lead to the agglomeration of the clusters upon landing with particles already formed on the support. In addition, the exposure of the sample to air during transport to the beam-line may cause additional aggregation as well. However, it has been shown that Pt clusters deposited onto a γ -Al₂O₃(111)/NiAl(110) substrate under high vacuum were not altered when transferred in air for TEM analysis.^{8,9} Pt clusters prepared from dendrimers and deposited onto silica were found to show only limited sintering at 425 °C under oxidation.¹⁰ Guinier analysis of the vertical slice of the X-ray scattering data collected at room temperature gives an $R_g = 11.1$ Å, while the horizontal slice yields $R_g = 11.6$ Å.¹¹ Within the experimental deviation, the particles are roughly spherical with a diameter of $d = 29.7$ Å ($d = 2 \times 1.29 \times R_g$). This size corresponds to a cluster containing approximately 900 Pt atoms. During heat treatment, the cluster size did not change until the temperature reached 320 °C, when the clusters began to grow parallel to the surface of the substrate in as is shown in Figure 2. There was no growth observed in the vertical direction. Thus, the agglomeration leads to the formation of oblate spheroids with the minor axis being equal to the original spheroids. The stability of the Pt particles may be due in part to the fact that they are dilute on the surface at the given surface coverage and in part due to strong interactions with the

support. The change of the particle size and shape as a function of coverage is summarized in Table 1 and shows an increase in mean

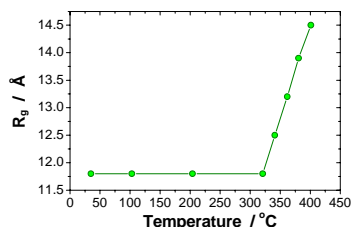


Figure 2. Change in radius of gyration calculated from horizontal slices as a function of temperature.

particle size with coverage. More cylindrical particles were observed at lower levels of coverage (samples 1 and 2), while more spherical particles were formed at higher levels of coverage (samples 3 and 4).

Table 1. Results from Guinier analysis for Pt nanoparticles formed by cluster deposition on SiO₂/Si(111) as a function of surface coverage. $R_{g,G\parallel}$ and $R_{g,G\perp}$ denotes the radii of gyration from the Guinier analysis of the horizontal and vertical cuts, respectively. h and d are the average height and width of the particles calculated as $2 \times 1.29 \times R_g$, h/d stands for the aspect ratio, D for the average interparticle separation.

Samp le #	Coverage (atoms/cm ²)	$R_{g,G\parallel}$ (Å)	$R_{g,G\perp}$ (Å)	h (Å)	d (Å)	h/d (Å)	D (Å)
1	1.4×10^{14}	7.8	5.8	15.0	20.1	0.8	29.1
2	3.4×10^{15}	10.5	6.3	16.2	27.1	0.6	31.3
3	6.8×10^{15}	17.3	13.6	35.0	44.6	0.8	-
4	1.4×10^{16}	28.4	>27	>70	-	-	-

Kinetics of Pt nanoparticle aggregation. Samples 1-4 were rapidly heated up to 400 °C and GISAXS images were recorded for up to 8 hours. The evolution of the average radii of gyration R_g is plotted in Figure 3. The results indicates a two-step agglomeration process with the first step completed within ~30 minutes.

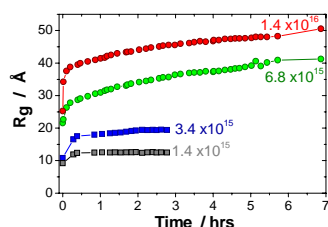


Figure 3. Change in radii of gyration of Pt nanoparticles supported on SiO₂/Si(111) at 400 °C as a function of time. The level of surface coverage is indicated in the plots as well.

Thermal stability of supported Au nanoparticles. A narrow gold cluster distribution with two dominant cluster sizes, Au₃ and Au₄ was deposited on 1 ML Al₂O₃/SiO₂/Si(111) support at a surface coverage equivalent of 15% of atomic monolayer. The flux of clusters landing on the substrate was monitored on-line during the deposition process using a picoammeter. The analysis of the GISAXS data recorded at room temperature showed that about 45% of the overall number of supported particles retained the initial size of the deposited clusters ($R_g=1.8\text{Å}$), the remaining fraction of particles had a radius of gyration $R_g=12.6\text{Å}$.

Figure 4 shows the change of the average radii of gyration of the supported gold particles as a function of temperature. The results

indicate particles with initial spherical average shape, those retain their size and form up to about 180 °C, when a likely multi-step aggregation yielding oblate particles takes place.

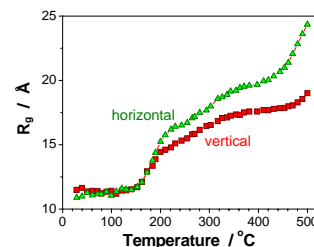


Figure 3. Change in the radii of gyration of Au nanoparticles supported on 1ML Al₂O₃/SiO₂/Si(111) as a function of temperature.

Conclusions. An unexpectedly high thermal stability of Pt nanoparticles preserving their original size up to about 320 °C was observed. Cylindrical particle shapes were observed at lower levels of surface coverage and more spherical forms at higher levels of coverage. The kinetics data indicate a two-step agglomeration process with final particle size determined by the level of surface coverage. In the case of the supported Au nanoparticles, the onset of aggregation takes place at approximately 180 °C and the particle shape evolves from spherical to oblate. These experiments demonstrate the powerful combination of cluster deposition, atomic layer deposition and synchrotron techniques, which can aid in characterization and design of new nanoparticle-support combinations with potential use, for example, in catalysis. Extended, element specific information on multi-component systems can be gained by using anomalous GISAXS¹².

Acknowledgments. This work was performed under the auspices of the U.S. Department of Energy, Office of Basic Energy Sciences, Division of Chemical Sciences, Geosciences, and Biosciences and use of the Advanced Photon Source was supported by BES-DOE all under contract number W-31-109-ENG-38. The authors thank Don Graczyk and coworkers for performing the weight analysis of platinum deposits. In memory: Steve Riley.

References

- Min, B. K.; Santra, A. K.; Goodman, D. W. *Catalysis Today* **2003**, 85, 113.
- Hayashi, K.; Horiuchi, T.; Suzuki, K.; Mori, T. *Catalysis Letters* **2002**, 78, 43.
- Chen, Z. X.; Smith, G. C.; Putman, C. A. J.; Voert, E. J. M. *Catalysis Letters* **1998**, 50, 49.
- George, S. M.; Ott, A. W. & Klaus, J. W. *Journal of Physical Chemistry* **100**, 13121-13131 (1996).
- Richtsmeier, S. C.; Parks, E. K.; Liu, K.; Pobo, L. G.; Riley, S. J. *Journal of Chemical Physics* **1985**, 82, 3659.
- Parks, E. K.; Weiller, B. H.; Bechthold, P. S.; Hoffman, W. F.; Nieman, G. C.; Pobo, L. G.; Riley, S. J. *Journal of Chemical Physics* **1988**, 88, 1622.
- Seifert, S.; Winans, R. E.; Tiede, D. M.; Thiagarajan, P. *Journal of Applied Crystallography* **2000**, 33, 782.
- Klimenkov, M.; Kuhlbeck, H.; Nepijko, S. A. *Surface Science* **2003**, 539, 31.
- Klimenkov, M.; Nepijko, S.; Kuhlbeck, H.; Baumer, M.; Schlögl, R.; Freund, H. J. *Surface Science* **1997**, 391, 27.
- Deutsch, D. S.; Lafaye, G.; Liu, D. X.; Chandler, B.; Williams, C. T.; Amiridis, M. D. *Catalysis Letters* **2004**, 97, 139.
- Winans, R.E.; Vajda, S.; Lee, B.; Riley, S.J.; Seifert, S.; Tikhonov, G.Y.; Tomczyk, N.A., *Journal of Physical Chemistry B*, ASAP web release 30-Oct-2004, (Letter) DOI: 10.1021/jp045549p
- Lee, B.; Seifert, S.; Riley, S.J.; Tikhonov, G.Y.; Tomczyk, N.A.; Vajda, S.; and Winans, R.E., *submitted*

IN SITU SAXS AND GISAXS STUDIES OF POLYMER/NANOCOMPOSITE MEMBRANES FOR ENERGY APPLICATIONS

Giselle Sandt¹, Kathleen A. Carrado¹, Riza Kizilel², Norma Castagnola¹, Byeongdu Lee³, and Sönke Seifert³

(1) Chemistry Division, Argonne National Laboratory, 9700 South Cass Ave, Argonne, IL 60439, (2) Chemical and Environmental Engineering Department, Illinois Institute of Technology, (3) Experimental Facilities Division, Argonne National Laboratory

Abstract

In recent years a new class of materials has been developed by dispersing layered silicates with polymers at the nanoscale level. We have prepared a series of nanocomposites containing PEO intercalated in the layers of hectorite clays. These clays are composed of two tetrahedral silicate layers sandwiching a central octahedral layer in a so-called 2:1 arrangement. Isomorphous substitutions in the lattice of Li(I) for Mg (II) in the octahedral layers cause an overall negative charge that is compensated by the presence of interlayer, or gallery, cations. Interlayer water is also present and the cations are easily exchangeable. Catalytic nanocomposite membranes have also been prepared by ion exchanging Pt^{2+} for Li^+ in synthetic hectorite clay and dispersing this inorganic component within a polymeric matrix. Transparent, self-supporting membranes from the polymer-clay nanocomposite are then made. These membranes have been characterized by TEM and in situ techniques such as SAXS and GISAXS.

Introduction

In recent years, a new class of materials has been developed by dispersing layered silicates with polymers at the nanoscale level. These new materials have attracted wide interest because they often exhibit chemical and physical characteristics that are very different from the starting materials [1, 2]. In some cases, the silicates and polymers exist as alternating layers of inorganic and organic [3]. Nanocomposite materials of PEO and phyllosilicates were first suggested by Ruiz-Hitzky and Aranda [4] as candidates for polymer electrolytes. Within these materials, the polymer chains are intercalated between the silicate layers. The polymer chains then provide a mobile matrix in which cations are able to move. A considerable amount of interest has been shown in nanocomposites of PEO and montmorillonite, a layered aluminosilicate clay. When this composite contains LiBF_4 , it displays conductivities up to 2 orders of magnitude larger than that of PEO itself at ambient temperatures. However, the addition of lithium salts, which is needed to obtain such conductivity values, is not desirable for two reasons; the first relates to a more complicated synthetic route and the second is that transference numbers are not unity since in this case both cations and anions move.

We have prepared a series of nanocomposites containing PEO intercalated in the layers of hectorite clays. Catalytic nanocomposite membranes have also been prepared by dispersing the clay in water with a platinum salt and water-soluble polymer. Transparent, self-supporting membranes from the polymer-clay nanocomposite are then made. The resulting films are then reduced under H_2 at 150°C for 2-4 hr, turning black upon reduction. The final film contains Pt(0) at 2.4 wt% loading levels. XRD shows development of Pt(0) by the appearance of crystalline peaks upon reduction. A lineshape analysis using the Scherrer equation of the (220) peak shows Pt(0) particles from 3.8 nm to 7.5 nm depending upon processing conditions. These values are confirmed by TEM,

and a high dispersion of the metal throughout the matrix is evident. XRD and TGA confirm that PEO is stable to the processing conditions.

This paper will describe the results from in situ small angle x-ray scattering (SAXS) studies that were employed to follow (a) the stability of polymer-clay nanocomposite films with temperature, (b) platinum metal reduction as the films were heated, and (c) grazing incidence SAXS (GISAXS) studies of the films were attempted for the first time.

Experimental

Preparation of the SLH clay via hydrothermal crystallization at 100°C of silica sol, magnesium hydroxide, and lithium fluoride can be found in detail in reference 1. Loading of Pt(II) salt was accomplished via a wet impregnation method by adding 0.5 gm clay to a 2.5 mM aqueous $\text{cis-Pt}(\text{NH}_3)_2\text{Cl}_2$ solution and stirring for 24 hr. This yields a material that has 4.65 wt% Pt. The impregnation method was followed rather than an ion-exchange method in order to ensure that all of the metal used was associated with the clay. The desired amount of PEO (100 000 average molecular weight, from Aldrich) was then added to either the pure clay or the Pt-salt-clay, and the mixture stirred for 24 hours. Mixtures contained 0.6, 0.8, 1.0, and 1.2 g of PEO/g of clay. Films were prepared by puddle-casting the slurries onto Teflon-coated glass plates and air-drying. Further drying was carried out at 120 °C under an inert atmosphere for at least 48 hours. The typical thickness of the films is about 40 μm . The reduction of Pt^{2+} to Pt(0) nanoclusters in the catalytic membranes is accomplished by thermal reduction under H_2 at temperatures higher than 120°C.

XRD patterns were recorded on a Rigaku Miniflex+ with $\text{Cu K}\alpha$ radiation, a 0.05 °2 θ step size, and 0.5 °2 θ scan rate; the films were held in a horizontally-mounted sample stage. Lateral crystallite size of the Pt(0) nanoclusters was estimated from the line broadening of the (220) reflection using the Scherrer equation; $L = .91\lambda/B\cos\theta_{\text{max}}$ where L = crystallite size in Å, $\lambda = \text{CuK}\alpha = 1.5405$ Å, $B = \sqrt{(B_{\text{obs}}^2 - b^2)}$; B_{obs} = FWHM (220) reflection in radians observed, b = FWHM instrumental correction (in this case Si(220) reflection).

TEM images were acquired using a FEI TECNAI F30ST operating at 300 kV with a CCD camera. One drop of Pt(0)-PCN slurry in MeOH (sonicated for 1 hr) was placed onto 3 mm holey carbon Cu grids; excess solution was removed and the grid dried at 100°C for 10 min. TGA was performed using an EXSTAR6000 Seiko Haake instrument at a heating rate of either 10°C/min (for pure clay) or 0.5°C/min (clay systems containing polymer) under 100 ml/min O_2 gas flow using 2-3 mg sample.

In situ SAXS and GISAXS were carried out at the Sector 12 of the Advanced Photon Source at Argonne National Laboratory. For the SAXS measurements, monochromatic x-rays (18 keV) were scattered and collected on a 15 x 15 cm² CCD camera. The scattering intensity is corrected for adsorption and instrument background. The differential scattering cross section is expressed as a function of scattering vector q . The value of q is proportional to the inverse of the length scale (\AA^{-1}). The instrument was operated with a sample to operator detector distances of 228 cm and 390 mm to obtain data at $0.01 < q < 0.3 \text{ \AA}^{-1}$ and at $0.08 < q < 2.3 \text{ \AA}^{-1}$, respectively. For these studies, a specially designed sample holder was used to heat the sample and collect SAXS data at the same time. Films of about 1.25 cm in diameter and 40 μm in thickness were placed in the sample holder and held using Kapton tape. The furnace temperature program was set to ramp from room temperature to 200°C at 5°C/min, and the gas flow of H_2 and He was started at room temperature. For the GISAXS experiments, the membranes were deposited on a silica substrate and an incident angle of 0.15°.

Results

Figure 1 shows SAXS data obtained from a film made of PEO/SLH 1.2:1 mass ratio. The data was collected at different room temperatures, as shown in the inset. It is clear that the structure of the polymer has changed as indicated by the near complete disappearance of the PEO crystalline peaks. It is therefore assumed that the polymer chains have relaxed inside the clay layers. Other evidence of such relaxation is the decrease in d001 spacing, which indicates a more dense polymer phase. Under these circumstances, the polymer matrix is more mobile and the lithium ions associated with the polymer can have higher transference number, leading to a higher conductivity.

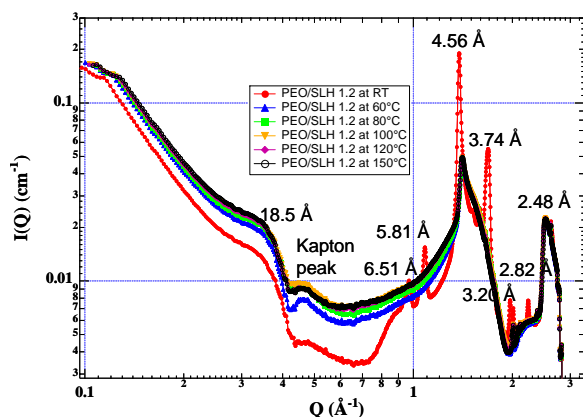


Figure 1. In situ SAXS of a SLH:PEO 1.2:1 ratio film.

Figure 2 shows a high resolution TEM image of a membrane made of PEO:clay in a 1:1 weight ratio. Small 15 nm disks due to silica spheres are visible throughout the background. Croce et al [5] demonstrated that by dispersing selected low-particle size ceramic powders (γ -LiAlO or TiO_2) in PEO-LiX polymer electrolytes nanocomposites, enhanced interfacial stability as well as improved conductivity at ambient temperature was achieved. Commercially available laponite such as that used by Doeff [6] does not contain silica particles. As discussed by Mermut and Cano [7], other clay materials such as those recently used by Giannelis et al [8], contain negligible amounts of silica impurities.

Figure 3 shows the Arrhenius conductivity plot in the temperature range from room temperature to 150 °C for the sample prepared with a PEO:SLH 0.6:1 mass ratio and different silica precursors as indicated in the graph inset. The conductivity of the polymer nanocomposites increases as the sample is heated from room temperature (26.0 °C) to 150 °C. As discussed by Sandí et al [3] the slope change or break that occurs in many polymeric materials is absent in our system.

Figure 4 shows XRD patterns for a Pt-salt-PEO-SLH film both before and after reduction to Pt(0) in H_2 . The clay d(001) basal spacing at 2.0 nm ($4.4^\circ 2\theta$) indicates incorporation of a bilayer of PEO chains (the clay layer itself is 0.96 nm and each PEO chain is approximately 0.45 nm). The basal spacing value does not change position upon reduction, showing the stability of the PEO chains in the gallery region. Several higher orders of reflection (002, 004, 006) occur due to the layered, film arrangement and subsequent high degree of orientation of the hectorite sheets. Three new peaks due to Pt(0) metal appear upon reduction at 40.1 , 46.4 , and $67.6^\circ 2\theta$. The crystallite size of the Pt(0) nanoclusters is estimated from the line broadening of the latter (220) reflection, using the Scherrer equation as described in the experimental section 11, at 3.8 nm diameter for this particular sample. Peaks due to PEO are also observed as indicated in Fig. 4, which do not shift or decrease upon reduction.

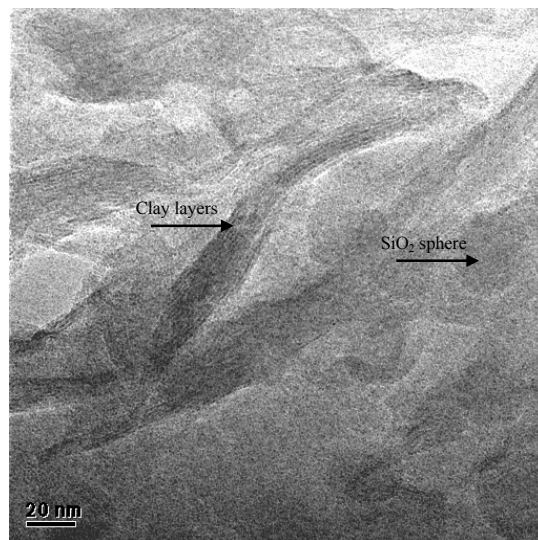


Figure 2. High resolution TEM of a 1:1 PEO:SLH mass ratio nanocomposite membrane. The arrows point to a silica sphere and to well-defined clay layers.

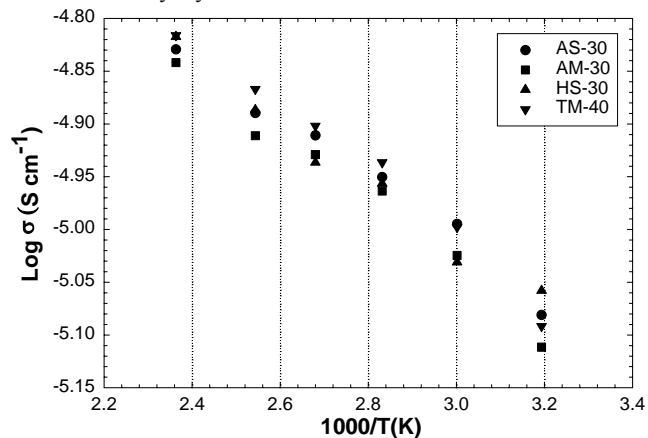


Figure 3. Arrhenius conductivity plots as a function of temperature of nanocomposite membranes with nominal composition PEO:SLH 1.2:1 mass ratio, derived from different silica sources as indicated in the graph inset. AS-30, AM-30, and HS-30= 15 nm silica sphere size; TM-40= 24 nm.

TEM images of a Pt(0)-PEO-SLH are shown in Figure 5. The difference in contrast between the clay (as well as silica) and Pt(0) particles is clearly evident, making it easy to distinguish the metal. TEM also clearly shows the highly dispersed nature of the metal nanoparticles throughout the matrix, as well as the fact that some polydispersity in particle size is evident. While the majority of Pt(0) particles are spherical, a minority appears as more oblong in shape. The inset of Fig. 5 shows a HR-TEM image of a single 5 nm nanoparticle with the crystal lattice plane fringes apparent.

The Pt(II) reduction process was monitored in situ via small angle x-ray scattering (SAXS) under either H_2 (reducing) or He (inert) flow at different temperatures. The SAXS curves were modeled using the general unified fit (GUF), which is a general equation developed to describe scattering functions that contain multiple length-scales where scattering from individual particles as well as from their aggregates are present.

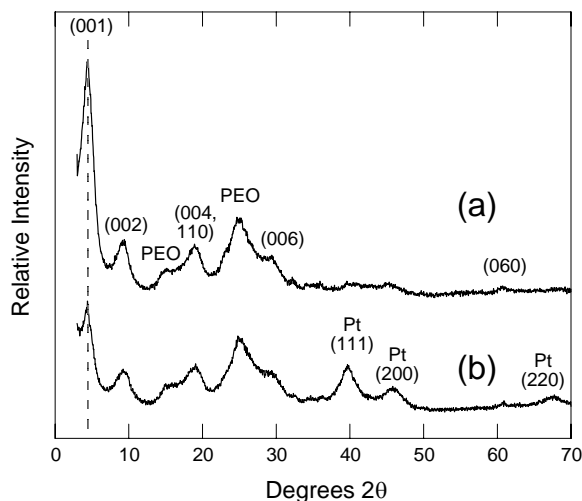


Figure 4. XRD of (a) Pt(II) salt-PEO-PCN film before reduction and (b) Pt(0)-PEO-PCN film after reduction. Reflections in (a) are for hectorite clay and PEO as indicated; reflections in (b) are for Pt(0) as indicated, as well as for clay and PEO.

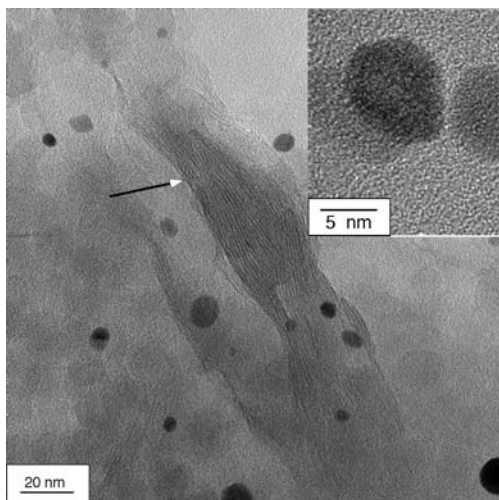


Figure 5. TEM images of Pt(0)-PEO-SLH. The white-tipped arrow indicates several stacked 1-nm clay layers.

Heating under H_2 at moderate temperatures ($>100^\circ\text{C}$) produces significant changes in the SAXS results, especially in the higher- Q regime (see Fig. 6). The GUF fits still extend over the entire range of the data. However, at $>100^\circ\text{C}$, the qualitative change in the data is accommodated in the GUF equation by two, instead of one, structural levels with two G , B , P , and R_g values. This additional length-scale is included in Table 1. It is presumed to arise from the reduction of Pt(II) to Pt(0) nanoclusters and the resultant scattering from these new particles. Diameters of the particles are calculated by multiplying the R_g by a constant of 2.6 ($R_g = R/1.29$ for spherical particles) and yield 4.8 nm at 120°C . Further heating to 200°C does not form significantly larger nanoclusters (the size increases by just 6% to 5.1 nm).

Figure 7 shows the R_g of the Pt particles formed upon the reduction of the polymeric catalytic membranes calculated by using GISAXS. The Pt particles start to form above 100°C and the radius reaches a plateau at about 175°C . The R_g is about 12 Å, which

correspond to a 3.1 nm diameter Pt particle ($R_g = R/1.29$ for spherical particles). These values are consistent with those calculated by XRD or TEM techniques. There is some variability on the diameter of the Pt particles calculated by SAXS or GISAXS, but they are within experimental error. Also, dilute H_2 was used for the GISAXS experiments and that lead to a smaller particle being formed. That might be an advantage for practical applications, where it is desirable to keep the particles separated for a more effective catalytic activity.

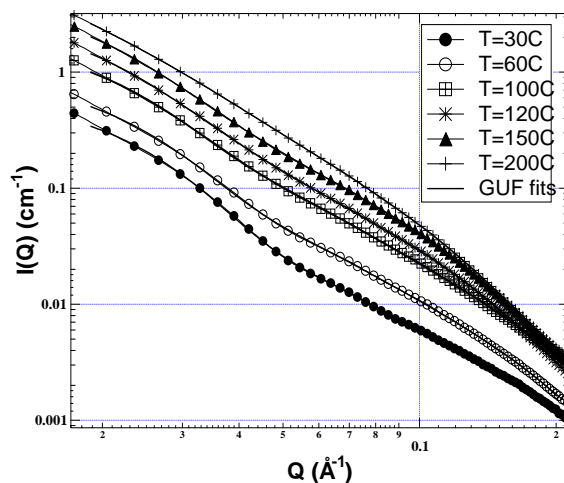


Figure 6. Log-log SAXS plot of a Pt-PEO-SLH film heated under H_2 flow with fits to the GUF equation. Curves $> 100^\circ\text{C}$ have been offset for clarity.

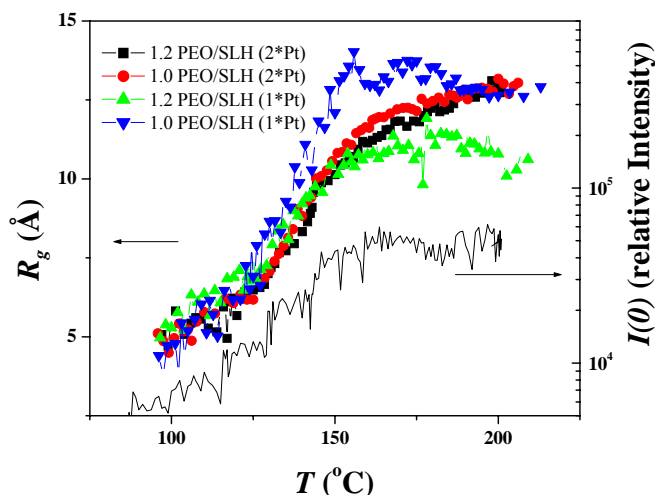


Figure 7. In situ GISAXS data of the Pt particle formation in catalytic membranes.

Conclusions

Transparent films made with synthetic lithium hectorite and intercalated PEO are obtained with excellent mechanical strength and with conductivity that is comparable to more traditional polymer electrolytes made with added lithium salts. Conductivity values, activation energies, and lithium transference numbers indicate that these membranes are single ion conductors with transference numbers close to unity. Polymer-clay nanocomposite films were also made containing Pt(0) metal nanoclusters by suspending a synthetic clay in an aqueous solution of Pt(II) salt and polyethylene oxide

(PEO), evaporating this solution to make 40-micron thick films, and reducing them under H₂ at 150°C for 2-4 hr. The final film contains Pt(0) at 2.4 wt% loading levels. XRD shows development of Pt(0) by the appearance of crystalline peaks upon reduction. In situ SAXS and GISAXS revealed the Pt particle diameter at about 3-5 nm, values consistent with XRD and TEM measurements. The efficacy of these metal nanoparticle polymer-clay nanocomposite films for use as membranes in gas separations and catalysis is currently under investigation. In addition, variables controlling the Pt(0) nanoparticle size and dispersion are being optimized.

Acknowledgement. This work was performed under the auspices of the Office of Basic Energy Sciences, Division of Chemical Sciences, Geosciences, and Biosciences, U.S. Department of Energy, under contract number W-31-109-ENG-38.

References

1. K. A. Carrado. *Appl. Clay Sci.* **17**, 1, 2000.
2. G. Sandí, H. Joachin, R. Kizilel, S. Seifert, and K.A. Carrado. *Chemistry of Materials* **15** (4), 838, 2003.
3. G. Sandí, K. A. Carrado, H. Joachin, W. Lu, and J. Prakash. *Journal of Power Sources*. **119-121**, 492, 2003.
4. E. Ruiz-Hitzky, P. Aranda. *Adv. Mater.* **2**, 545, 1990.
5. F. Croce, R. Curini, A. Martinelli, L. Persi, F. Ronci, B. B. Scrosati, and F. Croce, *J. Electrochem. Soc.*, **5**, 1718, 2000.
6. M. Doeff and J. S. Reed, *Solid State Ionics*, **113-115**, 109, 1998.
7. A. R. Mermut and A. F. Cano, *Clays and Clay Minerals*, 49, 381, 2001.
8. E. Hackett, E. Manias, and E. P. Giannelis, *Chem. Mater.*, **12**, 2161, 2000.

DIESEL SOOT IN THE LIGHT OF SYNCHROTRON RADIATION – A REVIEW OF USAXS, WAXS, AND NEXAFS DATA

Artur Braun¹, Soenke Seifert², ³Jan Ilavsky, ⁴Simon B. Mun, ⁵Steven Ehrlich, ⁶Sue Wirick, ⁷Alena Kubatova, ⁸Naresh Shah, ¹Frank E. Huggins, ⁸Kerry E. Kelly, ⁹Matti Maricq, ¹Gerald P. Huffman

¹Consortium for Fossil Fuel Sciences, University of Kentucky, Lexington KY, ²Chemical and Materials Technology, Argonne National Laboratory, Argonne IL, ³Advanced Photon Source, Argonne National Laboratory, Argonne IL, ⁴Advanced Light Source, Berkeley National Laboratory, Berkeley CA, ⁵National Synchrotron Light Source, Brookhaven National Laboratory, ⁶SUNY, Upton NY, ⁷EERC, University of North Dakota, Grand Forks ND, ⁸University of Utah, Salt Lake City UT, ⁹Ford Motor Company, Dearborn MI

Introduction

Diesel soot is believed to be a major constituent of airborne particulate matter and held partially responsible for global climate change and adverse health effects in humans. Here we give an overview of our efforts to characterize soot with synchrotron radiation techniques. Structural analysis on soot is usually performed with electron microscopy, but we are able to resolve all structural characteristics with X-ray scattering. Wide angle X-ray scattering (WAXS) confirms that soot is a quasi-graphitic material, and allows to determine sizes of graphitic domains or aliphatic side chains. Small-angle X-ray scattering (SAXS) permits to measure primary particle size, sizes of substructures, aggregate and agglomerate sizes, and fractal dimensions. Near-edge X-ray absorption fine structure (NEXAFS) spectroscopy reveals that major part of the soot is of a graphitic nature, but, unlike EELS, also permits the molecular speciation of surface functional groups and volatiles in soot. With the highly intense beam of a STXM microscope we were able to induce photochemical reactions on soot extracts and could in-situ simulate and monitor the atmospheric discharge of soot constituents.

Experimental

Diesel soot was obtained from several independent sources, such as NIST standards 1650 and 2975, and exhaust from a Ford diesel engine car. Soot was also produced at the diesel test engine facility at the University of Utah, from three diesel fuels in a 2-stroke diesel test engine, operated under idle or under load conditions. Extraction of volatiles was carried out with sub-critical water. For the Ultra-small angle X-ray scattering experiments, the soot was evenly distributed on scotch tape, at a thickness of approximately 200 micron. Additionally, soot pellets of 0.5 mm thickness and 6 mm diameter were pressed at various pressures. To simulate soot under no pressure, soot powder was immersed in acetone. SAXS was carried out at synchrotron beamline 12-ID of BESSRC-CAT, and USAXS was carried out at beamline 33-ID at UNICAT, both at Advanced Photon Source (APS), Argonne National Laboratory. The USAXS scattering curves were desmeared and background corrected. All USAXS data were fully corrected for all instrumental effects. Wide-angle X-ray scattering on soot powder before and after extraction of volatiles was carried out at beamline 18 A, National Synchrotron Light Source (NSLS), Brookhaven National Laboratory. The X-ray energy was 10,000 eV for USAXS and WAXS. NEXAFS experiments on soot powder, pellets, and dried extracts on goldfoil were performed at beamline 9.3.2 at the Advanced Light Source (ALS) in Berkeley National Laboratory, but also with the scanning transmission X-ray microscope at beamline X1-A at NSLS.

Results and Discussion

Ultra-small angle X-ray scattering (USAXS). A typical USAXS scattering curve of diesel soot is shown in Figure 1 (upper curve). We are able to identify five size ranges characteristic for diesel soot, and we can determine the fractal dimension of several structures [1]. Size range b) is the most prominent one and can be attributed to the fractal aggregates of primary particles. The aggregate sizes were typically 20 to 30 nm. When we used oxygenated diesel fuel, soot from idle engine had aggregates up to 85 nm, however. Simple Guinier analysis was sufficient to analyze this range. For $q=0.0015$, we find another weak structure which we assign to agglomerates of soot aggregates with sizes around 400 nm. The primary particles can only be found after subtraction of a Porod power law. The result is shown by the lower of the two scattering curves in Figure 1. Range c) indicates the Guinier fit for the primary particles, with sizes around 12 nm. Recent transmission electron microscopy images suggested the existence of substructures in soot primary particles. We have identified these in ranges d) and e) with sizes of 1.5 nm and below.

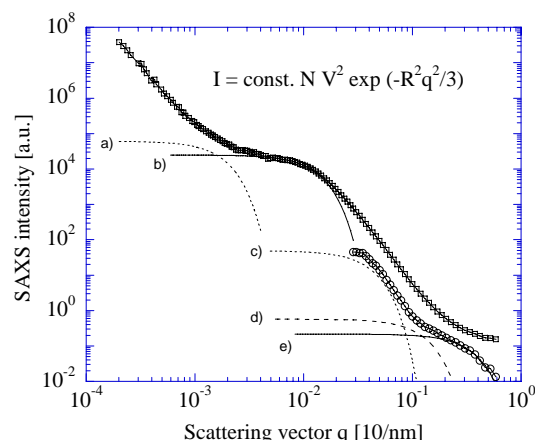


Figure 1. USAXS curve and Guinier fits after equation.

Depending on the applied pellet pressure, we are able to compress the aggregates [2], which can be seen by a remarkable shift of structure b) towards larger q values. We found that idle soot is less “stiff” than load soot. At maximum pressure, the aggregate structure is not maintained anymore, but the Guinier structure for the primary particles is clearly visible. Immersing soot in acetone permits to determine the aggregate size in its unaltered state, as shown by the according Guinier range in a minimal q position.

Wide-angle X-ray scattering (WAXS). We have studied both soot as received, and soot after extraction of volatiles, with WAXS. The WAXS curves of soot follow close the structure of graphite, but with more diffuse diffraction peaks. Figure 2 displays the (002) Bragg reflection of 3 soot samples from a test engine operated at various speeds. Similar to coal samples, the (002) reflection peak shows an aliphatic side band at its lower angle. The extent of this shoulder depended on the engine conditions and nature of fuel. Soot from fuel with diethyl carbonate as oxydant had a pronounced side band at middle engine speed (1800 rpm vs. 1500 and 2200), while regular fuel had this pronounced shoulder at the lowest engine speed (1500).

Extraction of the volatiles causes a partial decrease of the intensity of the side band for both regular and oxygenated fuel. Deconvolution of the side band and (002) reflection allows quantification of this effect. Figure 3 shows the decrease of the full width at half maximum (FWHM) of soot from both regular fuel and oxygenated fuel. The trend is the same for both, but soot from regular fuel has an overall sharper (002) reflection than from oxygenated fuel.

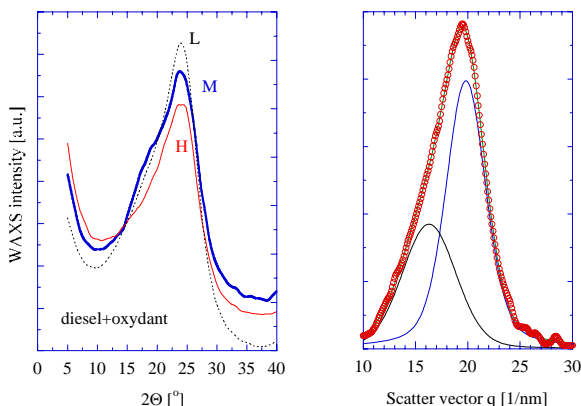


Figure 2. Left: WAXS curves of soot from diesel fuel mixed with oxidants. L, M, and H refer to 1500, 1800, and 2200 rpm. Right: Deconvolution into side band and (002) reflection.

The area under the aliphatic side band accounts to about 35% to the overall area under the side band plus (002) Bragg reflection. While extraction was performed at temperatures ranging from 25°C to 300°C, no significant change in the relative portions of these areas could be made out. For 25°C it was 36.8 %, and for 300°C it was 33.7 %. The impact of extraction on the WAXS scattering curves is easier to visualize in terms of peak widths. Figure 3 shows the full width at half maximum of the (002) reflection for the (002) reflection of soot from DEC mixed fuel and reference fuel.

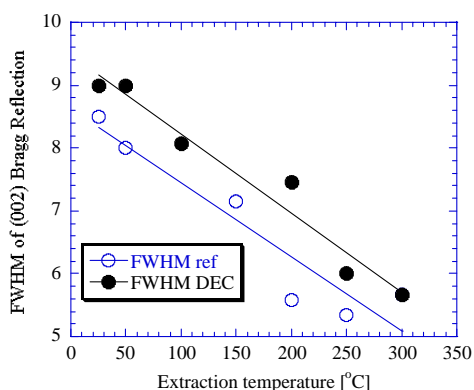


Figure 3. FWHM of the (002) reflection after deconvolution from the aliphatic side band for several different extraction temperatures.

These data permit also determination of crystallite sizes and degree of aromaticity.

Near-edge X-ray absorption fine structure (NEXAFS). Soot extracts, residuals and soot pellets were studied with NEXAFS [3,4]. Similar to graphite, soot spectra show a strong resonance of C=C bonds at 285 eV. Extraction of volatiles enhances the ratio between C=C peak intensity and peaks at energies between 286 eV and 289 eV, which result from aliphatics, C-H bonds, carbonyl and carboxyl groups, for instance. Unlike EELS with TEM [3], NEXAFS permits a detailed study of surface functional groups. Our extraction experiments are intended to facilitate deconvolution of soot spectra.

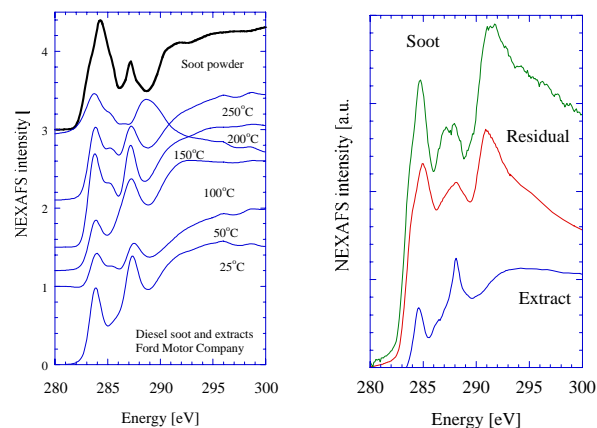


Figure 4. Left: NEXAFS spectra of soot as prepared, one extract, and the corresponding residual. Right: Sequence of NEXAFS spectra from soot and extracts for various extraction temperatures.

The left image in figure 4 shows a sequence of soot extract spectra as well as the original soot. Peak positions in spectra of extracts are all similar, but the peak height ratios are different. It is evident that soot is a very complex material.

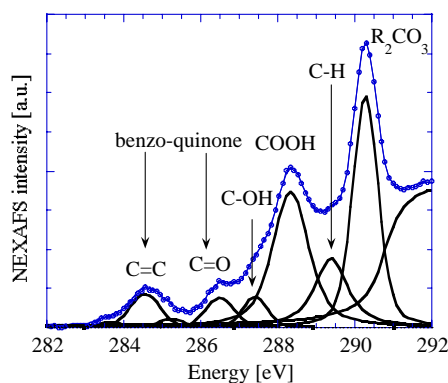


Figure 5. Peak assignment of a diesel soot extract.

The right image in figure 4 shows how the NEXAFS spectra of an extract and a residual qualitatively match up to the spectrum of the original solid soot material.

Not shown here, the intense X-ray beam of a STXM microscope caused remarkable changes in NEXAFS spectra of soot extracts,

revealing that these are prone to photochemical reactions. For instance, carboxyl groups decomposed into an organo carbonate, and possibly water. A proposed peak assignment of a NEXAFS spectrum of a soot extract is shown in figure 5. The peak at 290.5 eV was created during irradiation, on the cost of the intensity of the carbocyl group resonance at 288.5 eV.

Conclusions

Synchrotrons provide valuable tools for the structural characterization and molecular speciation of soot and soot extracts. Structural parameter like size, fractal dimension can be obtained with USAXS. WAXS is used to study crystallite sizes and aromaticity. NEXAFS was used for molecular speciation. We point out that these techniques are relatively straightforward and can be done in a high-throughput mode. Unlike microscopy techniques, the scattering results come with a robust statistical significance.

Financial support by the National Science Foundation, grant # CHE-0089133 is gratefully acknowledged.

References

- (1) Braun, A.; Huggins, F.E.; Seifert, S.; Ilavsky, J.; Shah, N.; Kelly, K.E.; Sarofim, A.; Huffman, G.P. *Combustion and Flame*, **2004**, 137 (1/2), 63-72.
- (2) Braun, A.; Ilavsky, J.; Jemian, P.R. *Deformation of diesel soot aggregates studied with ultra small angle X-ray scattering as a function of pellet pressure. Submitted to J.Appl.Phys.*
- (3) Braun, A.; Huggins, F.E.; Seifert, S.; Ilavsky, J.; Shah, N.; Kelly, K.E.; Sarofim, A.; Huffman, G.P. *Combustion and Flame*, **2004**, 137 (1/2), 63-72.
- (4) Braun, A.; Wirick, S.; Jacobsen, C.; Huggins, F.E.; Mun, S.B.; Shah, N.; Chen, Y.; Huffman, G.P. *Carbon*, **2005**, 43 (1), 117-124.

MAGNETIC IMAGING OF PYROLYSIS FEEDSTOCKS TO MODEL OLEFIN PRODUCT YIELDS

P.S. Virk

Department of Chemical Engineering
M.I.T., Cambridge, MA 02139

Abstract

A system for the Magnetic Imaging of Pyrolysis Feedstocks, acronym MIPF (pronounced with P silent) has been devised comprising three facets. First, sample preparation incorporates internal standards into the feedstock oils, to enable precise analysis of the NMR experiments. Second, NMR experiments are performed to provide quantitative C13 and H1 spectra, with spectral features elaborated by 1-D and 2-D procedures such as DEPT, COSY and HETCOR. Third, data analysis employs (1) an Integral Regions train, which provides coarse but complete information about all the carbon and hydrogen atoms in a feedstock, particularly the aromatic C and H atoms, and (2) a Canonical Groups train, which provides high-level information about chemical moieties, but detects only ~1/3 of all the atoms in the feedstock, particularly those in n- and methyl-alkane chains. An example illustrates how the MIPF parameters of an AGO feedstock might presage its performance in an ethylene plant.

Introduction

The present work derives from the need to engineer and predict the performance of modern pyrolysis coils that must crack diverse feedstocks at ever increasing temperatures, reaction severities and product selectivities. NMR imaging adds a unique dimension to olefin feedstock characterization because of its intimate relation to molecular topology and carbon atom hybridization. The most valuable olefins, ethylene, propylene, and butadiene, arise from operation of the free radical pathways prevalent during pyrolysis upon specific chemical moieties contained within the feedstock, respectively, normal-alkane chains, n-alkyl chain termini and methyl-alkyl units, and interior methylene chains. Individual sp³-hybridized carbon atoms within each of these moieties can be detected by NMR, to anticipate the corresponding olefin yields available from pyrolysis.

Of the voluminous literature on NMR applied to hydrocarbon mixtures, the present work has most been influenced by the classic papers of Knight (1967), Shoolery and Budde (1976) and Deutsche, Jancke and Zeigan (1976), specific articles by Ladner and Snape ((1978), Gillet et al (1981), Netzel et al (1981), and especially Cookson and Smith (1985, 1987), and the texts by Stothers (1972), Breitmaier and Voelter (1987) and Croasmun and Carlson (1994). In an earlier work (Virk 1999), akin to the present, NMR was applied to enhance conventional and mass spectrometric characterizations of FCC feedstocks.

MIPF System

Samples are prepared with gravimetric incorporation of internal standards into the feedstock oils, here AGOs and HCRs, to enable precise analysis and interpretation of the NMR experiments. Three internal standards are used, namely, deuteriochloroform CDCl₃, as oil solvent and spectrometer lock; dioxane, C₄H₈O₂, abbr DIOX, to assist in spectral integrations; and tetramethylsilane, Si(CH₃)₄, abbr TMS, as a spectral frequency reference. The primary NMR experiments performed provide quantitative C13 and H1 spectra, the spectral regions and individual resonances observed therein being identified and interpreted by additional 1-D and 2-D procedures that include DEPT, COSY, and HETCOR. Spectral data are analysed in two trains, according to either their integral regions, abbr IR, or their

canonical groups, abbr CG. In the IR train, the observed spectra are parsed into more or less coarse regions, each comprising chemically similar sorts of atoms. The IR train accounts for 100% of feedstock atoms and provides useful overall parameters, such as the percent of feedstock atoms, either carbon or hydrogen, that are aromatic, as well as more detailed regional data, and thence hydrogen atom counts, and thermochemical information. In the CG train, certain groups of spectral peaks that arise from atoms belonging to particular molecular moieties are recognized, particularly those in linear n-alkane chains and in 2-, 3-, 4-, 5-, and interior-methyl alkane branched chains. The CG train thus provides high-level quantitative information about n-alkane content and chain length, as well as the contents of a variety of methyl-alkane moieties; however the sum of identified species is but a fraction of the total, typically amounting to ~ 40% of feedstock atoms. Both IR and CG trains are combined to form a set of NMR groups that characterize the feedstock.

NMR Experiments

13-C. Figure 1 shows the 13-C NMR spectrum of an AGO feedstock called A1 in Table 1 (infra). The position of a peak on the x-axis, its resonance frequency or chemical shift, c, in units of ppm relative to TMS, is indicative of C atom type, while peak height on the y-axis, its absorption intensity, i, with arbitrary units, is roughly proportional to the abundance of such C atoms in the sample. Precise carbon atom amounts are obtained from peak integration, these integrals being the five continuously increasing stepped segments in the figure, their c-domains and magnitudes being noted below the abscissa.

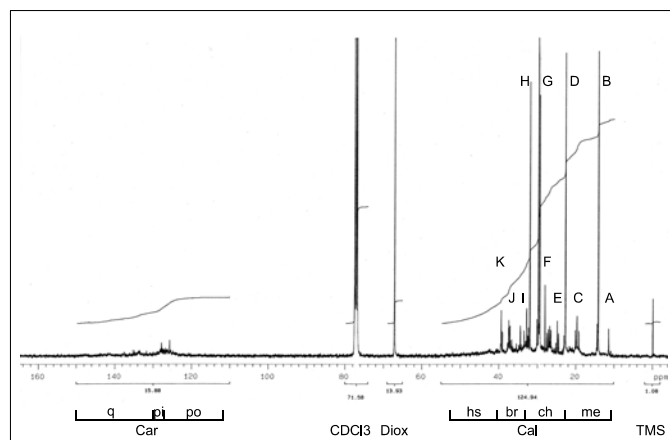


Figure 1. Annotated 13-C spectrum of an AGO feedstock.

The major spectral regions observed are:

Region	c (range)	C-atom type
TMS	0.0	methyl carbons in TMS
Cal	10 - 52	aliphatic carbons, sp ³ hybridized
DIOX	~67	methylene carbons in DIOX
CDCl ₃	~78 triad	C in CDCl ₃ solvent
Car	112 - 150	aromatic carbons, sp ² hybridized

The wide separation between the regions of aliphatic and of aromatic carbons is noteworthy, allowing unambiguous delineation of these two broad categories; the integrals corresponding to these regions provide the carbon aromaticity Car = 11.5%. Further demarcations shown below the spectrum, called Cumulative Integral Regions, sort carbon atoms into categories with the following approximate chemical interpretations: Carqt is aromatic quaternary, which are inherently of two kinds, either fused ring junction or substituted, not distinguished here; Carpi and Carpo are both

aromatic protonated, with subtle distinctions between them; the sum $\text{Car}(\text{qt}+\text{pi}+\text{po}) = \text{Car}$.

Among aliphatic carbons, Calhs is aliphatic highly substituted, Calbr is aliphatic branched (single substitution, such as methyl), Calch is aliphatic chains, mainly CH₂, and Calme is aliphatic methyls, all CH₃. Many additional individual spectral regions can be distinguished in Figure 1, and these have been labelled beside their principal peaks as follows: Regions B, D, H, and G (two tall peaks at $c \sim 30$) respectively contain the carbon atoms C1, C2, C3, and (C4, C ≥ 5) in linear n-alkane chains. Region C contains mainly methyl groups, pendant on a variety of alkane, cyclo-alkane and aromatic structures. Regions E and F contain carbon atoms in C5- and C6-cyclo-alkane rings, as well as C2 in 2-methyl-alkanes. Regions A, I, J and K contain carbon atoms from branched (iso-) alkanes. Peaks of the n-alkane moiety in regions B, D, H, and G, called a Canonical Group, reveal the present AGO to possess an n-alkane chain content of 24.9 C atoms per 100 C atoms of feedstock, with an average chain length $L = 6.9$, that is, for every pair of terminal n-alkane atoms (C1, C2), there are 4.9 interior n-alkane atoms (C3, C4, C ≥ 5).

1-H. Figure 2 shows the 1-H NMR spectrum of AGO feedstock A1. The x-axis is resonance frequency, or chemical shift, h , in units of ppm relative to TMS, indicative of hydrogen type, while the y-axis is absorption intensity, i , with arbitrary units, approximately proportional to the abundance of such hydrogen atoms in the sample. Accurate hydrogen amounts are obtained from integrals of peak intensities, seen as four continuous stepped lines in the figure, their h-domains and numerical magnitudes noted below the abscissa.

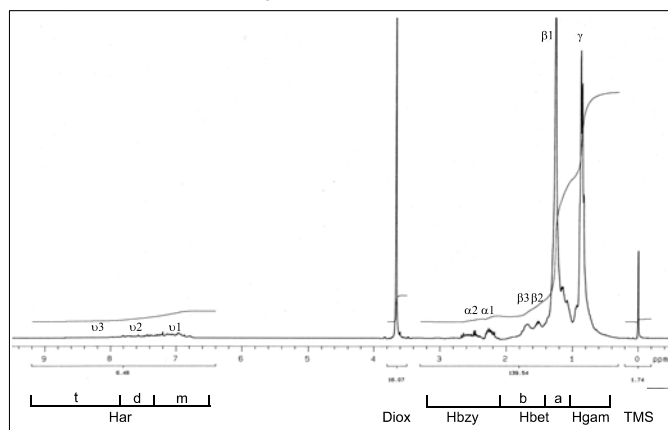


Figure 2. Annotated 1-H spectrum of an AGO feedstock.

The 1-H spectrum has the following regions:

Region	h (range)	H-atom type
TMS	0.0	H in methyls of TMS
Hgam, Hbet, Hbzy	0.4 - 3.2	Aliphatic H, attached to sp ³ hybridized C atoms
DIOX	~ 3.65	H in methylenes of DIOX
Har	6.5 - 9.2	aromatic H, attached to sp ² hybridized ring C atoms

The wide separation between the regions of aliphatic and of aromatic hydrogens is noteworthy, permitting their unambiguous delineation, and providing the hydrogen aromaticity $\text{Har} = 4.4\%$. The Cumulative Integral Regions, shown below the spectrum, have the following approximate chemical interpretations. The aromatic H region is subdivided into Hart, Hard, and Harm, with sum $\text{Har}(\text{t}+\text{d}+\text{m}) = \text{Har}$; of these, Harm contains H atoms from all aromatic rings; Hard contains H atoms from ≥ 2 - but not from 1-ring aromatics; and Hart contains H atoms from ≥ 3 - but not from ≤ 2 -ring

aromatics. Next, Hbzy are benzylic H atoms, attached to aliphatic C atoms bonded to aromatic rings; Hbzy thus reflects the degree of aromatic ring substitution. Of the two broad benzylic peaks in the spectrum, $\alpha 1$ is mainly H atoms on methyls pendant on mono-aromatic rings, while $\alpha 2$ contains a host of other benzylic hydrogens. Hbet are H atoms attached to aliphatic C atoms bonded to other aliphatic C atoms; region Hbeta, with huge peak $\beta 1$, is primarily H atoms in the methylene CH₂ units of alkyl chains, while Hbetb includes H atoms on CH (methine) and CH₂ (methylene), the peaks $\beta 2$, $\beta 3$ including H atoms on alicyclic rings. Hgam, with large twin peaks γ , are H atoms in aliphatic methyls CH₃.

2-D HETCOR. Figure 3 is a 2-dimensional contour plot showing the islands in an H-C atom correlation spectrum of AGO feedstock A1.

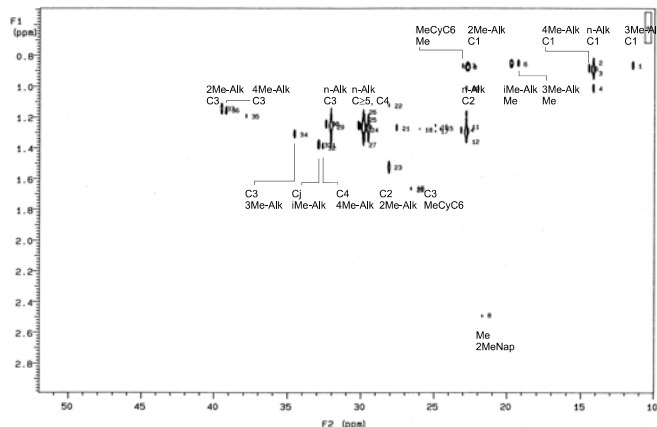


Figure 3. Annotated HETCOR spectrum of an AGO feedstock.

The HETCOR experiment, described by Gray (1994), is the equivalent of recording full 1-H spectra, such as shown in Figure 2, at each of a myriad slices of a 13-C spectrum, such as shown in Figure 1. A correlation island at chemical shift coordinates $[c, h]$ represents a carbon of shift c connected to a hydrogen of shift h , with island cross-section (actually, its peak height and volume) crudely related to the abundance of the correlated atoms in the feedstock. In Figure 3, with abscissa (F2 axis) c and ordinate (F1 axis) h , the large lens-shaped island #3 at coordinates $[c, h] = [14.2, 0.89]$ arises from the H and C atoms in the terminal methyl group of an n-alkane chain and is labeled n-Alk C1. This particular island has peak height $p = 232$ units on a scale where the spectral noise level is $p \sim 1$; the 37 islands visible on the figure have peak heights $283 > p > 4$, with all signals well above noise. Islands that have been chemically identified are labelled in four rows, top to bottom, representing methyl CH₃, methylene CH₂, methine CH, and benzylic methyl CH₃ carbons. Identified islands belong to the following Canonical Groups: n-alkane (C1, C2, C3, C4, C ≥ 5), 2-methyl alkane (C1, C2, C3), 3-methyl alkane (C1, Me, C3), 4-methyl alkane (C1, C3, C4), interior-methyl alkane (Me, Cj(unction)), methyl-cycloalkane (Me, C3(ring)), and 2-methyl naphthalene (Me).

Results

Both conventional and MIPF characterizations were acquired for six pyrolysis feedstocks, three AGOs and three HCRs, with results for two AGOs A1 and A2 and an HCR R1 shown in Table 1.

Table 1. Conventional and MIPF Characterizations.

Entry		A1	A2	R1		
CONVENTIONAL DATA						
SG	15.6C	0.838	0.843			0.835
H	Wt%	13.55	13.27			14.82
C	Wt%	86.34	86.51			85.18
S	Wt%	0.12	0.20			0.00
Helem	H/100 C	187	183			207
MIPF DATA						
IR Train C13						
diox/oil	Gravim	0.102	0.096	±	0.001	0.096
diox/oil	Spectral	0.099	0.106	±	0.005	0.094
Car	C/100 C	11.5	15.2	±	0.3	0.0
CIRs						
Calme		17.1	18.9	±	0.6	12.8
Calch		44.3	44.6	±	0.6	67.0
Calbr		18.5	16.5	±	0.3	16.8
Calhs		8.7	4.8	±	0.7	3.4
Cargo		4.6	4.4	±	0.7	0.0
Carpi		2.0	3.0	±	0.0	0.0
Carqt		4.9	7.8	±	0.5	0.0
Sum		100.0	100.0			100.0
IR Train H1						
diox/oil	gravimetric	0.109	0.105	±	0.001	0.093
diox/oil	Spectral	0.112	0.106	±	0.006	0.090
Har	H/100 H	4.4	5.6	±	0.3	0.1
CIRs						
Hgam		35.4	33.7	±	1.2	21.9
Hbeta		50.7	47.5	±	0.4	70.8
Hbetb		7.0	8.6	±	1.3	6.7
Hbzy		2.5	4.7	±	0.6	0.5
Harm		2.5	3.2	±	0.0	0.1
Hard		1.4	1.7	±	0.1	0.0
Hart		0.5	0.7	±	0.1	0.0
Sum		100.0	100.0			100.0
CG Train C13						
Lna	Atoms	6.9	5.9	±	0.0	9.7
Groups	C/100 C					
Can	n-Alkane	24.9	21.8	±	1.5	50.3
Cma	Me-Alkane	12.3	13.6	±	0.7	14.6
Ccs	Cyc+Sub	51.3	49.5	±	2.5	35.1
Car	Aromatic	11.5	15.2	±	0.3	0.0
Sum		100.0	100.0			100.0

Conventional properties included specific gravity and elemental assays of H, C, and S, from which H elem, H atoms/100 C atoms, has been calculated.

MIPF data include results from the IR and CG trains; for samples run in duplicate, average values and an estimate of their experimental uncertainty are quoted. Among IR train C13 data, the two rows labelled diox/oil are the ratios of carbon atoms in the dioxane internal standard to those in the oil; the gravimetric row was

calculated from sample preparation and elemental assays while the spectral row was independently derived from the regional integrals of the experimental spectra. Agreement between these internal standard ratios is a stringent test of C13 NMR data fidelity. The next row, Car, and then the next seven rows, called CIRs for Cumulative Integral Regions, provide a breakdown of feedstock carbon atom types, as percentages. CIRs are so named because each is the accumulation of Detailed Integral Regions, DIRs, which represent the finest parsing of spectral integrals; CIRs were earlier delineated in Figure 1 and their chemical significance pointed out. Data from the IR train H1 are analogous to those from the IR train C13, with two diox/oil rows, gravimetric and spectral, followed by Har and then seven CIRs, that were earlier considered in the 1-H NMR spectrum in Figure 2. Finally, the first row of the CG Train C13 data provides the average chain length of n-alkane moieties in the feedstock, Lna in C atoms. The second and third rows respectively provide the percentages of C atoms in n-alkane moieties Cna, and in methyl-alkane moieties Cma, the latter comprising 2-, 3-, 4-, 5-, and interior-methyl substituted alkane moieties. These are used, along with Car from the IR train, shown again in the fifth row, to form a set of 4 NMR-derived Canonical Groups for each feedstock. In the fourth row, the group Ccs, comprising cyclic and highly substituted aliphatic C atoms, is a remnant (often large) obtained from Ccs = 100 - Cna - Cma - Car.

Dioxane/Oil Ratios. Ratios of dioxane to oil D/O,g from the gravimetric sample preparation procedure to those derived from spectral integration D/O,s for each of the C13 and H1 spectra recorded provided the average relation:

$$(E1) \quad D/O,s = (1.00 \pm 0.06) D/O,g.$$

The present NMR integrals are thus accurate to within 6% absolute. Such noteworthy quantitative fidelity shows that modern NMR spectrometers can excite and detect diverse kinds of C and H atoms in the feedstock over wide frequency ranges on both sides of the C and H atoms in the dioxane internal standard.

MIPF Maps and Carbon Atom Groups. The NMR data in Table 1 provide three types of maps and two sets of carbon atom groups to characterize feedstocks in regard to their pyrolysis performance. These are, respectively, an aromaticity map, Car vs Har, a chain map, Cna vs Lna, and a branch map, Cna vs. Cma, as well as the sets of CIR and CG groups. For the present examples, the aromaticity map shows that while AGOs A1 and A2 differ appreciably in absolute terms, they possess similar ratios of Har/Car ≈ 0.37 , implying similarity in their respective fractions of protonated, substituted, and ring junction aromatic carbons. The chain map reveals n-alkane chain contents and lengths to vary such that R1 \gg A1 $>$ A2 while the branch map provides ratios of methyl-alkanes/n-alkane in the order R1 \ll A1 $<$ A2; both maps suggest that in producing ethylene, R1 should prove superior to both A1 and A2, and among the latter, A1 might be a bit better than A2.

MIPF-derived carbon atom groups for feedstocks A1 and R1 are depicted as pie charts in Figure 4. For each feedstock, the IR train pie has six slices [Calme, Calch, Calbr, Calhs, Carpr, Carqt], respectively denoting percentages of aliphatic methyl, chain, branch, highly-substituted carbons and aromatic protonated and quaternary carbons, while the CG train pie has four slices [Cna, Cma, Ccs, Car], respectively the percentages of n-alkane, methyl-alkane, alicyclic + highly substituted, and aromatic carbon atoms in the feedstock. The IR pie offers a complete but coarse sorting of the types of carbon atoms in a feedstock whereas the CG train offers refined information about carbons contained in n- and methyl alkane moieties but leaves a significant fraction of them, from 1/3 to 1/2, unassigned, in the remnant Ccs. A comparison between feedstocks A1 and R1 shows their respective IR and CG group pies to differ significantly, with R1

containing far more n-alkanes and virtually no aromaticity; on this basis, R1 should prove superior to A1 in producing more olefins and less pyrolysis fuel oil.

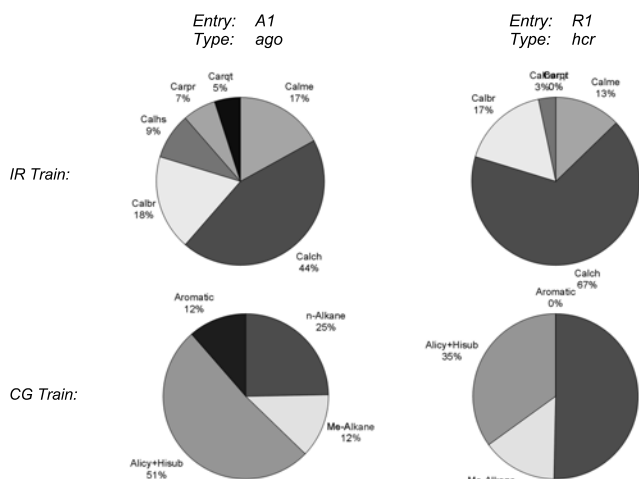


Figure 4. MIPF-derived carbon atom groups in two feedstocks.

Relation of MIPF to Pyrolysis Performance

Some examples are presented to illustrate how MIPF parameters might relate to pyrolysis product yields. Our slate of feedstocks, as well as three pure n-alkanes, namely decane, dodecane and hexadecane, were cracked using steam/hydrocarbon ratios ~ 1 and “kinetic severities” $K^* \sim 2$, as defined by Zdonik, Green and Hallee (1969). Reaction conditions and experimental apparatus were akin to those in an earlier work concerning pyrolysis of virgin and hydrogenated gas oils (Virk, Korosi and Woebcke 1979b).

Three fractions define overall pyrolysis yields, namely, in descending order of desirability, GAS, C4 and lighter; raw pyrolysis gasoline RPG, C5 to 400 F; and pyrolysis fuel oil PFO, >400 F. Figure 5, called a “yield fingerprint”, is a Cartesian plot of GAS yield, wt%, versus IR Region 1, comprising the sum of the first two CIRs (Calme + Calch), in C/100 C.

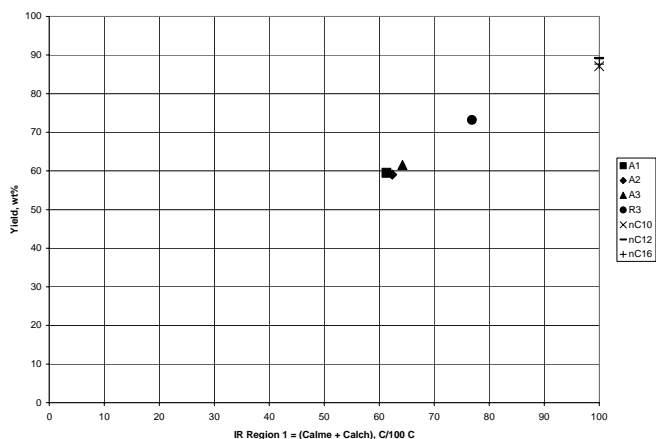


Figure 5. Yield fingerprint of GAS vs IR Region 1.

The GAS yields obtained from each feedstock are essentially equal to, perhaps a bit less than, the corresponding magnitudes of IR Region 1. Next, Figure 6 is a fingerprint of PFO yield, wt%, versus IR Region 3, which comprises the sum of CIRs 4 to 7, namely (Calhs + Car), in C/100 C.

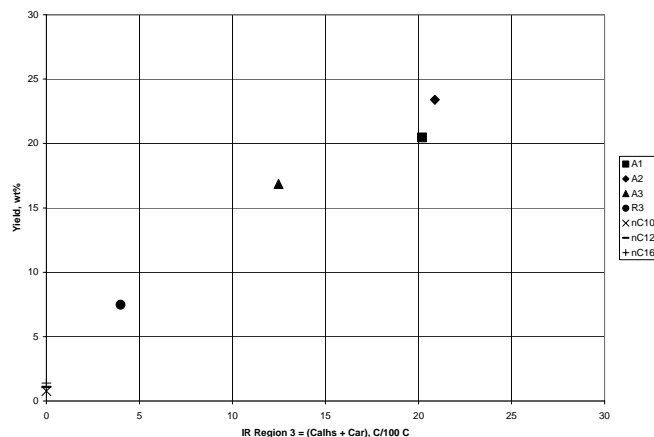


Figure 6. Yield fingerprint of PFO vs IR Region 3.

The PFO yields obtained from each feedstock are essentially equal to, perhaps a tad higher than, the corresponding magnitudes of IR Region 3. With $GAS \approx CIR(1+2)$ and $PFO \approx CIR(4+5+6+7)$, it follows from the requisite conservations that $RPG \approx CIR(3) = Calbr$, called IR Region 2. It is mildly astonishing that the NMR-derived IR regions, that are simply sums of adjacent CIRs, should relate so directly to the respective amounts of the three overall pyrolysis products. This connection, which has not hitherto been reported, should be fun to explore and exploit.

Turning to individual products, Figure 7 presents a fingerprint for the major olefin, ethylene, using CG Cna, n-alkane chain content.

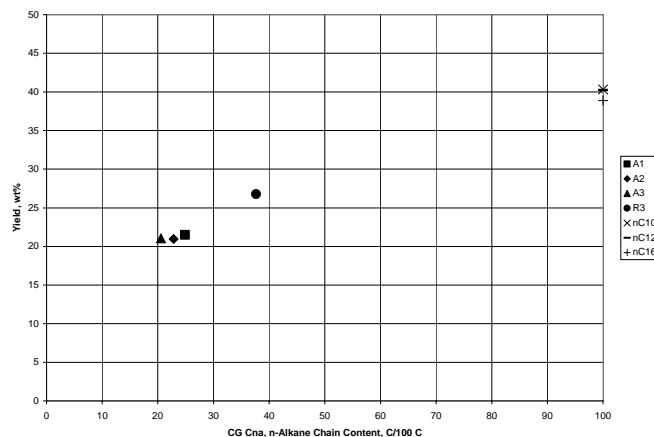


Figure 7. Yield fingerprint of Ethylene vs CG Cna, n-alkane chains.

Results from the pure n-alkanes, with $Cna = 100$, suggest that under the present pyrolysis conditions, n-alkane chains provide ethylene yield $\approx 0.4 \cdot Cna$. Ethylene yields observed from the feedstocks range from $(0.7 \text{ to } 1.0) \cdot Cna$, and must therefore additionally arise from moieties other than n-alkanes. Finally, Figure 8 shows the fingerprint for a minor product, buta-1,3-diene, using $CG\ Cna > 2$, n-alkane interior carbons, based on the notion of butadiene being a secondary product. The pure n-alkanes provide butadiene yield $\approx 0.1 \cdot Cna > 2$ while the AGO and HCR feedstocks have butadiene yields $\approx (0.2 \text{ to } 0.3) \cdot Cna > 2$, showing, as for ethylene, that butadiene must additionally arise from moieties other than n-alkane chain interiors.

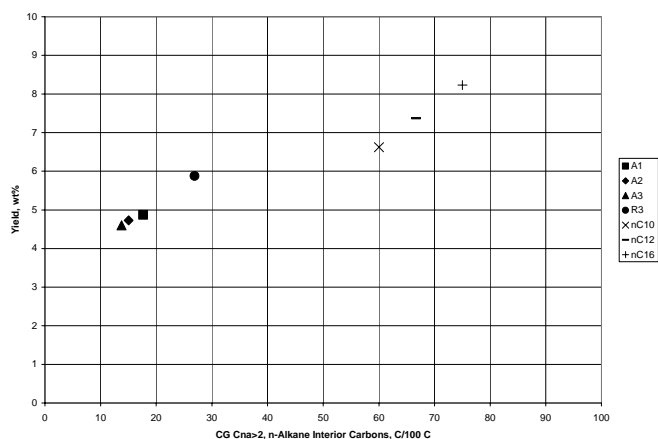


Figure 8. Yield fingerprint of Butadiene vs CG Cna>2, n-alkane interior carbons.

It is interesting that both ethylene and butadiene are abundant products of cyclohexane pyrolysis (Virk, Korosi and Woebcke 1979a), so that alicyclic moieties in the feedstocks might well provide additional sources for the ethylene and butadiene yields observed in excess of those expected from n-alkane chains.

Conclusions.

1. A MIPF system has been devised for quantitative NMR-assays of AGOs and HCRs according to a coarse but quantitative IR Train and a fine but fractional CG Train.

2. Annotated 13-C, 1-H, and 2-D HETCOR spectra of an AGO feedstock were presented to illustrate the system.

3. MIPF results for three each AGO and HCR feedstocks included: Gravimetric vs spectral dioxane/oil ratios.
Carbon and Hydrogen aromaticities.
n-Alkane chain contents and chain lengths.
Characterization by IR and CG train carbon atom groups.

4. Overall and individual pyrolysis product yields at fixed cracking severity $K^* \sim 2$ were related to NMR-derived carbon atom groups as follows:
GAS (C4 and lighter) yields approximately equalled the unbranched, unsubstituted aliphatic carbons found from the IR train.
PFO (> 400F) yields roughly equalled the sum of (substituted + aromatic) carbons found from the IR train.
Ethylene yields varied with n-alkane chain content found from the CG train and butadiene yields varied with n-alkane internal carbons, also found from the CG train, but for both these products the observed yields exceeded those expected from n-alkane moieties alone.

Acknowledgements

This work was supported by Larry Hallee, late of Stone & Webster Engineering Corporation, Houston, TX. The author is indebted to Jeanne Owens, of the MIT Spectrometry Laboratory, Cambridge, MA, for help with NMR spectra.

References

- (1) Knight, S.A.: Chem. Ind., 1920-1923 (1967).
- (2) Shoolery, J.N.; Budde, W.L.: Anal. Chem., 48, 1458-1461 (1976).

- (3) Deutsch, K.; Jancke, H.; Zeigan, D.: J. Prakt. Chem. Ind., 318, 177-184 (1976).
- (4) Ladner, W.R.; Snape, C.E.: Fuel, 57, 658-662 (1978).
- (5) Gillet, S.; Rubini, P.; Delpuech, J.J.; Escalier, J.C.; Valentin, P.: Fuel, 60, 221-225 (1981).
- (6) Gillet, S.; Rubini, P.; Delpuech, J.J.; Escalier, J.C.; Valentin, P.: Fuel, 60, 226-230 (1981).
- (7) Netzel, D.A.; McKay, D.R.; Heppner, R.A.; Guffey, F.D.; Cooke, S.D.; Varie, D.L.; Linn, D.E.: Fuel, 60, 307-320 (1981).
- (8) Cookson, D.J.; Smith, B.E.: Anal. Chem., 57, 864-871 (1985).
- (9) Cookson, D.J.; Smith, B.E.: Energy & Fuels, 1, 111-120 (1987).
- (10) Stothers, J.B.: "Carbon-13 NMR Spectroscopy", Academic Press, New York, NY 1972.
- (11) Breitmaier, E.; Voelter W.: "Carbon-13 NMR Spectroscopy: High-Resolution Methods and Applications", 3rd Ed., VCH Publishers, Weinheim, Germany, 1987, pp73-105.
- (12) Croasmun, W.R.; Carlson, R.M.K.: "Two-Dimensional NMR Spectroscopy: Applications for Chemists and Biochemists", 2nd Ed., VCH Publishers, Weinheim, Germany, 1994.
- (13) Virk, P.S.: Prepr. Pap. - Am. Chem. Soc., Div. Fuel Chem., 44, (3), 546 (1999).
- (14) Gray, G.A., Ch 1, pp 46-49 in Croasmun, W.R.; Carlson, R.M.K.: "Two-Dimensional NMR Spectroscopy: Applications for Chemists and Biochemists", 2nd Ed., VCH Publishers, Weinheim, Germany (1994).
- (15) Zdonik, S.B.; Green, E.J.; Hallee, L.P: Oil Gas J., 66, (7) 192 (1969).
- (16) Virk, P.S.; Korosi, A.; Woebcke, H.N: ACS Advances in Chemistry Series 183, 67-76 (1979a).
- (17) Virk, P.S.; Korosi, A.; Woebcke, H.N: ACS Advances in Chemistry Series 183, 77-89 (1979b).

STUDIES OF CATALYSIS WITH SINGLE ATOM SENSITIVITY BY ABERRATION-CORRECTED STEM AND FIRST-PRINCIPLES THEORY

Stephen J. Pennycook^{1,2}, Andrew R. Lupini¹, Albina Borisevich¹, K. Sohlberg³, Alberto Franceschetti^{2,1}, Sergei Rashkeev^{1,2}, Steven H. Overbury¹ and Sokrates T. Pantelides^{2,1},

¹Oak Ridge National Laboratory, Oak Ridge, TN 37831

²Department of Physics and Astronomy, Vanderbilt University, Nashville, TN 37235

³Department Of Chemistry, Drexel University, 3141 Chestnut Street, Philadelphia, PA 19104

Introduction

The successful development of aberration correctors for the scanning transmission electron microscope (STEM) has more than doubled the achievable spatial resolution in the last few years, and the direct imaging of a crystal lattice at sub-Angstrom resolution has recently been demonstrated.¹ The sub-Angstrom probe has the same current as the uncorrected probe, but it is concentrated into a much smaller diameter with much greater peak intensity. It therefore allows the imaging of single atoms on real catalyst supports with much greater resolution and signal to noise ratio than before, making the aberration-corrected STEM an ideal instrument for correlating atomic structure of catalysts to chemical reactivity. Here we present several examples of the capabilities realized by such instruments, carried out using the VG Microscopes HB603U STEM at Oak Ridge National Laboratory (ORNL), equipped with a Nion aberration corrector. This machine operates at an accelerating voltage of 300 kV and produces a beam size of 0.6 Angstroms.¹

Experimental Results

Pt trimers on γ -Al₂O₃. The first images to show that Pt clusters could form trimer-like structures on the surface of a high surface area γ -Al₂O₃ were obtained several years ago by uncorrected STEM.² That work showed that extremely small clusters, even single atoms, might be catalytically important, but the precision of the experimental data on the interatomic distances was insufficient to choose among the competing mechanisms of trimer formation. The improved sensitivity after aberration correction is striking, as shown in **Figure 1**. These images demonstrated that the Pt-Pt distances in the trimer differ significantly from those in bulk Pt. A thorough theoretical study has shown that the experimentally observed geometry can only be achieved in an adatom cluster capped by an OH- group.³ Additionally it was demonstrated that unlike the metastable Pt₃ cluster, the Pt₃OH formation was stable and had slightly electron-deficient character (Pt₃ was found to be slightly electron-rich). This finding relates directly to the Lewis acidity and catalytic activity of the Pt/ γ -Al₂O₃ catalysts.

Au nanoparticles on TiO₂. Au is not a good catalyst in bulk or in the form of large particles, but when prepared as nanoparticles on an oxide support, it becomes one of the most active catalysts for the oxidation of CO to CO₂. The cause of this activity has been a mystery for many years, with several explanations proposed. Early work showed that there is a correlation between particle size and activity,^{4,5} although it is difficult to see the smallest nanoparticles by conventional TEM, hindering the identification of likely sites and mechanisms. More recent work on model systems has shown that the thickness may be more important than the lateral extent, with bilayer structures having the highest activity.⁶

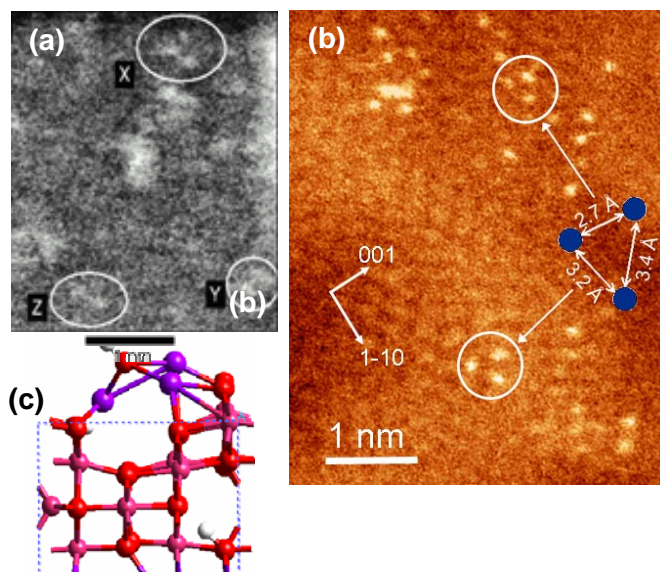


Figure 1. Z-contrast STEM image of Pt trimers and dimers on the surface of γ -Al₂O₃ before (a) and after (b) aberration correction. Two Pt₃ trimer structures are circled; inset - measured interatomic distances. A hint of the alumina lattice is also visible. (c) Schematic of the configuration for the Pt₃OH unit on the (110) surface of γ -Al₂O₃, determined by first-principles calculations, with closely matching interatomic distances.

We have used aberration corrected STEM to image the clusters of a Au catalyst prepared by deposition/precipitation onto nanocrystalline anatase. Following mild reduction in 12%-H₂ at 423 K, the catalyst showed 50% conversion at 235K as measured in a plug-flow reactor, with a reaction rate of about 3.5×10^{-3} moles CO/(mole Au s), which is comparable to the highest reported in the literature at this temperature. As seen in **Figure 2**, most of the nanoparticles are 1-2 nm diameter, and quantifying the thicknesses by comparing to image simulations revealed that they are just 1 or 2 layers thick. Furthermore, the contrast seen in the image is in fact that of the TiO₂ substrate showing right through the Au nanoparticles. Since we certainly have the resolution to resolve a Au crystal, and none were seen on this sample, it seems likely that the nanoparticles may be in a liquid state.

XANES studies were carried out on the catalysts to determine the Au oxidation state during catalysis. Results show that no more than a few percent of the Au could be oxidized in the most catalytically active state. Introducing reactants into the gas stream resulted in no detectable changes to the XANES data. Once reduced, the Au particles are not reoxidized by exposure to air at room temperature or even at 573 K, and so are unlikely to re-oxidize under reaction conditions or during transfer into the STEM.

Therefore we believe that the images shown in Figure 2 are representative of the active state of the Au nanocatalysts. Based on these images, it was then possible to perform first-principles calculations to investigate the adhesion energies of Au_N clusters on defect-free TiO₂ surfaces and also on the same surfaces with an O vacancy. Single Au atoms adsorb preferentially at O vacancy sites with a binding energy about 0.9 eV larger on the O vacancy than on the stoichiometric (001) surface. The binding energy of Au_N clusters at an O vacancy site is approximately constant with the number N of Au atoms, suggesting that only the Au atom on the O vacancy site forms a strong bond with the substrate. Further evidence for this

conclusion is provided by the observation of the relaxed cluster structure, which shows one Au atom displaced into the O vacancy site. We conclude that O vacancies act as "anchors" to suppress coalescence, consistent with earlier calculations.⁷ Such anchors facilitate the high areal density of small clusters.

Further calculations were carried out of the binding energies of CO and O₂ molecules. While a single Au atom binds CO and O₂ only weakly, larger Au clusters, such as Au₇ and Au₁₀, can adsorb *both* CO and O₂, unlike gold steps or surfaces. Thus it seems that the ability to bind both of the reactants is the key to the high activity of this unusual catalyst.

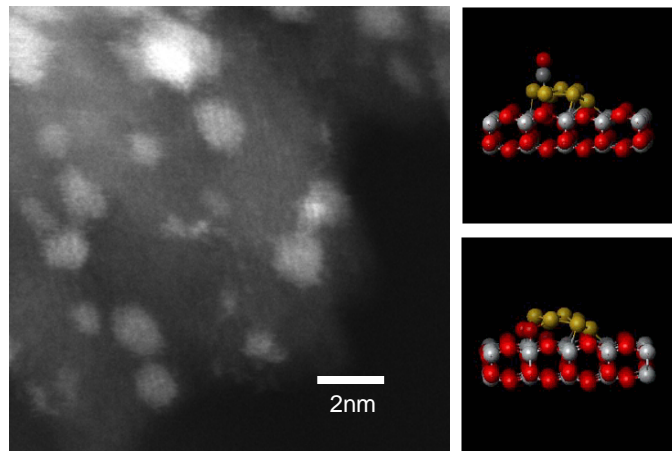


Figure 2. (Left) Z-contrast STEM image showing Au nanoparticles on a titania flake. Most of the nanoparticles are between 1 and 2 nm in diameter and are 1 to 2 layers thick. First-principles calculations for the nanoparticles observed shows that they are capable of bonding both CO (right top) and O₂ (right bottom), enabling the high catalytic activity.

La-stabilization of supports. γ -Al₂O₃ is used extensively as a catalytic support material because of its high porosity and large surface area but at temperatures in the range 1000-1200°C transforms rapidly into the thermodynamically stable α -Al₂O₃ phase (corundum), drastically reducing the surface area and suppressing the catalytic activity of the system. The phase transformation can be shifted to higher temperatures by doping with elements such as La but previously it was not possible to establish if dopants enter the bulk, adsorb on surfaces as single atoms or clusters, or form surface compounds.

A Z-contrast image of a flake of La-doped γ -Al₂O₃ in the [100] orientation is shown in **Figure 3**. The square arrangement of Al-O columns is clearly resolved. Single La atoms are visible in the form of brighter spots on the background of thicker but considerably lighter γ -Al₂O₃ support. Most of the La atoms are located directly over Al-O columns (site A), but a small fraction also occupies a position shifted from the Al-O column (site B). The images reveal clearly that there is no correlation in the distribution of dopant atoms, and a through focal series shows they are located on the surfaces of the flake. Density functional theory calculations have demonstrated that La atoms are very strongly bound to the γ -Al₂O₃ surfaces (binding energy 7-8 eV), considerably stronger than to the α -alumina surface (binding energy 4.3 eV). Thus it became apparent that the stabilization is achieved by single La atoms adsorbed on the γ -Al₂O₃ surface, which improve its stability with respect to phase transition and make sintering highly unfavorable.⁸

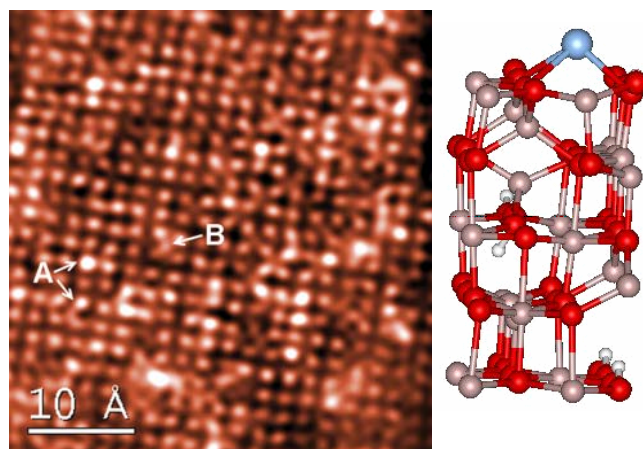


Figure 3. (left) Z-contrast image of La atoms on a γ -Al₂O₃ flake in [100] orientation. (Right) Schematic of the configuration for the La atom determined by first-principles calculations.

Discussion and future directions. The aberration-corrected STEM provides the sensitivity to image individual transition metal and rare earth atoms on light oxide supports, allowing new insights into many issues of catalysis. Developments are presently underway to provide an *in-situ* capability for reactive gases and elevated temperatures to provide conditions closer to those of the active catalyst. In addition, an unanticipated benefit of aberration correction is the greatly enhanced depth resolution, which allows three-dimensional images to be formed by the technique of depth slicing, maintaining single atom sensitivity. Presently the depth resolution is ~ 2 nm, but this should improve to ~ 1 nm in future generations of aberration-corrected STEM.

Acknowledgment. Research sponsored by the Office of Basic Energy Sciences, U.S. Department of Energy, under contract DE-AC05-00OR22725, by an appointment to the ORNL Postdoctoral Research Associates Program, and by the Laboratory Directed Research and Development Program of ORNL.

References

1. Nellist, P. D.; Chisholm, M. F.; Dellby, N.; Krivanek, O. L.; Murfitt, M. F.; Szilagy, Z. S.; Lupini, A. R.; Borisevich, A.; Sides, W. H.; Pennycook, S. J. *Science* **2004**, *305*, 1741-1741.
2. Nellist, P. D.; Pennycook, S. J. *Science* **1996**, *274*, 413-415.
3. Sohlberg, K.; Rashkeev, S. N.; Borisevich, A. Y.; Pennycook, S. J.; Pantelides, S. T. *ChemPhysChem* **2004**, *in press*.
4. Haruta, M. Size and support dependency in the catalysis of gold. In *Catalysis Today*, 1997; Vol. 36; pp. 153-166.
5. Valden, M.; Lai, X.; Goodman, D. W. Onset of catalytic activity of gold clusters on titania with the appearance of nonmetallic properties. In *Science*, 1998; Vol. 281; pp. 1647-1650.
6. Chen, M. S.; Goodman, D. W. *Science* **2004**, *306*, 252-255.
7. Rodriguez, J. A.; Liu, G.; Jirsak, T.; Hrbek, J.; Chang, Z. P.; Dvorak, J.; Maiti, A. Activation of gold on titania: Adsorption and reaction of SO₂ on Au/TiO₂(110). In *Journal of the American Chemical Society*, 2002; Vol. 124; pp. 5242-5250.
8. Wang, S. W.; Borisevich, A. Y.; Rashkeev, S. N.; Glazoff, M. V.; Sohlberg, K.; Pennycook, S. J.; Pantelides, S. T. *Nature Materials* **2004**, *3*, 143-146.

NEAR-FIELD SCANNING OPTICAL MICROSCOPY OF METAL NANOPARTICLES AND NANOSCALE HETEROSTRUCTURES

Gary P. Wiederrecht, Gregory A. Wurtz, Jasmina Hranisavljevic

Chemistry Division and Center for Nanoscale Materials, Argonne National Laboratory, Argonne, Illinois 60439

Introduction

The interaction of light with metal nanoparticles produces a range of physical and chemical phenomena that impact an extraordinary breadth of basic science research and technological applications related to fuel chemistry. Areas of interest include surface enhanced Raman scattering (SERS),¹⁻³ photocatalysis,⁴ and molecular sensors,⁵ to name only a few. These applications are frequently the result of the confined optical field, or evanescent field, that is produced when the surface plasmon resonance of metal nanoparticles is optically excited. An understanding of the spatial profile of the intensity of this field is critical for understanding the adsorbate/nanoparticle interactions, or what types of structures can optimize the strength, confinement, and plasmon resonance energy for a particular application. In this presentation, the application of near-field scanning optical microscopy (NSOM) towards imaging metal nanoparticles and functionalized nanoparticle heterostructures is described. Our emphasis is on the use of NSOM to understand the chemical and physical adsorbate interactions with the metal nanoparticles. A specific example is that of metal-organic nanometer-sized complexes formed by the J-aggregates from cyanine dyes adsorbed on silver (Ag) nanoparticles using NSOM. Comparing results obtained on both bare and J-aggregate coated particles we show that the near-field contrast is sensitive to optically induced charge transfer occurring between the particle and the J-aggregates.

Experimental

We used the procedure described by Kometani *et al.* to prepare the J-aggregate coated Ag nanoparticles.⁶ The dye used was a cyanine derivative, 5,5'-dichloro-3,3'-disulfopropylthiacyanine sodium salt (TC, Hayashibara Biochemical Laboratories, Japan). The ground state absorption spectrum of the Ag/J-aggregate complex in solution shows a slightly red shifted plasmon frequency to ca. 400 nm, and a new absorption band at ca. 475 nm representative of J-aggregation on the nanoparticle. A schematic of the dressed particle (DP) is shown in the inset of Fig. 1. Far-field transient absorption spectroscopy combined with fluorescence spectroscopy strongly suggest that a charge transfer from the J-aggregates to the particle is likely to occur subsequent to the particle plasmon excitation (pictured in the inset of Fig. 1), quenching the radiative relaxation pathway the J-aggregates show in solution.^{7,8}

The near-field optical (NFO) distribution was probed using a commercially available silicon tip (NCH-W, Nanosensors). An atomic force feedback loop (Multimode/IIIa, Digital Instruments) insured a constant probe to sample distance regulation in the intermittent contact mode. A microscope objective (0.28 NA, 33 mm working distance) collects the field diffracted by the probe-to-sample interaction at an angle of 75° from the probe axis in the backscattering direction with respect to the incident wave vector (see Fig. 1). The polarization of the resulting collimated beam is then analyzed and subsequently focused onto an optical fiber (0.2 NA, 100 µm core diameter) with a 3 cm focal length lens. The output of the fiber is incident on a photomultiplier tube (Hamamatsu H5773-01) via an interference filter centered at 400 nm and is lock-in demodulated to provide the NFO signal. Unless otherwise stated, the

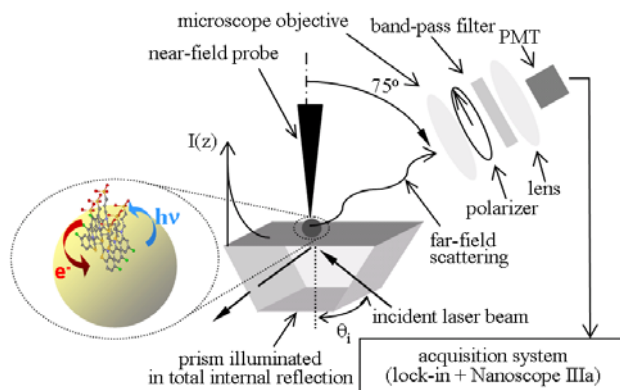


Figure 1. The basic operation of apertureless NSOM is shown. Scattering lobes radiated from the probe/sample interaction region are collected in the far-field by the detection optics. In some configurations, such as tapping mode, a lock-in can be used to demodulate the signal for better signal to noise.

images presented here are recorded at the probe vibration frequency f ($f \sim 330$ kHz) and for a probe vibration amplitude of ca. 50 nm.

Results and Discussion

The NFO response from the plasmon oscillation of a bare Ag nanoparticle is first investigated. For this purpose the Ag nanoparticle is illuminated with a transverse magnetic (TM) polarized field at a wavelength of 415.4 nm. Figure 2 presents the AFM (Fig. 2(a)) as well as the corresponding NFO image (Fig. 2(b)) for a 40 nm diameter particle. The NFO contrast corresponds to the component of the scattered field polarized parallel to the plane of incidence (see Fig. 1). Figure 2(b) features both strong spatial confinement and local enhancement that are characteristic for the particle resonant near-field response.

We found contrasting changes to both Fig. 2(b) and the far-field results obtained on the DP when characterizing the NFO response of the DP. Briefly, we will show that: (i) the evanescent field scattered by the bare Ag particle is absorbed by the J-aggregates; (ii) NFO images support strong evidence for the occurrence of charge transfer between the J-aggregates and the nanoparticle.

Figure 3(a) represents the AFM contrast for a 40 nm diameter DP and Figs. 3(b)-(d) are the corresponding NFO images obtained under different detection conditions. For conditions identical to Fig.

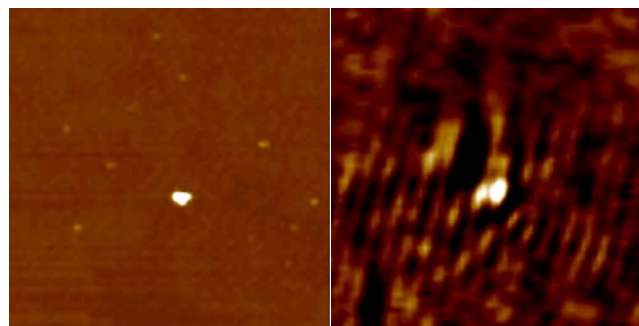


Figure 2. Ag nanoparticle illuminated in total internal reflection at 415.4 nm on a glass substrate. (a) and (b) correspond to the respective AFM and NFO contrasts of a 40 nm diameter Ag particle. The illumination polarization is TM and the NFO image represents the field polarized parallel to the plane of incidence. Scan sizes are 3.6 µm.

2(b), the NFO distribution for the DP loses the characteristic features of Fig. 2(b) as a much weaker and more complicated contrast is observed in Fig. 3(b). Although both Figs. 2(b) and 3(b) relate to highly absorbing objects, this absorption leads to an intense evanescent near-field scattering only for the bare particle (Fig. 2(b)). This observation is supported by the far-field transient spectroscopy experiments showing that the J-aggregates absorb the field scattered by the particle plasmon oscillation; internal damping provides the subsequent relaxation pathway for the energy absorbed by the DP.⁷

Recording the DP near-field response at the harmonics nf (n integer >1) of the probe vibration frequency f supports the occurrence of energy transfer between the Ag particle and its J-aggregate coating. Indeed, the DP shows very similar NFO contrasts up to $4f$; Fig. 3(c) obtained at $2f$ illustrates such a contrast. This image shows that a highly spatially confined field is present in the vicinity of the DP and the existence of similar contrasts for higher harmonics underlines this confinement. In fact, the appearance of non-linearities in the DP near-field modulation demonstrates the severe local nature of the interaction between the probe and the DP. This observation along with the far-field results showing a quenching of the fluorescence suggests that the DP is emitting light upon strong interaction with the probe, i.e. the vicinity of the probe opens a radiative relaxation channel for the DP. In Fig. 3(c), elastic scattering originating directly from the plasmon scattering and mediated by the

J-aggregate coating is taking place. However, the distinction of the two scattering mechanisms is difficult to rule out at this point.

To gain more insight on these results we collected the emission from the J-aggregates expected around 475 nm. For this purpose, the resonant excitation of the DP plasmon oscillation is preserved at 415.4 nm while a band-pass filter centered at 450 nm is inserted in the collection system to collect the emission of interest. Figure 3(d) represents the NFO contrast obtained under these conditions, where emission is observed only at the DP location. As opposed to spontaneous emission for which light is usually detected at some distance from the emitting object, the spatial confinement of the source in Fig. 3(c) supports the above-mentioned interpretation suggesting that the probe provides the radiative relaxation channel for the DP, leading to the emission of light by the J-aggregates.

Conclusion

The optical near-field properties of nanostructured complexes formed by J-aggregate coated Ag particles have been experimentally studied using NSOM. Our results show that the J-aggregates adsorbed on the Ag particle absorb the light scattered in near-field by the resonantly excited plasmon oscillation in the dressed particle. A new radiative relaxation channel opened by the presence of the probe near the dressed particle introduced high anharmonicity in the light modulated by the probe vibration. Hence, analyzing the near-field images at the harmonics of the probe vibration frequency enabled us to observe energy transfer occurring between the Ag core and J-aggregate coating in the dressed particle. Evidence of fluorescence from the J-aggregates further supports this observation.

Acknowledgments. This work was supported by the US Department of Energy, Office of Basic Energy Sciences, Division of Chemical Sciences under contract number W-31-109-ENG-38. This work also benefited from the University of Chicago-Argonne National Laboratory Consortium for Nanoscience Research.

References

- (1) Moskovits, M. *Reviews of Modern Physics* **1985**, 57, 783.
- (2) Schatz, G. *Acc. Chem. Res.* **1984**, 17, 370.
- (3) Campion, A.; Kambhampati, P. *Chem. Soc. Rev.* **1998**, 4, 241.
- (4) Dawson, A.; Kamat, P. V. *J. Phys. Chem. B* **2001**, 105, 960.
- (5) Park, S.; Yang, P.; Corredor, P.; Weaver, M. J. *J. Am. Chem. Soc.* **2002**, 124, 2428.
- (6) Kometani, N.; Tsubonishi, M.; Fujita, T.; Asami, K.; Yonezawa, Y., *Langmuir* **2001**, 17, 578.
- (7) Hranisavljevic, J.; Dimitrijevic, N.M.; Wurtz, G.A.; Wiederrecht, G.P. *J. Am. Chem. Soc.* **2002**, 124, 4536-4537.
- (8) Wiederrecht, G. P.; Wurtz, G. A.; Hranisavljevic, J. *Nano. Lett.* **2004**, ASAP article.

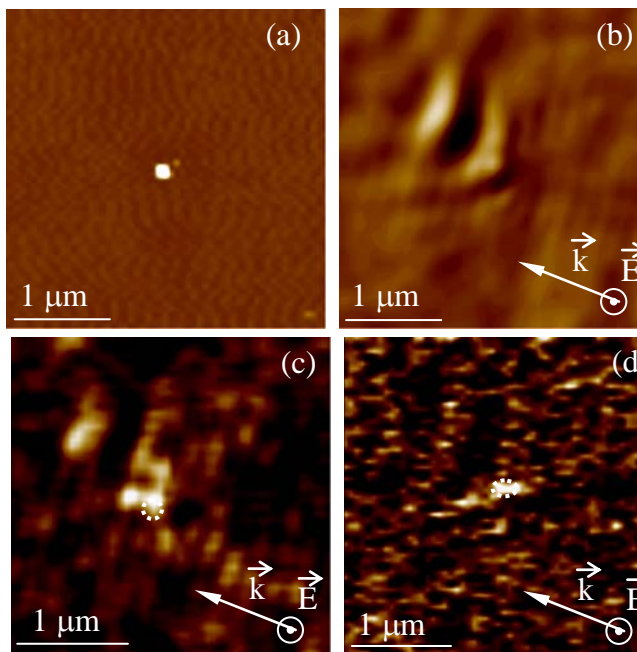


Figure 3. J-aggregate coated Ag particle (referred in the text as Dressed Particle DP) illuminated in total internal reflection on a glass substrate (situation of Fig. 1). (a) corresponds to the AFM contrast of a 40 nm diameter DP. (b)-(d) correspond to the near-field optical response of this particle for identical excitation but different detection conditions. The illumination wavelength is 415.4 nm and the polarization is TM. The NFO images represent the field polarized parallel to the plane of incidence. (b) has been recorded in the same conditions as Fig. 2(b): the optical signal modulated at the probe vibration frequency f is shown. (c) represents the second harmonic ($2f$) contribution to the optical signal modulated by the probe. (d) represents the emission from the J-aggregates at ca. 475 nm. A white dotted outline in (b) and (c) indicates the location of the particle, as obtained from the corresponding AFM images not shown here. Scan sizes are 3.34 μm for (a)-(b), 2.8 for (c) and 3.22 μm for (d).

INVESTIGATION OF FINE AND ULTRAFINE PARTICULATE MATTER FROM COMBUSTION SOURCES BY ANALYTICAL TRANSMISSION ELECTRON MICROSCOPY

Yuanzhi Chen, Naresh Shah, Frank E. Huggins, and Gerald P. Huffman

CFFS/CME, University of Kentucky, 533 South Limestone Street, Lexington, KY 40508-4005

Introduction

Combustion of coal, petroleum-based fuels and biomass results in considerable amounts of particulate matter (PM) being emitted to the ambient environment. Epidemiological studies have identified significant associations between elevated levels of airborne PM and acute adverse human health effects (1, 2). Several particle-related parameters, such as size, composition and solubility, have been linked with adverse health effects. However, there still remains considerable uncertainty regarding the actual toxicity mechanisms. Although conventional bulk analyses have been used to determine particulate species, such analyses do not provide adequate characterization of individual particles whose physical and chemical characteristics may more directly correlate with the potential toxicological mechanisms and govern their environmental impact. It is therefore desirable to develop and apply techniques that are capable of obtaining information on the size, morphology, composition, microstructure and crystallinity of individual particles.

In this study, we have applied a combination of analytical transmission electron microscopy (TEM) techniques including energy dispersive x-ray spectroscopy (EDS), selected area electron diffraction (SAED) and high-resolution TEM (HRTEM), high angle annular dark field (HAADF) scanning TEM (STEM), energy-filtered TEM (EFTEM) and electron energy loss spectroscopy (EELS) for the characterization of individual fine and ultrafine particles generated from combustion of coal, residual oil, diesel, gasoline, jet fuel and hard wood. Information on the microcharacteristics of different types of combustion-generated particles may aid epidemiological and toxicological studies aimed at discovering the underlying mechanisms that cause adverse health effects. In addition, such information also can be used in source apportionment studies that identify and quantify different source contributions to ambient PM.

Experimental

Coal fly ash (CFA) and residual oil fly ash (ROFA) PM samples were generated from combustion experiments conducted at the U.S. Environmental Protection Agency (EPA) National Risk Management Research Laboratory (NRMRL) at Research Triangle Park, NC. The CFA and ROFA were separated by a cyclone apparatus into fractions with mean diameter $>2.5\ \mu\text{m}$ ($\text{PM}_{2.5+}$) and $<2.5\ \mu\text{m}$ ($\text{PM}_{2.5}$). Three CFA PM samples including Western Kentucky $\text{PM}_{2.5}$, Wyoming PRB $\text{PM}_{2.5}$ and Montana $\text{PM}_{2.5}$, and two ROFA $\text{PM}_{2.5}$ samples (Baseline #5 $\text{PM}_{2.5}$ and high-sulfur #6 $\text{PM}_{2.5}$) were examined in this study. The diesel PM sample was produced at the diesel test engine facility at the University of Utah using a two-stroke diesel test engine (Kubota Z482B, 482 cc displacement, 2200 rpm, 6 ft.lb load). The fuel/air ratio was 0.013. The diesel fuel was a 50:50 mixture of the Chevron/Phillips reference fuels, T-22 and U-15, with an average cetane number of 46.7 and a sulfur content of 79 ppm. The gasoline PM was produced from a passenger vehicle at Ford Motor Company. PM samples from T-80 jet engine exhaust were collected at the test combustion facilities of the Wright Patterson Air Force Research

Laboratory. The hard wood PM sample was generated in combustion experiments conducted at the Lovelace Respiratory Research Institute (LRRI). These PM samples were either collected directly on TEM grids coated with lacey carbon or holey carbon films or received as powders. For powder PM samples, small amounts of them were dispersed in acetone first and then several drops of the suspensions were transferred to TEM grids coated with lacey carbon or holey carbon films. A 200 kV field emission analytical transmission electron microscope (JEOL JEM-2010F) equipped with an ultrathin-window Oxford energy dispersive x-ray spectrometer, a STEM unit, and a Gatan imaging filter (GIF) system was used to examine the PM samples.

Results and Discussion

Coal fly ash. Micron-sized CFA particles from different geological regions have been well studied in the past, however little compositional and structural information is available on ultrafine CFA particles. In this study, differences in the morphology, composition and microstructure between micron-sized and ultrafine particles have been observed in three CFA $\text{PM}_{2.5}$ samples. The micron-sized inorganic CFA particles are dominated by aluminosilicates that typically have spherical morphologies. The eastern/bituminous CFA sample (Western Kentucky $\text{PM}_{2.5}$) exhibits significant amounts of Fe-aluminosilicates, whereas the western/low rank CFA samples (Wyoming PRB and Montana) contain significant Ca-aluminosilicate particles. More detailed results are available elsewhere (3).

The ultrafine fraction of inorganic particles in the Western Kentucky $\text{PM}_{2.5}$ sample shows abundant discrete crystalline particles rich in Fe, Ti and Al. They are typically encapsulated in or associate with char particles in the form of nanocrystals. Crystalline phases, such as magnetite, rutile, lime, and Fe-Al spinel have been identified. Fe-aluminosilicate particles exhibit nonuniform distributions of Fe, Al and Si. Figure 1 left shows the TEM bright-field image of a Fe-aluminosilicate particle. Fe-rich ultrafine spherules are clearly revealed in the Fe L-edge energy-filtered elemental map (Figure 1, right). These spherules can be either cubic Fe oxides or Fe-Al spinels, while the matrix can be either aluminosilicate or silicon oxides. Such a composite structure is most likely formed from the crystallization and precipitation of spinel oxides from a molten Fe-aluminosilicate particle.

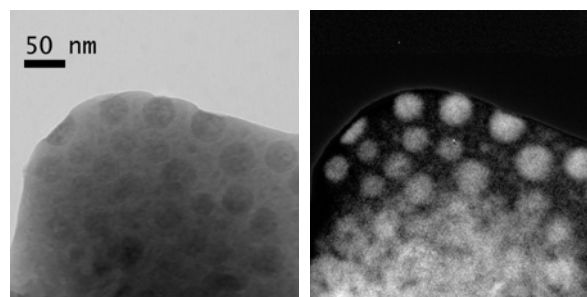


Figure 1. Left: TEM bright-field image of a Fe-aluminosilicate particle. Right: Fe-rich ultrafine spherules are revealed from the Fe L-edge energy-filtered elemental map.

The ultrafine fractions of the Wyoming PRB and Montana $\text{PM}_{2.5}$ samples contain considerable amounts of alkaline-earth-element aggregates in the form of phosphates, silicates, and sulfates and mixed species. Most of them show crystalline or crystalline plus amorphous characteristics. Figure 2 shows the typical morphology of

ultrafine calcium phosphates observed in the western/low rank CFA samples. The primary particles of this aggregate are typically 30-60 nm in size. EDS spectrum of this aggregate shows dominant Ca and P as well as minor amounts of S, Mg and Ba.

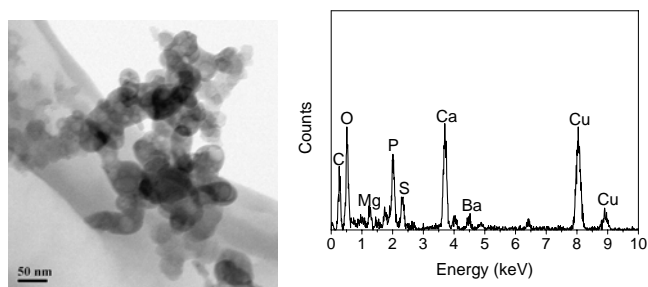


Figure 2. Micrograph (left) and EDS spectrum (right) of ultrafine Western low-rank coal fly ash particles. Cu peaks are due to TEM grids.

Carbonaceous particles are also present in the CFA PM samples in addition to the inorganic particles. Char particles that typically have porous structures with near spherical or irregular shapes are typically present in the micron-sized fraction, whereas soot aggregates are the dominant features in the ultrafine and submicron fractions. Typical ultrafine soot aggregates have near spherical primary particles with sizes of 30–50 nm. An onion-like microtexture that consists of concentrically stacked graphitic layers can be observed in the primary particles. A typical HRTEM image of combustion generated soot primary particle is shown in Figure 3. The onion-like microtexture in Figure 3 has also been observed in other soot primary particles generated from combustion of residual oil, diesel, gasoline, jet fuel, and hard wood, which will be discussed later. The carbonaceous soot aggregates in the western low-rank CFA PM samples are typically mixed or coated with alkali and alkaline earth inorganic species, which might be useful as a fingerprint in source apportionment studies.

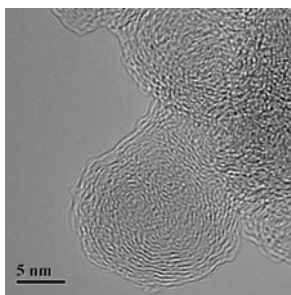


Figure 3. Typical HRTEM image of a combustion-generated soot primary particle showing microtextures consisting of concentrically stacked graphitic layers.

Residual oil fly ash. ROFA PM is dominated by carbonaceous particles, which exist in two distinctive forms, i.e. as soot aggregates with spherical primary particles of size 10 – 80 nm and as larger spherical or irregular-shaped porous residual char particles of size 1 - 20 μm . The microstructure of ROFA soot primary particles also exhibits concentrically stacked graphitic layers similar to those of soot primary particles present in CFA PM samples. The microstructure of char particles exhibits order-deficient arrangements of clusters consisting of several subparallel graphitic layers. Compositional analyses by EDS indicate that the char particles

typically have much higher sulfur contents than the soot particles. V and P, which are basically absent in the residual oil soot particles, are frequently observed in the char particles (4). The metallic elements may originate from organically bound species (e.g. porphyrins) in the parent fuel. Both types of carbonaceous particles, especially the char particles, are often found mixed/coated with external transition metal compounds. Figure 4 shows the mapping of carbonaceous particles mixed/coated with inorganic species containing S, Ca, V and Ni. Such carbonaceous particles could effectively act as a catalyst “support” for transition metal compounds that catalyze chemical reactions in the atmosphere and biochemical processes in the body.

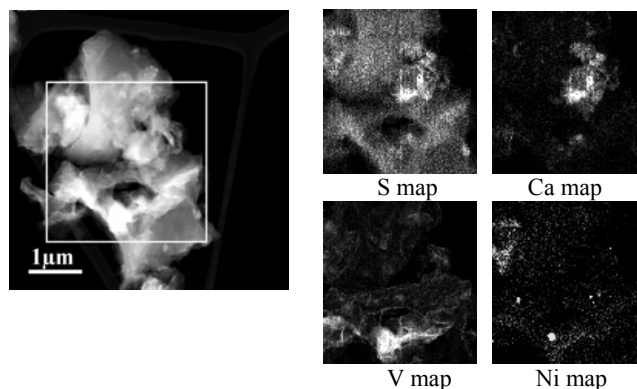


Figure 4. HAADF image (left) and STEM/EDS mapping (right) of ROFA carbonaceous particles mixed/coated with inorganic compounds.

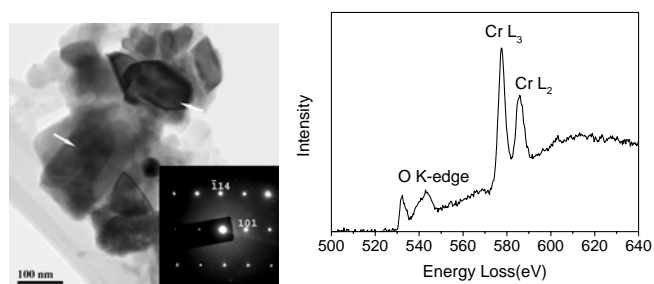


Figure 5. Micrograph (left) and EELS spectrum (right) of crystalline chromium oxide (Cr_2O_3) particles identified in ROFA PM samples. The SAED pattern (inset) is indexed to a trigonal crystalline structure. The Cr L-edge reveals a valence of +3.

Inorganic species in these two high sulfur ROFA $\text{PM}_{2.5}$ samples exist mainly in the form of sulfates. In addition, transition metal oxides, vanadates, phosphates, and sulfides have also been identified. Considerable amounts of the particles exhibit crystalline characteristics. Figure 5 (left) shows several chromium oxide (Cr_2O_3) particles. The SAED pattern (inset) reveals a trigonal crystalline structure. The valence state of Cr can be obtained from comparison of the peak position of Cr L-edges with EELS spectra of Cr compound standards. The Cr L-edge EELS spectrum recorded from the particles in Figure 5 indicates a valence of +3. The valence state of V in some V-rich oxide particles was found to vary from +2 to +5. Individual transition metal sulfate, oxide, and phosphate particles typically exhibit complex compositions containing multiple metallic elements. Many of the oxide particles exhibit a spinel crystalline structure,

which is capable of incorporating multiple metallic elements with variable valency. More detailed results regarding the ROFA PM samples are available in references 4-6.

Diesel PM. Diesel PM is dominated by ultrafine soot aggregates. The primary particles typically have a size ~20-50 nm, although some smaller (down to 5 nm) or larger (up to 80 nm) particles can also be found. The sizes of soot aggregates are typically in the range of 0.1-1 μm . The microstructures of the diesel soot primary particles are very similar to those of coal and residual oil soot primary particles. Concentric arrangements of stacked graphitic layers and multiple spherical nuclei surrounded by several graphitic layers were observed in many soot primary particles. The measured BSU (basic structural unit) parameters of the diesel soot primary particles, including the average distance of interlayer spacings (d_{002}), the stacked layer length (L_a) and the layer thickness (L_c) from the 002 lattice fringe images, are also close to those of coal and residual oil soot primary particles. Such results indicate a common characteristic of soot particles generated via a vaporization-condensation mechanism during different combustion processes.

The chemical composition of diesel soot primary particles was examined by using STEM/EDS. The EDS spectrum (Figure 6 (top)) shows a strong carbon peak and a much weaker oxygen peak. The sulfur peak is basically indiscernible in the spectrum. In contrast, the typical EDS spectrum of coal and residual oil soot primary particles (Figure 6 (bottom)) exhibit a much stronger sulfur peak, which reflects the higher content of sulfur in the parent fuels. This difference could serve as an important compositional signature that may be used to differentiate between soot particles generated from low-sulfur content fuels and high-sulfur content fuels.

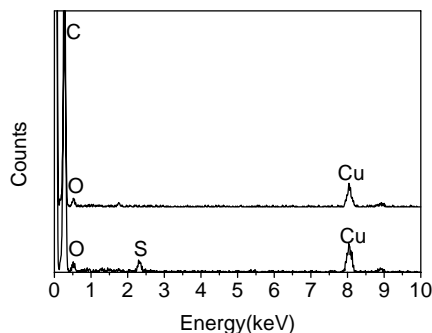


Figure 6. Comparison of typical EDS spectra of soot primary particles generated from low-sulfur content fuels (top) and from high-sulfur content fuels (bottom).

Gasoline PM. Two types of carbonaceous particles have been observed in gasoline PM. One is the soot aggregates, which typically exhibit smaller aggregate sizes and more compact morphologies (Figure 7 (top right)) compared to diesel soot aggregates. HRTEM images recorded from the soot primary particles also show concentric arrangements of stacked graphitic layers, although some of the primary particles may have morphologies far deviated from the perfectly spherical shape. The EDS spectra of soot primary particles are basically very close to those of diesel soot particles. The other type of carbonaceous particle exhibits a fuzzy morphology with an undefined shape (Figure 7 (top left)). They typically have a size in the micron range and show rather refractory behavior under the exposure of electron beams. EDS spectra of this type of particle show only carbon and oxygen peaks. Since they have a very low contrast

and show a semi-transparent appearance, they could be the refractory organic species condensed from the gas phases.

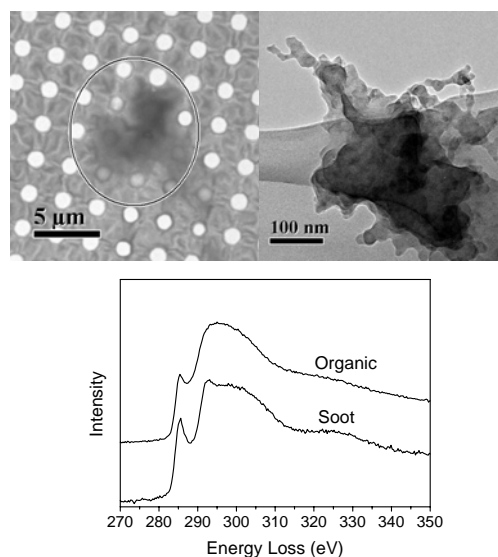


Figure 7. Micrograph of an organic-type carbonaceous particle (top left) and soot aggregates with compact morphologies (top right) observed in gasoline PM samples. Their carbon K-edge EELS spectra are shown in the figure below.

The microstructural differences between these two types of carbonaceous particles are reflected in their carbon K-edge EELS spectra. The soot particles (Figure 7 (bottom)) show a sharper $1s-\pi^*$ peak at 285.4 eV and a discernible $1s-\sigma^*$ peak at 292.4 eV. However, the organic-type carbonaceous particle exhibits much more amorphous characteristics, which can be discerned from the broadened $1s-\pi^*$ peak and the disappearance of the $1s-\sigma^*$ peak, which is replaced by an averaged broad peak ranging from 290 to 300 eV. Such microstructural differences are also easily verified from their HRTEM images. Stacked graphitic layers cannot be observed in the HRTEM image of the organic-type carbonaceous particle.

Jet PM. Compared to broad research of the particulate formation from combustion of diesel fuel, the information about individual particles generated from jet engines is limited. The jet PM examined in this study typically exhibits short (less than 0.4 μm) soot aggregates. Spherical soot primary particles can be discerned from the close examination of the soot aggregates. Some large soot aggregates (up to several microns) with compact morphologies have also been identified. Most of the soot primary particles appear to fuse together and the boundary between each primary particle can not be clearly discerned. This may relate to the higher temperatures and pressures present in the jet engine. EDS spectra recorded from the carbonaceous particles show only carbon and oxygen peaks and are very similar to those from gasoline PM.

Carbonaceous particles intermixed with particles rich in metallic elements have also been observed in the jet PM samples. Figure 8 shows the HAADF image of a carbonaceous particle intermixing with metallic species. STEM/EDS elemental mapping shows that most of the bright spots present in the HAADF image containing mainly Fe and minor amount of Cr. Fe and Cr are the major components of stainless steel. It is very likely that these metallic species come from wear of an engine component because the engine is run under the high temperature and pressure. These metallic elements could be an important source signature of jet PM.

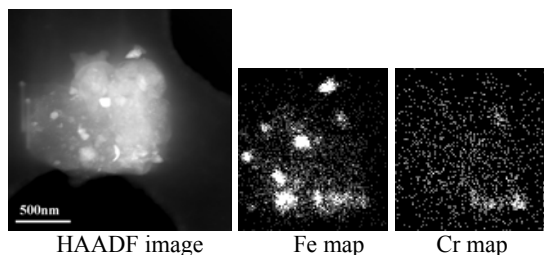


Figure 8. HAADF image and Fe and Cr elemental maps of a carbonaceous particle decorated with particles rich in metallic elements in a jet PM sample.

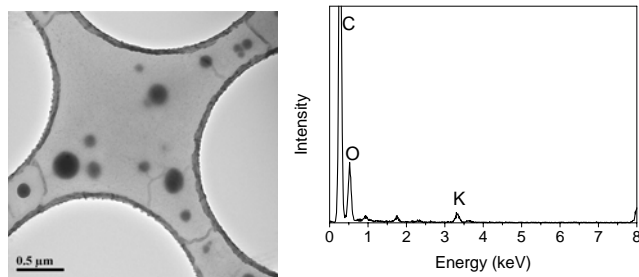


Figure 9. Micrograph (left) and EDS spectrum (right) of K-containing tar ball particles observed in the hard wood PM sample.

Hard wood PM. The hard wood PM sample is dominated by carbonaceous particles that can be subdivided into three types. The first type does not have a distinct morphology. They are very likely condensed from organic gas phases. Their amorphous characteristics are verified by electron diffraction patterns, which show broad diffuse diffraction rings. Carbon is the major elemental component of this type of particles. In addition, minor amounts of oxygen and potassium are also present. The second type has a spherical morphology (Figure 9 (left)) and is termed as “tar ball” in the text. The tar balls are amorphous and stable under electron beam. They usually exist separately and do not form aggregates with each other or with other particles. EDS spectra recorded from the tar ball particles (Figure 9 (right)) show the presence of weak potassium and oxygen peaks in addition to the dominant carbon peak. These carbonaceous particles lack the morphological and microstructural features of soot particles and are assumed to be nucleated directly from organic gas phases. The last type is soot aggregates, which is clearly distinguishable from the first two types. They show very similar morphologies and microstructures to those of coal and oil soot aggregates. The numbers of the first two types of carbonaceous particles are much more than that of soot particles. The combustion parameters, such as air/fuel ratios, may affect the final carbon format. For example, smoke from smoldering combustion has been found contained much less soot than that from flaming combustion (7). Organic-type carbonaceous particles that contain minor amounts of K were also observed in a study on the biomass burning in southern Africa (8). The K-containing characteristic could be an important compositional signature for identifying biomass-generated carbonaceous PM.

Conclusions

Ultrafine soot aggregates are the typical representative of carbonaceous particles formed via vaporization-condensation mechanisms during combustion processes. They have been observed in all the PM samples investigated in this study. An important compositional signature of soot particles is that soot particles in CFA and ROFA PM samples typically have higher sulfur contents compared with diesel and gasoline soot particles. Porous or solid char particles with sizes in the micron range are typical for CFA and ROFA PM samples. Some organic-type carbonaceous particles, which are more common in gasoline, jet and hard wood PM samples have also been observed. They exhibit different microstructures compared to soot particles. Jet PM contains carbonaceous particles intermixed with metallic elements. Hard wood PM can be distinguished by the presence of K-containing spherical tar ball particles.

Inorganic ultrafine CFA particles show quite different morphologies, compositions and microstructures compared with inorganic particles in coarser, micron-size fractions. An eastern bituminous CFA sample (Western Kentucky) showed abundant discrete crystalline particles rich in Fe, Ti and Al, whereas Western low-rank CFA samples (Wyoming PRB and Montana) contained considerable amounts of alkaline-earth element aggregates in the form of phosphates, silicates, and sulfates and mixed species. The major chemical form of inorganic species in the two high sulfur ROFA PM_{2.5} samples (High Sulfur #6 and Baseline #5) is sulfates. In addition, transition metal oxides, vanadates, phosphates, and sulfides were also identified. Individual transition metal sulfate, oxide, and phosphate particles are typically compositionally complex, containing multiple metallic elements.

Acknowledgments

The authors would like to thank Dr. William P. Linak and Dr. C. Andrew Miller of U.S. EPA, NRMRL for generating the CFA and ROFA PM samples, Ms. Kerry Kelly of University of Utah for generating the diesel PM samples, Lovelace Respiratory Research Institute for supplying the wood smoke PM samples, and Dr. Alan Dozier for his kind help in operating the transmission electron microscopes. This research was supported by the National Science Foundation under CRAEMS grant CHE-0089133.

References

- (1) Dockery, D. W.; Pope, C. A. *Ann. Rev. of Publ. Health*, **1994**, *15*, 107-132.
- (2) Schwartz, J.; Dockery D. W.; Neas, L. M. *J. Air & Waste Manage. Assoc.* **1996**, *46*, 927-939.
- (3) Chen, Y.; Shah, N.; Huggins, F. E.; Huffman, G. P.; Linak, W. P.; Miller, C. A. *Fuel Process. Technol.* **2004**, *85*, 743-761.
- (4) Chen, Y.; Shah, N.; Huggins, F. E.; Huffman, G. P. *Environ. Sci. Technol.* **2005** (In press)
- (5) Huffman, G. P.; Huggins, F. E.; Shah, N.; Huggins, R.; Linak, W. P.; Miller, C. A.; Pugmire, R. J.; Meuzelaar, H. L. C.; Seehra, M. S.; Mannivannan, A. *J. Air Waste Manage. Assoc.* **2000**, *50*, 1106-1114.
- (6) Huggins, F. E.; Shah, N.; Huffman, G. P.; Robertson, J. D. *Fuel Process. Technol.* **2000**, *65-66*, 203-218.
- (7) Patterson, E. M.; McMahon, C. K. *Atmos. Environ.* **1984**, *18*, 1825-182551.
- (8) Pósfai, M.; Simonics, R.; Li, J.; Hobbs P. V.; Buseck, P. R. *J. Geophys. Res.* **2003**, *108*, SAF 19/1-SAF 19/12.

CHARACTERIZATION OF PETROLEUM BY HIGH RESOLUTION FIELD DESORPTION/IONIZATION AND ATMOSPHERIC PRESSURE PHOTOIONIZATION FT-ICR MASS SPECTROMETRY

Alan G. Marshall,^{1,2} Sunghwan Kim,² Tanner M. Schaub,² Jeremiah M. Purcell,¹ Donald F. Smith,¹ and Ryan P. Rodgers^{1,2}

¹ Department of Chemistry and Biochemistry, Florida State University, Tallahassee, Florida 32306.

² Ion Cyclotron Resonance Program, National High Magnetic Field Laboratory, Florida State University, 1800 E Paul Dirac Drive, Tallahassee, Florida 32310-4005.

Introduction

Fourier transform ion cyclotron resonance mass spectrometry (FT-ICR MS) analysis of crude oil achieves sufficient mass resolving power ($m/\Delta m_{50\%} > 450,000$ in which $\Delta m_{50\%}$ denotes mass spectral peak full width at half height) and high mass accuracy (< 1 ppm) to allow for the baseline resolution and elemental composition assignment of thousands of heteroatomic species in a single crude oil.¹ Electrospray ionization (ESI) is limited to polar (N, S, and/or O-containing) species that are readily protonated (positive ions) or deprotonated (negative ions). Here, we couple two other ionization methods (field desorption (FD) and atmospheric pressure photoionization (APPI) to probe the much larger fraction of nonpolar (e.g., aromatic hydrocarbons, thiophenes), illustrated for the aromatic fraction of crude oil.

Experimental

Crude Oil Samples. The procedure used to fractionate the aromatic compounds from these samples is similar to that described in ASTM D2007² in which petroleum is separated into saturate, aromatic, and polar fractions. FD-generated positive ions were formed by continuous application (75 nL/min) of dilute sample solution (100 $\mu\text{g/mL}$ in methylene chloride) delivered to the FD emitter by a syringe pump through a 50 cm long, 10 μm i.d. fused silica capillary. Following a several minute delay for pressure equilibration, the pressure in the source vacuum chamber was 1×10^{-5} Torr. For APPI, the aromatic fraction isolated from S.A. crude oil was dissolved in toluene to yield a 2 mg/mL stock solution. A 1/50 dilution into toluene was used for the analysis. Naphtho-a-pyrene (NAP) @ 10 $\mu\text{g/mL}$ was introduced as a standard.

Mass Analysis. The crude oils were analyzed at the National High Magnetic Field Laboratory (NHMFL) with a previously described homebuilt 9.4 Tesla Fourier transform mass spectrometer. Continuous-flow FD FT-ICR MS was performed as previously described.³ APPI was carried out with a ThermoFinnigan ion source (<http://www.thermo.com>) interfaced via octopole ion guides and an external octopole ion trap for injection into a homebuilt 9.4 T FT-ICR mass spectrometer. The performance of the APPI source was evaluated over flow rates between 50 – 400 $\mu\text{L/min}$ and desolvation temperatures between 185 – 400 $^{\circ}\text{C}$. The gas flow was kept constant at a regulator defined 80 psi. 100 time-domain transients were co-added for each sample and stored for later Fast Fourier transformation and frequency-to-mass conversion. The stored time-domain signal was Hanning-apodized and zero-filled once prior to fast Fourier transformation and generation of the magnitude-mode frequency domain spectrum. A modular ICR data system (MIDAS) data station, developed in-house, provides instrument control, data acquisition, and data analysis. Mass spectra

were internally calibrated with respect to a known homologous series of alkylbenzenes. Homologous series were separated and grouped by nominal Kendrick mass and Kendrick mass defect to facilitate rapid identification, as described elsewhere.⁵

Results and Discussion

The broadband FD FT-ICR mass spectrum in Figure 1 shows prominent homologous series of intact alkylated aromatics and thiophenes, species not observable by ESI. Saturated hydrocarbons tend to fragment during external ion accumulation. The ultrahigh mass resolving power shown in Fig. 2 enables unique assignment of elemental compositions, and in particular resolves sulfur-containing species from others.

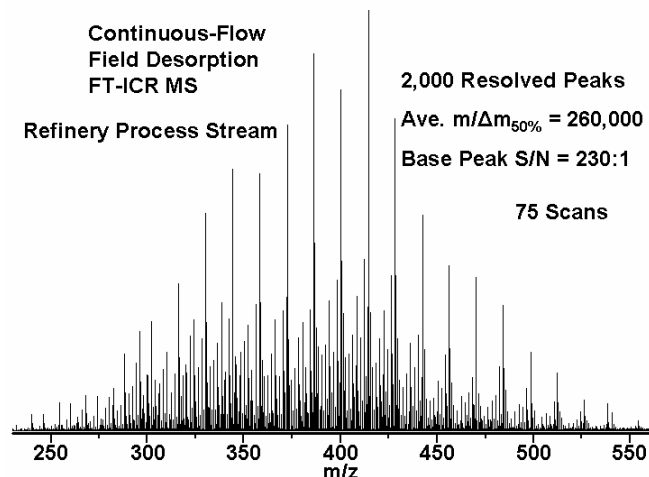


Figure 1. Continuous-flow FD FT-ICR mass spectrum of a refinery process stream sample. The spectrum is the ensemble average of 75 time domain signals collected in one hour. (From Ref. 4)

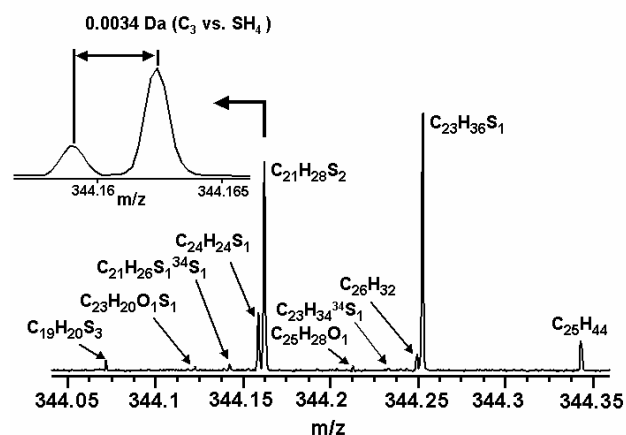


Figure 2. Mass scale expansion at nominal mass 344 Da from the broadband mass spectrum shown in Figure 2. The resolution of the 3.4 mDa C_3 vs. SH_4 split can be observed at m/z 344.25 and separately in the inset at m/z 344.16. (From Ref. 4)

Figure 3 shows a broadband APPI FT-ICR mass spectrum. As for FD, APPI reveals aromatic non-polars and thiophenes. Figure 4 illustrates the rich compositional complexity of the nonpolar components, with 40 distinct elemental compositions at a single nominal mass (m/z 428). Both FD and APPI generate singly-charged ions almost exclusively.

Although positive-ion FD produces primarily odd-electron radical ions, APPI generates both protonated and radical cations, as shown in Fig. 5 for naphtho[a]pyrene. Only FT-ICR MS is capable of resolving the $^{12}\text{C}_n\text{H}$ (even-electron) its $^{13}\text{C}^{12}\text{C}_{n-1}$ (odd-electron) counterpart. It is interesting to note that APPI generates five-membered **pyrrolic** nitrogen species as radical cations but six-membered **pyridinic** nitrogen species as protonated even-electron ions. Thus, five- and six-membered rings are readily distinguished by their half-integer vs. integer double bond equivalent values.

We are currently evaluating the relative advantages of FD vs. APPI relative to ESI for analysis of petroleum samples, and will report those results.

APPI FT-ICR Mass Spectrum:
Aromatic Fraction of Crude Oil
100 Summed Scans, Positive Ions

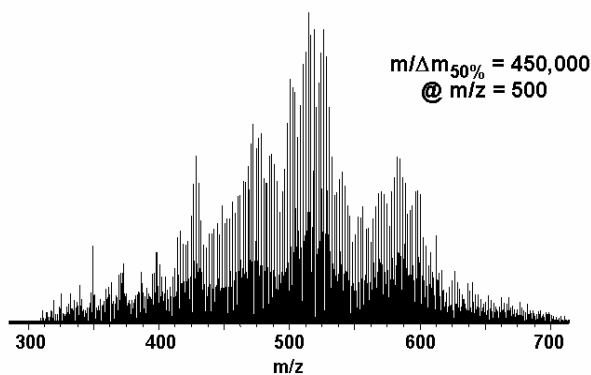


Figure 3. APPI FT-ICR broadband mass spectrum of the aromatic fraction of S. American crude oil.

APPI FT-ICR Mass Spectrum
Aromatic Fraction of S.A. Crude Oil
100 Summed Scans, Positive Ions
Zoom Mass Inset @ m/z 428

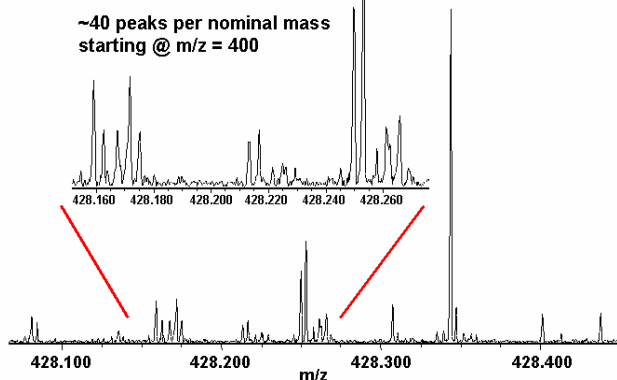


Figure 4. APPI FT-ICR mass spectral segment of the aromatic fraction of S. American crude oil.

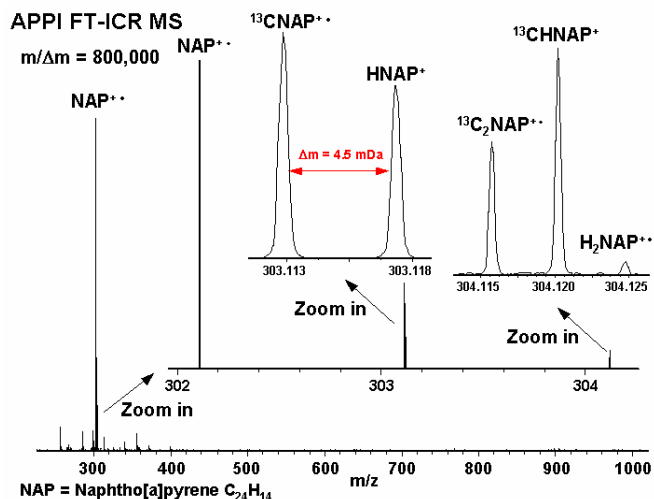


Figure 5. Optimized APPI FT-ICR mass spectrum of naphtho[a]pyrene, acquired at a flow rate of 50 $\mu\text{L}/\text{min}$ at $\sim 200^\circ\text{C}$. Note the presence (and resolution) of even- and odd-electron species.

Acknowledgments

The authors thank Kuangnan Qian for providing the oil samples and for his many helpful discussions. This work was supported by ExxonMobil Research and Engineering Co., NSF CHE-99-09502, Florida State University, and the National High Magnetic Field Laboratory in Tallahassee, FL.

References

1. Qian, K.; Robbins, W. K.; Hughey, C. A.; Cooper, H. J.; Rodgers, R. P.; Marshall, A. G., *Energy and Fuels*, **2001**, 1505-1511
2. ASTM D 2007-03, Annual Book of ASTM Standards, In *Standard Test Method for Characteristic Groups in Rubber Extender and Processing Oils and Other Petroleum-Derived Oils by the Clay-Gel Absorption Chromatographic Method*; 2003 Edition ed.; ASTM, 2003.
3. Schaub, T. M.; Hendrickson, C. L.; Qian, K.; Quinn, J. P.; Marshall, A. G. "High-Resolution Field Desorption Ionization Fourier Transform Ion Cyclotron Resonance High-Resolution Mass Analysis of Non-Polar Molecules," *Anal. Chem.* **2003**, 75, 2172-2176.
4. Schaub, T. M.; Linden, H. B.; Hendrickson, C. L.; Marshall, A. G. "Continuous Flow Sample Introduction for Field Desorption/Ionization Mass Spectrometry," *Rapid Commun. Mass Spectrom.* **2004**, 18, 1641-1644.
5. Hughey, C. A.; Hendrickson, C. L.; Rodgers, R. P.; Marshall, A. G.; Qian, K. "Kendrick Mass Defect Spectroscopy: A Compact Visual Analysis for Ultrahigh-Resolution Broadband Mass Spectra," *Anal. Chem.* **2001**, 73, 4676-4681.

CHARACTERIZATION OF CONJUGATED DIOLEFINS IN PETROLEUM REFINING PRODUCTS

Kuangnan Qian, Kathleen E. Edwards, Frank C. Wang and
Mike Siskin

ExxonMobil Research and Engineering Company
1545 Route 22 East, Annandale, NJ 08801

Introduction

Conjugated diolefins are largely responsible for molecular weight growth reactions (fouling) in various refinery processes, such as hydrocracking and hydroconversion, and in refinery equipment such as heat exchangers, furnaces, fractionators and reactors. These compounds can rapidly react with trace amounts of oxygen in air, forming hydroperoxides and peroxides. Upon heating from room temperature, through the range up to about 300°C, these peroxides, even at sub ppm levels, initiate free radical chain reactions, resulting in oligomerization reactions/gum formation and eventually in insoluble deposits. Currently, small conjugated dienes (smaller than C₆) in low-boiling hydrocarbon mixtures are determined by high resolution GC/FID. There is no reliable method to identify and quantify larger conjugated dienes (C₆⁺). The issue becomes more acute for more complicated matrices, such as FCC naphtha.

4-Methyl-1,2,4-triazoline-3,5-dione (MTAD) reacts rapidly with conjugated dienes via a Diels-Alder addition reaction. MTAD derivatization combined with GC/MS has been used to determine double bond position in fatty acids and other naturally occurring organic compounds^{2,3}. Here we report a method for the selective and rapid room temperature derivatization of conjugated dienes using MTAD followed by chemical ionization (CI) GC/MS and GC nitrogen chemiluminescence detection (NCD) analyses. The method has been successfully applied to the determination of the types and concentrations of conjugated dienes in steam cracked naphtha, coker naphtha and catalytic cracked naphtha.

Experimental

A stock solution of MTAD (0.442 M) was prepared by dissolving MTAD (250 mg) in methylene chloride (5 mL). An aliquot of the stock solution is directly mixed with hydrocarbon samples at room temperature to derivatize the conjugated structures. MTAD selectively and rapidly (usually <5 sec) reacts with linear and cyclic conjugated dienes as illustrated in Figure 1. The MTAD loading needs to be optimized to quantitatively derivatize all conjugated dienes in the sample.

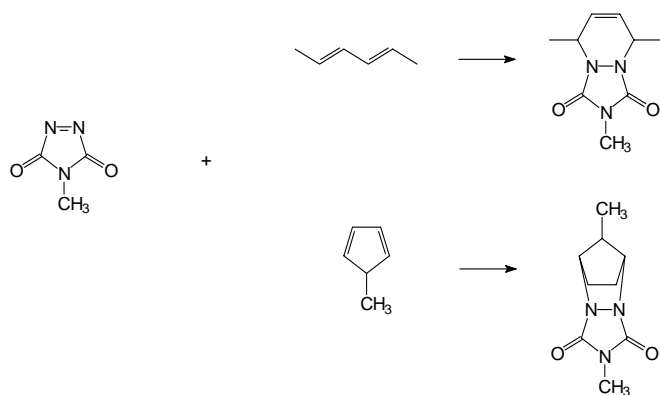


Figure 1. MTAD Derivatization of Conjugated Diolefins

The GC/NCD experiments were conducted on a HP 5890 Series II GC with an Antek 705E NCD detector. A split inlet was used at a 25:1 split ratio. The oven was ramped from 50°C to 320°C at 10°C/min. A SUPELCO PTA-5, 30 meter capillary column with a 0.32 mm ID and a 0.50 µm film thickness was used. The GC/MS experiments were conducted on a HP 5890 Series II GC with a HP 5989B MS Engine. The inlet temperature was 275°C. A split inlet was used at a 25:1 split ratio. The oven was ramped from 40°C to 300°C at 10°C/min. A 30 meter SPB-5 capillary column with a 0.32 mm ID and a 0.25 µm film thickness was used. 1,3-Cycloheptadiene was chosen as an internal standard for quantification purposes. The derivatized samples were analyzed by GC/NCD to determine the total molar concentration of conjugated dienes. The derivatized samples were also analyzed in parallel by GC/MS to determine the carbon number distribution of conjugated dienes. Molecules were ionized by Chemical ionization (CI) using deuterated ammonia (ND₃). The selected ion display of the deuterated molecular ion [M+D]⁺ and ND₄ adduct [M + ND₄]⁺ was used to differentiate the various conjugated dienes.

Results and Discussion

A mixture of model compounds that are typically present in a naphtha sample were derivatized and analyzed by MTAD-GC/MS. The results showed that MTAD did not react with paraffins, linear olefins, cycloparaffins, and aromatics. Cycloolefins and aromatic olefins partially react with MTAD in the derivatization process. Conjugated dienes react 100% with MTAD. The conjugated diene-MTAD adducts can be readily identified by mass spectrometry. Figure 2 illustrates the mass spectra of MTAD adducts of three conjugated diene model compounds, 1,3-pentadiene, 2,4-hexadiene and 2,4-heptadiene, respectively.

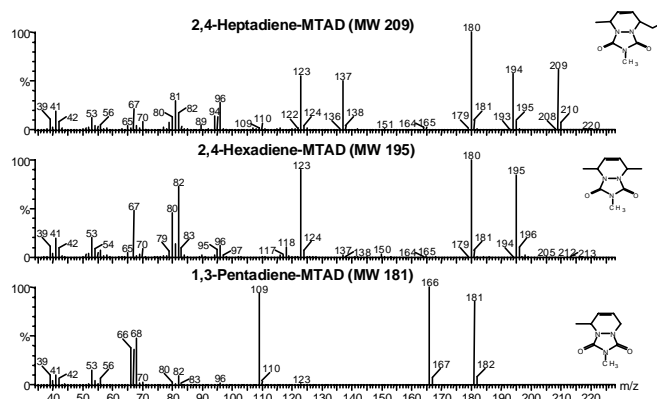


Figure 2. 70 EI GC/MS Spectra of Conjugated Diolefins

The compositions of real petroleum samples (e.g. steam cracked naphtha (SCN) and catalytic cracked naphtha (HCN)) are much more complicated. Figure 3 shows the GC/MS TIC of a SCN before and after MTAD derivatization. The MTAD derivatization converted conjugated dienes into adducts and appear at retention times longer than 20 min after most hydrocarbon components have eluted. The shift in retention time makes it straight forward to distinguish the MTAD products from the hydrocarbon matrix. The chromatography peaks before 20 minutes were simplified due to the removal of conjugated dienes and partial removal of styrenes and indenes. The MTAD adducts of these eluted after 26 minutes.

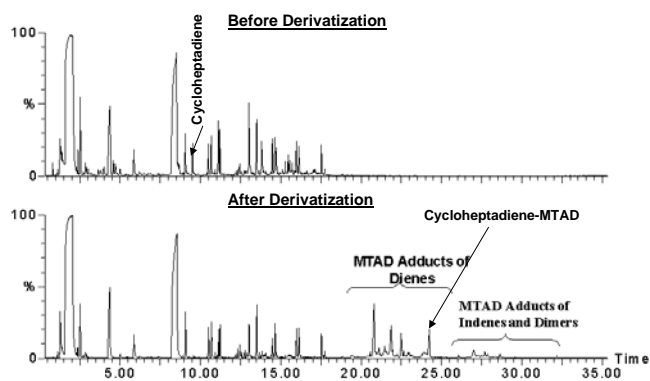


Figure 3. A Steam Cracked Naphtha Before and After MTAD Derivatization

GC resolves isomers of diene-MTAD adducts. The retention times of the diene-MTAD adducts are mainly influenced by their isomeric structure rather than by their molecular weight. Consequently, conjugated diene-MTAD adducts with different carbon numbers can overlap in chromatography. GC/MS with selected ion monitoring becomes necessary to differentiate the isomeric conjugated dienes.

Since MTAD adducts each contain 3 nitrogen atoms, GC with a nitrogen chemiluminescence detector becomes very useful to selectively detect and quantify the total MTAD adducts. We evaluated the relative sensitivities of 12 model compounds of conjugated dienes by GC/NCD and EI-GC/MS, respectively. GC/NCD gives a quite uniform response. The molecular ion intensities of EI-GC/MS vary significantly due to different degrees of fragmentation of the MTAD adducts. Chemical ionization can significantly reduce the fragmentation by forming protonated molecular ions. Figure 4 compares the mass spectra of C_7 linear conjugated dienes by 70 eV EI and by CI using CH_4 and ND_3 as reagent gases, respectively. In CH_4 CI, molecules tend to form protonated molecular ion $[M+H]^+$ and ethyl cation adducts $[M+C_2H_5]^+$, which can cause mass overlaps for dienes with different carbon numbers, e.g. $C_5 + C_2H_5^+$ overlap with $C_7 + H^+$. In ND_3 CI, molecules tend to form deuterated molecular ions $[M+D]^+$ and deuterated ammonium cation adducts $[M+ND_4]^+$ thus eliminating the overlap. Chemical ionization minimized variations in response factors. The relative response factors for the dienes of the same carbon number are very similar.

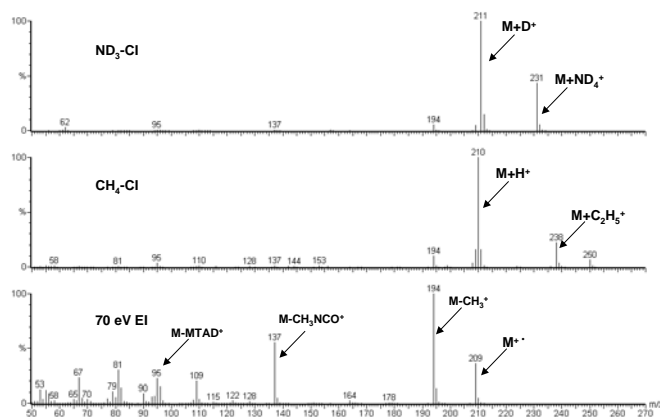


Figure 4. Mass Spectra of Conjugated Diolefins in 70 eV EI, CH_4 CI and ND_3 CI

The quantification of conjugated dienes can be made only when all the dienes are converted into the adducts. Model compound studies showed that 100% conversion can be reached when the ratio of the molar concentration of MTAD to the conjugated diene is between 2 and 10. When the ratio is below 2, the MTAD reaction is incomplete. When the ratio is greater than 10, self-polymerization of MTAD becomes predominant and results in the reduction of MTAD-conjugated diene adducts. The excess MTAD loading becomes a greater problem for real sample analyses. The higher loading causes an elevated baseline in the GC/NCD chromatogram, making accurate peak quantification difficult. The optimum MTAD:Diene ratio is between 2 to 4. This implies that for unknown samples, a series of experiments need to be conducted to assure that appropriate MTAD loading is used.

For quantification purposes, the total levels of conjugated dienes are determined using an internal standard, in this case, cycloheptadiene. The selected ion display of pseudo molecular ions by ND_3 GC/MS was used to determine the carbon number distribution. We have applied the method to steam cracked naphtha before and after hydrotreating. Conjugated dienes are significantly reduced after hydrotreating. Linear and cyclic conjugated dienes with a carbon number ranging from C_4 to C_{10} can be quantified by this method.

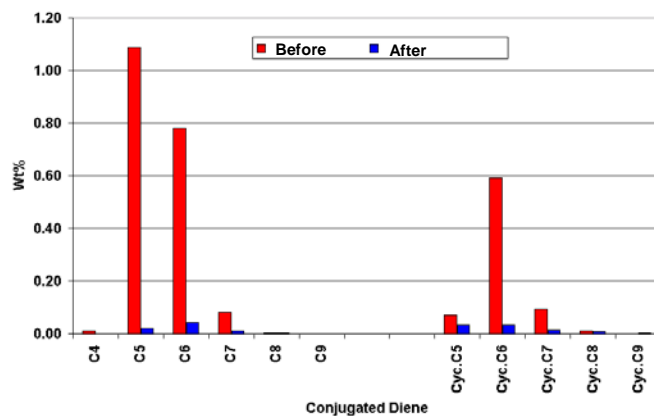


Figure 5. Concentrations of Conjugated Diolefins Before and After Hydrotreating

Conclusions

MTAD derivatization combined with GC-NCD and GC/MS (ND_3 CI) can detect and quantify the concentrations of up to C_{10} linear and cyclic conjugated dienes in highly complex hydrocarbon matrices. GC-NCD provides total level of conjugated dienes. GC/MS provides detailed carbon number and linear/cyclic distributions.

Acknowledgement. We acknowledge many valuable discussions with John W. Diehl and Frank P. DiSanzo in the development of this methodology. We also thank Norman E. Hoosain and Anita D. Linsenmayer for assisting GC/MS and GC/NCD experiments, respectively.

References

- (1) Radl, S. *Advances in Heterocyclic Chemistry*, **1997**.
- (2) Dobson, G. *Journal of the American Oil Chemists' Society* **1998**, 75, 137-142.
- (3) Young, D. C.; Vouros, P.; Decosta, B.; Holick, M. F. *Anal. Chem.* **1987**, 59, 1954-1957.

CHARACTERIZATION AND APPLICATION OF SESQUITERPANES FOR OIL SPILL STUDIES

Zhendi Wang*, C. Yang, M. Fingas, and B. Hollebone

Emergencies Science and Technology Division
Environmental Technology Centre, Environment Canada
335 River Road, Ottawa, Ontario, Canada K1A 0H3
Tel: (613) 990-1597, Fax: (613) 991-9485
E-mail: zhendi.wang@ec.gc.ca

INTRODUCTION

Polymethyl-substituted decalins (C_{14} - C_{16} bicyclic alkanes), i.e. hydrocarbons of the sesquiterpane type were first reported in 1974 and discovered in crudes of the Loma Novia and Anastasievsko-Troyitskoe deposits (1). Alexander et al. later identified and confirmed the existence of 8 β (H)-drimane and 4 β (H)-eudesmane in most Australian oils (2). Noble (3) identified a series of C_{14} to C_{16} sesquiterpane isomers using synthesized standards and mass spectral studies. Various sesquiterpanes, with the greatest enrichment in condensate, were also identified by Simoneit et al. from fossil resins, sediments and crude oils (4), and by Chen and He from a great offshore condensate field of Liaodong Bay, Northern China (5).

The bicyclic biomarker sesquiterpanes with the drimane skeleton are ubiquitous components of crude oils and ancient sediments. Most sesquiterpanes probably originate not only from high plants but also from algae or bacteria. During the thermal evolution, the relative concentration of C_{14} sesquiterpanes decreases with increasing maturation of organic matters. The concentration of C_{14} bicyclic sesquiterpanes is higher at the immature stage, while those of C_{15} drimane and C_{16} homodrimane are relatively lower. As a result of the dehydroxylation and chemo-dynamics of their higher molecular weight precursors, the concentrations of drimane (C_{15}) and homodrimanes (C_{16}) gradually increase, but the concentration of C_{14} sesquiterpanes becomes lower.

Though biomarker sesquiterpanes and diamondoids have increasing applications in petroleum exploration in recent years, there are very few studies on utilization of sesquiterpanes and diamondoids to environmental forensic investigations and oil spill identifications. For lighter petroleum products, refining processes have removed most high-molecular weight biomarkers from the corresponding crude oil feed stocks. Thus, the high boiling point pentacyclic triterpanes and steranes are generally absent in lighter petroleum products jet fuels and most diesels, while the smaller bicyclic sesquiterpanes including eudesmane and drimane get greatly concentrated in these petroleum products. Therefore, examination of GC-MS chromatograms of these bicyclic biomarkers can provide a comparable and highly diagnostic means of comparison for lighter petroleum products. In this work, sesquiterpanes in crude oils and petroleum products are identified and characterized; the distributions of sesquiterpanes in different oils, oil distillation fractions and refined products are compared. Weathering effects on sesquiterpane distribution are quantitatively studied. A number of diagnostic index of sesquiterpanes are developed for oil correlation and differentiation. Finally, a spill case using sesquiterpanes for source identification is presented.

EXPERIMENTAL

Approximately 0.4 gram of oils or petroleum products were weighed, dissolved in hexane and made up to the final volume of

5.00 mL. A 200 μ L of the oil solutions containing ~ 16 mg of oil was spiked with appropriate surrogates (100 μ L 200 ppm of o-terphenyl and 100 μ L of mixture of deuterated acenaphthene, phenanthrene, benz[a]anthracene, and perylene, 10 ppm each), and then transferred into a 3-g silica gel microcolumns, which was topped with about 1-cm anhydrous granular sodium sulfate and had been pre-conditioned using 20 mL of hexane, for sample cleanup and fractionation.

Hexane (12 mL) and 50% dichloromethane (DCM) in hexane (v/v, 15 mL) were used to elute the saturated and aromatic hydrocarbons, respectively. For each sample, the hexane fraction (labeled F1) was used for analysis of aliphatics, n-alkanes, and biomarker compounds; while 50% DCM in hexane fraction (labeled F2) was used for analysis of alkylated homologous PAHs and other EPA priority unsubstituted PAHs. The fractions were concentrated under a stream of nitrogen to appropriate volumes (~0.4 mL), spiked with appropriate internal standards (50 μ L of 200 ppm 5- α -androstane and 50 μ L of 20 ppm C_{30} - β -hopane for F1 and 50 μ L of 10 ppm terphenyl- d_{14} for F2, respectively), and then adjusted to an accurate pre-injection volume of 0.50 mL for GC-MS analyses (6, 7).

Analyses of target PAH compounds (including 5 alkylated PAH homologous groups and other EPA priority PAHs) and biomarkers were performed on an HP 6890 GC equipped with a HP 5973 mass selective detector (MSD). System control and data acquisition were achieved with an HP G1701 BA MSD ChemStation. The individual biomarker compounds were determined using GC-MS in the selected ion monitoring mode (SIM).

RESULTS AND DISCUSSION

Sesquiterpane Distributions. Generally, the bicyclic oil sesquiterpanes of interest to environmental forensic investigation are examined at m/z at m/z 123, 179 (the ion after sesquiterpane $C_{14}H_{26}$ loses CH_3), 193 (the ion after $C_{15}H_{28}$ loses CH_3), and 207 (the ion after $C_{16}H_{30}$ loses CH_3).

The sesquiterpanes ranging from C_{14} to C_{16} usually elute out between n- C_{13} and n- C_{16} in the GC-MS chromatogram. Peaks 1 and 2, peaks 3 to 6, and peaks 7-10 (**Figure 1**) are identified as C_{14} , C_{15} and C_{16} sesquiterpanes, respectively.

The distribution patterns of sesquiterpanes are, in general, different from oil to oil and from oil to refined products. **Figure 1** shows GC-MS chromatograms of sesquiterpanes at m/z 123 for representative light (API > 35), medium (API: 25-35) and heavy (API < 25) crude oils including Alaska North Slope (ANS), Arabian Light, Scotia Light oil (Nova Scotia), West Texas, and California API 11. **Figure 2** compares GC-MS chromatograms of sesquiterpanes at m/z 123 for representative petroleum products from light kerosene to heavy fuel oil.

The presence of common sesquiterpanes with the drimane skeleton in all studied oils is apparent. However, the oils from different sources demonstrate differences in both the absolute concentrations and relative distribution patterns of sesquiterpanes. The ANS, Arabian Light and Scotia Light display high concentrations of sesquiterpanes with the Peak 10 (C_{16} homodrimane) being the most abundant for the ANS and Arabian Light, and Peak 3 (C_{15} sesquiterpane) being the most abundant for Scotia Light, respectively. The Arabian Light has the lowest concentration of C_{14} sesquiterpanes (Peak 1 and 2), indicating this oil is highly mature. On contrast, the heavy California API 11 oil demonstrates the highest concentration of C_{14} sesquiterpane (Peak 1) among all sesquiterpane peaks, indicating that this oil may be still in the relatively immature stage.

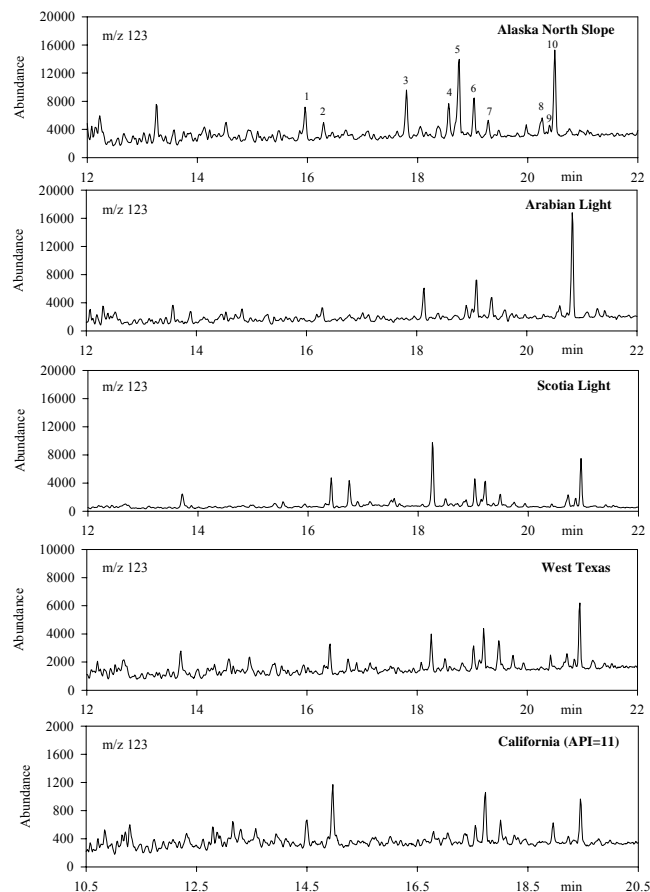


Figure 1. GC-MS chromatograms of sesquiterpanes at m/z 123 for representative light (API > 35), medium (API: 25-35) and heavy (API<25) crude oils including Alaska North Slope (ANS), Arabian Light, Scotia Light oil (Nova Scotia), West Texas, and California API 11

For petroleum products, sesquiterpanes are absent in very light Kerosene and heavy lubricating oils. However, the refined products IFO-180 and heavy fuel oil 6303 (Bunker C type) have relatively high concentrations of sesquiterpanes. It is noticed that one unknown bicyclic biomarker compound (between Peak 2 and Peak 3) is significantly abundant in these two products.

Effects of Weathering on Sesquiterpane Distributions. Biomarkers are source-characteristic and, in most cases, highly stable and degradation-resistant. Therefore, the sesquiterpanes are useful and promising for source correlation and differentiation of lighter refined products, in particular for the weathered refined products. In general, light to medium weathering has little effect on distribution pattern and diagnostic ration values of sesquiterpanes and diamondoids. **Figure 3** presents the relative GC-MS response (m/z 123) of ten sesquiterpanes (relative to Peak 3; that is, the response of Peak 3 = 1.00) in the Diesel No. 2 (2002, Ottawa Stinson gas station) at four weathering percentages: 0, 7.18, 14.20, and 21.95%. Indices of target sesquiterpanes in the weathered Diesel No.2 samples are also determined (not shown here). Clearly, no apparent depletion was observed for bicyclic sesquiterpanes. Almost all target sesquiterpanes were concentrated in proportion with the increase of the weathered percentages, resulting in that most sesquiterpane indexes remain constant for diesels from 0% to 22% weathered. However, some preferential loss of the lower

molecular weight and early-eluted C_{14} sesquiterpanes (Peaks 1 and 2) is observed as the diesel samples are further weathered.

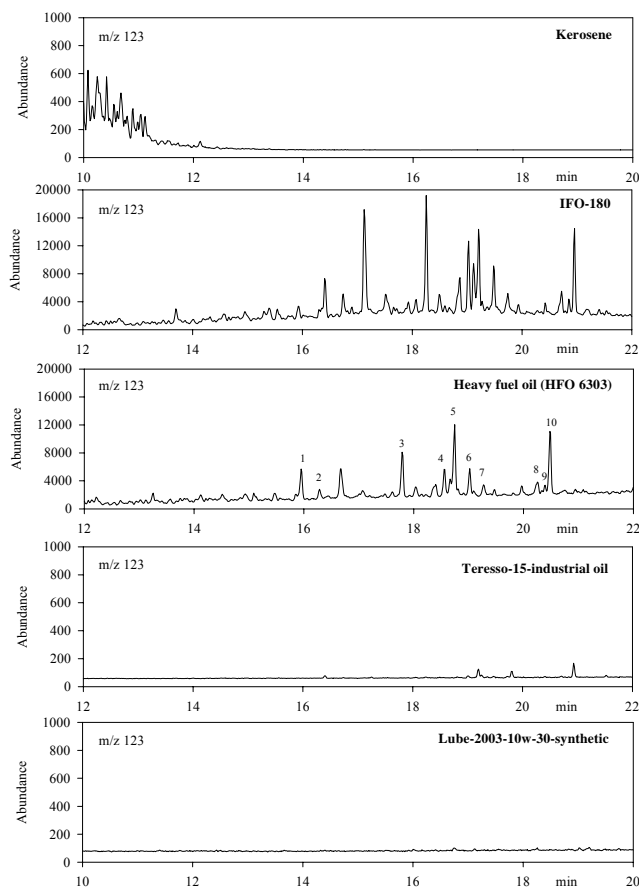


Figure 2. Comparison of GC-MS chromatograms of sesquiterpanes at m/z 123 for representative petroleum products from light kerosene to heavy fuel oil

Table 1. Diagnostic ratio values of selected sesquiterpanes determined from two representative 1998-spill-diesel and one suspected-source-diesel samples

Diesel samples	Spill sample I	Spill sample II	Suspected source
P5:P3	1.30	1.33	1.28
P10:P3	1.30	1.35	1.29
P8:P10	0.28	0.28	0.29
P2:P1	0.48	0.47	0.50
P1:P3:P5:P10	0.54:1.00:1.30:1.30	0.57:1.00:1.34:1.36	0.58:1.00:1.28:1.29

Using Sesquiterpanes for Spill source Identification.

Figure 4 shows the GC-MS chromatograms at m/z 123 for sesquiterpane analysis for a jet fuel, Diesel No.2 (2002, from an Ottawa Gas Station), Diesel No.2 (for 1994 Mobile Burn, 16.3% weathered), Diesel No.2 (2003, from Korea), 1998-spilled-diesel (from Quebec) and 1998-suspected-source-diesel (from Quebec). The Jet A is characterized with Peak 3, 5 and 1 being the most abundant, while the diesel (2002, Ottawa) is characterized with the Peak 10 being the most abundant and followed by Peaks 5 and 3. The difference of sesquiterpanes in distribution patterns and concentrations between three diesels (the Ottawa diesel, the

weathered diesel used for the 1994 Mobile Burn study, and the Korean diesel) and between diesels and the jet fuel are apparent.

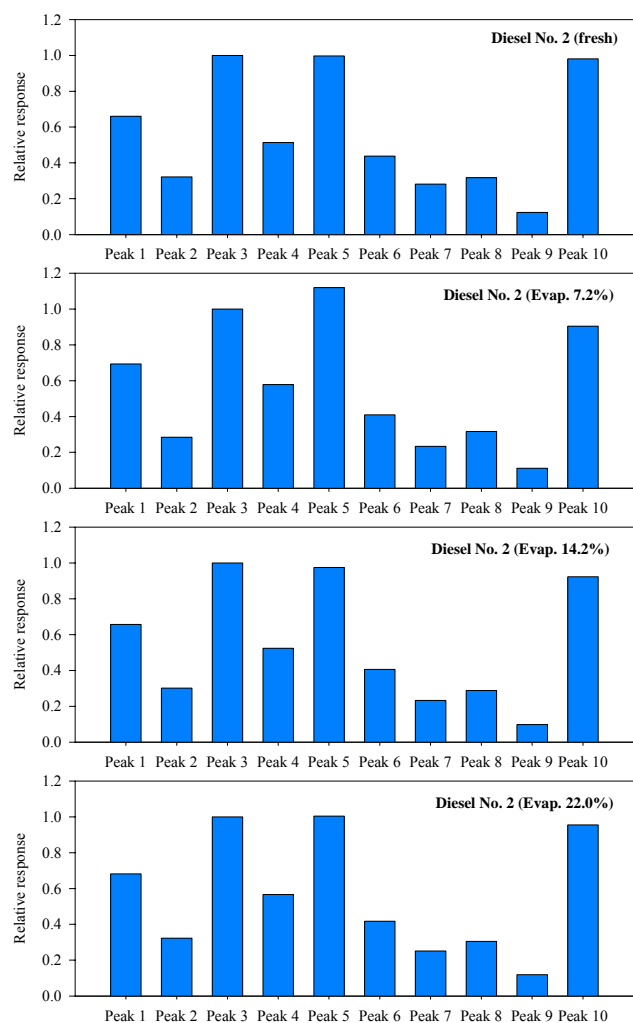


Figure 3. The relative GC-MS response (m/z 123) of ten sesquiterpanes (relative to Peak 3; that is, the response of Peak 3 = 1.00) in the Diesel No. 2 (2002, Ottawa Stinson gas station) at four weathering percentages: 0, 7.18, 14.20, and 21.95%.

As for 1998 Quebec spill samples (collected at a sewer outlet flowing into the Lachine Canal in Quebec), only very small amounts ($<10 \mu\text{g/g}$ oil) of low molecular weight $\text{C}_{19}\text{-C}_{24}$ tricyclic terpanes and regular $\text{C}_{20}\text{-C}_{22}$ steranes and trace of diasteranes were detected. However, these spill samples contain significant amount of sesquiterpanes. **Table 1** summarizes and compares diagnostic ratio values of selected sesquiterpanes determined from two representative 1998-spill-diesel and one suspected-source-diesel samples. **Figure 4** and **Table 1** clearly demonstrate that the spilled-diesel samples had very similar GC-MS chromatogram and nearly identical diagnostic ratio values of sesquiterpanes (at m/z 123) with the suspected-source diesel. The only difference noticed is that the spilled sample showed slightly higher abundances than the suspected-source-diesel sample because of weathering. These similarities, in combined with other hydrocarbon quantitation results (such as bulk hydrocarbon groups, n -alkane distribution, and fingerprints of alkylated PAHs and diagnostic ratios of source-specific PAH compounds), argued strongly that the spilled oil was a

diesel fuel, and the suspected diesel collected from the pumping station (very close to the spill site) was the source of the spilled diesel.

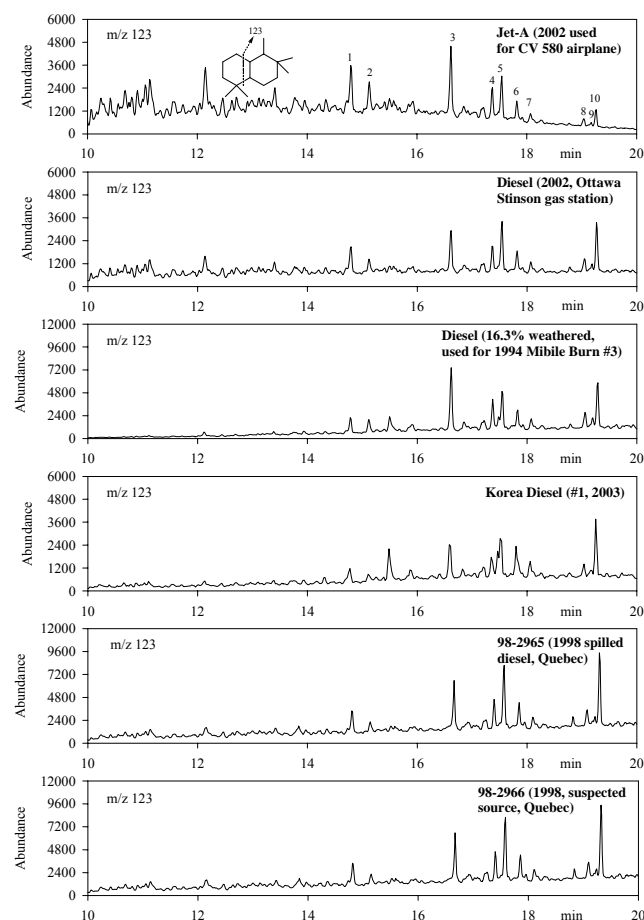


Figure 4. GC-MS chromatograms at m/z 123 for sesquiterpane analysis for a jet fuel, Diesel No.2 (2002, from an Ottawa Gas Station), Diesel No.2 (for 1994 Mobile Burn, 16.3% weathered), Diesel No.2 (2003, from Korea), 1998-spilled-diesel (from Quebec) and 1998-suspected-source-diesel (from Quebec)

REFERENCES

- Alexander, R., Kagi, R., and Noble, R., *J. C. S. Chem. Comm.*, 226-228, **1983**.
- Petrov, A. A., "Petroleum Hydrocarbons", 255 pages, Springer-Verlag, Berlin, Germany, **1987**.
- Noble, R. A., *Ph. D. Thesis*, Department of Organic Chemistry, University of Western Australia, 365 p, **1986**.
- Simoneit, B. R. T., Grimalt, J. O. And Wang, T. G., A review on cyclic terpanoids in modern resinous plant debris amber, coal, and oils, Annual research report of geochemistry laboratory, Institute of Geochemistry, Academia Sinica, People's Publishing House, Guizhou, China, **1986**.
- Chen, J., and He, B., *Organic Geochemistry*, 6, 561-567, **1990**.
- Wang, Z. D., Fingas, M., Li, K., *J. Chromatogr. Sci.*, **1994**, 32, 361-366 (Part I) and 367-382 (Part II).
- Wang, Z. D., Fingas, M., Sergy, G., *Environ. Sci. Technol.*, **1994**, 28, 1733-1746.

THERMOGRAVIMETRIC AND INFRARED CHARACTERIZATION OF ASPHALTENES PRECIPITATED FROM BITUMEN

Waldemar I. Friesen, Kirk H. Michaelian, Yicheng Long, and
Tadeusz Dabros

CANMET Energy Technology Centre–Devon
Natural Resources Canada
1 Oil Patch Drive, Devon, Alberta
Canada T9G 1A8

Introduction

Canada's oil sands are estimated to contain 1.7 trillion barrels of bitumen, of which 300 billion barrels are recoverable using current technology. Daily output presently stands at about one million barrels, which accounts for 25% of total Canadian production of conventional and heavy oil. It is projected that output will rise to five million barrels per day by 2030, enough to satisfy 20% of North American demand.

The processing of bitumen into a product that can be readily upgraded involves the treatment of bitumen froth, a highly viscous fluid typically containing 60% bitumen, 30% water, and 10% solids by weight. A recently developed process¹ dilutes the froth with an amount of paraffinic solvent above a critical ratio with respect to bitumen (*S/B*, wt/wt). The result is the formation of large clusters of solids, water, and precipitated asphaltenes that settle rapidly such that the bottom sediments and water content is reduced to less than 0.1%.²

Although the reduction of the asphaltene content in bitumen is advantageous for transport and upgrading, the cost is that potentially usable hydrocarbons are lost. Since oil sand bitumen contains from 16 to 25 wt% asphaltenes, a substantial fraction of the energy content of the original bitumen resides in the asphaltenes. Therefore, the advantage of improving the feedstock for upgrading must be weighed against the economic value of discarded hydrocarbon fuel when the optimal *S/B* for froth treatment is determined.

In this paper we report the results of a study of the asphaltenes precipitated by mixing hexane with Athabasca bitumen at *S/B* values from 1.1 to 3.5, a range that includes the ratio that would be used in an extraction plant. Thermogravimetric analysis (TGA) was used to measure the pyrolytic behaviour of the asphaltenes up to 1000°C and photoacoustic Fourier transform infrared (PA FT-IR) spectroscopy was used to characterize the asphaltenes.

Experimental

Sample Preparation. Clean and dry Athabasca bitumen was obtained by first diluting untreated bitumen froth with toluene in the ratio 1:3 (by weight). After the mixture had settled for 2 h, the supernatant was centrifuged to separate the water and solids. Vacuum rotary evaporation was then used to remove the toluene from the centrifuged supernatant.

The asphaltene content of the bitumen was measured to be 18.4 wt% using near-infrared spectroscopy.³ The bitumen was partially deasphalted by adding hexane in the ratios *S/B* = 1.1, 1.3, 1.7, 2.5, 3.5. The method used differed from the one prescribed by ASTM so as to crudely simulate the industrial process. Clean and dry bitumen was fully mixed with solvent at the desired *S/B* and centrifuged. Partially deasphalted bitumen (PDAB) was derived from the supernatant by using vacuum rotary evaporation to remove the solvent. Asphaltenes were obtained by repeated washing of the cake with solvent until the recovered solvent was clear, dissolving the cake in toluene, centrifuging the suspension to separate any remaining solids, and finally removing the toluene from the resulting supernatant by vacuum rotary evaporation. The asphaltene particles

were then ground manually to sizes of the order of 0.5 mm. The asphaltene contents of the PDAB samples, as measured by NIR spectroscopy, are given in Table 1.

Bitumen was also deasphalted completely (by definition) by dilution with *n*-pentane according to the standard ASTM method.

Thermogravimetric Analysis. A Mettler-Toledo TGA/SDTA-851^e module was used to analyze bitumen, asphaltene, and PDAB samples of about 15 mg each. The temperature was increased from 25°C to 150°C at a rate of 50°C/min and then to 1000°C at 10°C/min under an atmosphere of nitrogen flowing at 75 mL/min. At 1000°C, the nitrogen was replaced by air at a flow rate of 150 mL/min to allow combustion of any remaining hydrocarbons. The results from duplicate runs for each sample were averaged.

Photoacoustic FT-IR Spectroscopy. Photoacoustic infrared spectra of neat (undiluted) samples of asphaltenes were recorded using a Bruker IFS 113v FT-IR spectrometer and an MTEC 300 PA accessory. The asphaltene samples were contained in 6-mm cups, with nitrogen serving as the carrier gas in the PA cell. The spectra were measured at a resolution of 6 cm⁻¹, utilizing mirror velocities that correspond to modulation frequencies of 3.716 and 4.42 kHz at the HeNe laser wavenumber (15,800 cm⁻¹). In most cases twenty 50-sec spectra were averaged to produce the final spectrum.

Comparison of band intensities for the five asphaltene samples is based on the assumption that the particle sizes were about the same for all of the samples. The total intensity of a band was estimated by integrating the relevant interval above a suitably constructed baseline.

Table 1. Properties (in wt%) of PDAB and Asphaltenes at Various *S/B*

<i>S/B</i>	PDAB		Asphaltenes		
	Asphaltenes	Coke	V.M.	Coke	Ash
1.1	18.4	9.4	59.6	30.1	35.4
1.3	17.5	8.9	58.3	34.9	23.2
1.7	12.7	7.8	59.2	35.2	6.0
2.5	8.2	5.9	60.3	34.5	3.8
3.5	6.6	4.6	60.7	34.1	2.5

Results and Discussion

Thermogravimetric Analysis. Thermograms for bitumen and its pure maltene and asphaltene components (separated using *n*-pentane) are shown in Fig. 1. The bitumen and maltene masses began to decrease appreciably at 140°C with the onset of distillation, whereas no significant mass loss of the asphaltenes occurred below 300°C. The rates of mass loss were highest between 400°C and 490°C due to molecular decomposition. Mass losses were small above 525°C as the residue, semi-coke, was dehydrogenated into coke.⁴ At 1000°C, the coke was combusted in the air flow, leaving very small amounts of ash.

Figure 2 shows thermograms for the asphaltenes precipitated at various *S/B*. These curves are similar to the thermogram for whole asphaltenes in Fig. 1, except for the amount of ash remaining after combustion (Table 1). Subtracting the ash content from the total mass yields the thermal behaviour of the organic component of the asphaltenes. The fraction of the organic component volatilized

below 525°C (V.M.) and the fraction converted to coke at 1000°C are listed in Table 1 for the five asphaltene samples. We observe that V.M. is approximately 60 wt% for all samples; i.e., it is essentially independent of *S/B* and is approximately the same as the fraction measured for whole asphaltenes.

Photoacoustic FT-IR Spectroscopy. Figure 3 shows the 600–1900 cm⁻¹ and 2700–4000 cm⁻¹ regions for the asphaltene samples. The prominent features are labelled according to their origin: aromatic (ar), aliphatic (al), or clay. The clay bands closely resemble those in spectra of kaolinite, indicating that it is the predominant clay in the asphaltenes. The spectra clearly show that, as *S/B* increases, the intensities of the hydrocarbon bands increase while those of the clay bands decrease.

The variations of the aliphatic C–H intensity (2800–3000 cm⁻¹) and the aliphatic/aromatic (1350–1530 cm⁻¹/1530–1790 cm⁻¹) ratio with *S/B* were determined from the spectra. While the aliphatic intensity grows by about 80% as *S/B* increases from 1.1 to 3.5, the difference in the aliphatic/aromatic ratio is only about 6%. Estimates of the CH₂ and CH₃ contents obtained by integrating the 2880–2950 and 2950–3010 cm⁻¹ regions indicate that the CH₃ intensity increases by only 4% while the CH₂ intensity decreases by 3%. These results imply that increasing *S/B* causes the precipitation of asphaltenes containing slightly larger amounts of aliphatics, and that these hydrocarbons do not differ substantially.

The total intensity of the 900–1100 cm⁻¹ (clay) region decreases by a factor of 3.5 from low to high *S/B*. When the ratio of clay to hydrocarbon intensity (calculated from the aliphatic C–H region) is plotted against the ratio of ash to organic matter as measured by TGA, there is a strong positive correlation. This approximately linear relationship demonstrates the consistency of the TGA and FT-IR data.

Conclusion

TGA revealed that approximately 60 wt% of the organic material in each of the five samples was volatilized below 525°C, and that the asphaltenes differed primarily with respect to inorganic (clay and mineral) content, which decreased as *S/B* increased. These results are consistent with data obtained by photoacoustic FT-IR spectroscopy: the infrared intensities of CH₂ and CH₃ groups differed by only a few percent, and the infrared intensities of the clay bands varied inversely with *S/B*.

We conclude that the thermal treatment of these asphaltenes yields a significant fraction of their mass as potentially usable hydrocarbons and that any dependence of this fraction on *S/B* is small. Consequently, if asphaltene recovery is deemed to be a worthwhile step in the treatment process, *S/B* should be the minimal value that yields a bitumen product with properties satisfying upgrading requirements.

Acknowledgment. We thank T. Kratchmer for preparing the samples.

References

- (1) Tipman, R. N.; Long, Y. U.S. Patent 5 876 592, **1999**.
- (2) Long, Y.; Dabros, T.; Hamza, H. A. *Fuel* **2002**, 81, 1945.
- (3) Long, Y.; Dabros, T.; Hamza, H. A. *Can. J. Chem. Eng.* **2004**, in press.
- (4) Ritchie, R. G. S.; Roche, R. S.; Steedman, W. *Fuel* **1979**, 58, 523.

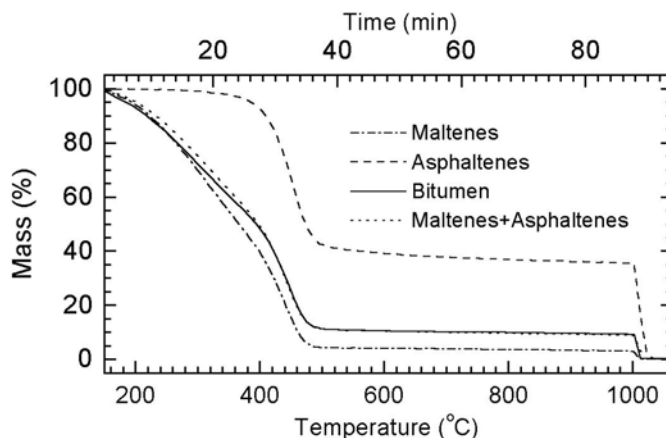


Figure 1. Thermograms for bitumen, maltenes, and asphaltenes precipitated by *n*-pentane

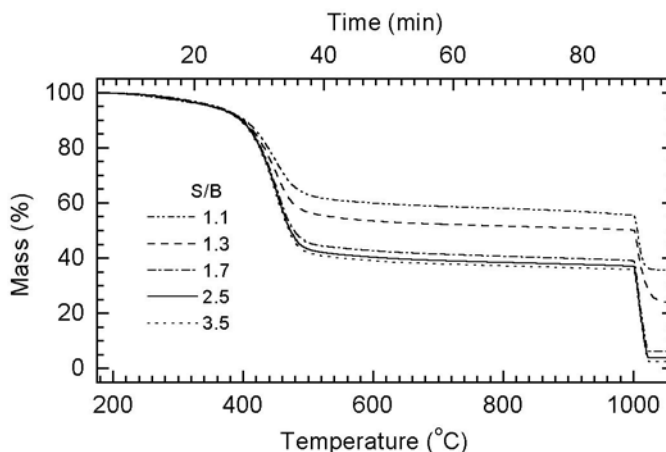


Figure 2. Thermograms for asphaltenes precipitated by hexane

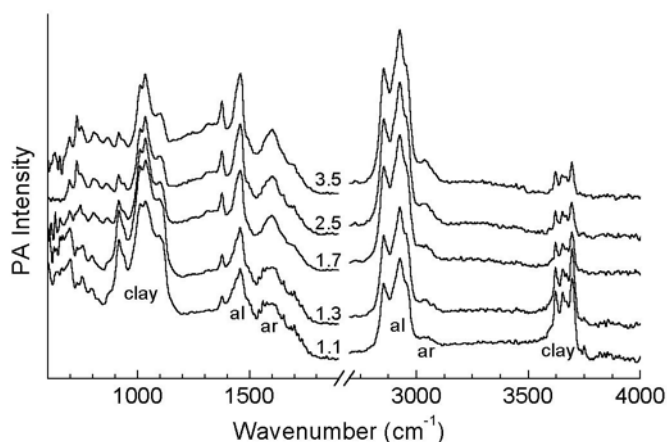


Figure 3. PA FT-IR spectra of asphaltenes

NEW ASTM METHOD FOR HEAVY FUEL OIL STABILITY

H. Buron¹, I. Cohen², J-A. Ostlund³

¹Formulation, 10 impasse Borde Basse, 31240 L'Union (France)

²Sci Tec, 726 Las Trampas road, CA 94549 Lafayette (USA)

³Ocel, PO Box 17, CH654HF Ellesmere Port (UK)

Introduction

The quality of heavy fuel oils is decreasing due to more severe conversion rates in the refineries around the world (1). In particular harder visbreaking increases the asphaltenes content in fuel oils. Asphaltenes are known to flocculate into particulates and are thought to be responsible for storage stability problems in heavy fuel oils (2,3). Sludge formation may cause severe problems in fuel tanks and may also result in incomplete combustion. When handling fuel oils, it is valuable to be able to know beforehand whether an oil is prone to form sludge or not. It is also important to be able to determine whether an oil can be upgraded by using additives, and whether the chosen additives are effective or not.

Experience from discussions with additive users has shown that more traditional methods, such as hot filtration, does not really explain the stability reserve of a fuel (4,5); it rather gives a hint about the amount and size of the asphaltenes aggregates that are present in the fuel. It does neither give any information about whether these molecules are dispersed in the oil. Ocel has therefore developed an in-house method using the Turbiscan that estimates the stability reserve of oils. It is also a valuable tool when checking and predicting the performance of additives. This method has recently been granted ASTM approval (D7061-04).

This paper describes the method used for estimating the stability reserve of oils. It also shows an example of a simulation scenario with sludge formation in a tank. It is shown from these results that aging of oils can be slowed down and prevented by the use of stabilizing additives. By combining such additives with combustion improves a boost in combustion characteristics may be obtained.

Experimental

In the test method ASTM D7061-04, oil is diluted with toluene and heptane is added. The phase separation rate upon addition of heptane is measured as a function of time using a Turbiscan.

The Turbiscan is a scanning device, where the reading head is composed of a pulsed near infrared light source (850 nm), and a transmittance detector situated at an 180° angle from the light source. Figure 1 shows a schematic picture of the measurement principle.

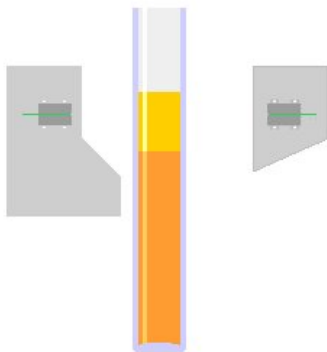


Figure 1. Measurement principle of the Turbiscan

The transmittance is recorded along the sample every 0.04 mm. By scanning the sample every minute the change in transmittance is

detected over time. The more rapidly it changes the more unstable the oil is regarded to be. One measurement is made every minute for 15 minutes. The deviation in transmittance between sixteen measurements is then calculated using the equation for standard deviation (see Eq. 1):

where X_i is the average transmittance (%) for each minute, X_T the average of X_i , and n the set of replicate measurements (16 in the method).

$$\text{Separability number} = \sqrt{\frac{\sum_{i=1}^n (X_i - X_T)^2}{n-1}} \quad (1)$$

The calculated value, the so-called separability number, is higher when the oil is destabilized and phase-separated. Hence, a high value indicates that the stability reserve in the oil is low and that there may be deposit problems within the oil. A low value of the separability number indicates that there is a good stability reserve within the oil.

Accordingly a scale has been determined from experience in the field. If the separability number is between 0-5, the oil can be considered to have a high stability reserve and asphaltenes are not likely to flocculate. If the separability number is between 5-10 the stability reserve in the oil is much lower. However, asphaltenes are in this case not likely to flocculate as long as the oil is not exposed to any worse conditions, such as storing, aging and heating. If the separability number is above 10 the stability reserve of the oil is very low and asphaltenes easily flocculate, or have already started to flocculate.

Simulation of storage of oils in a tank. Fuel oils were mixed with additives in small glass bottles. S1 and S2 are stabilizers and SC1 is a stabilizer plus a combustion catalyst. The bottles were provided with screw caps that were tight for liquid, but probably not totally gas tight and placed in a laboratory-heating oven at a temperature of 120 °C. The bottles were then removed from the oven every 24 h and 5 ml of the mixture was withdrawn each time for analysis using the procedure described above.

Results and Discussion

Illustration of the test method. Typical test results from measurements on two oils are shown in Figure 2 a and b.



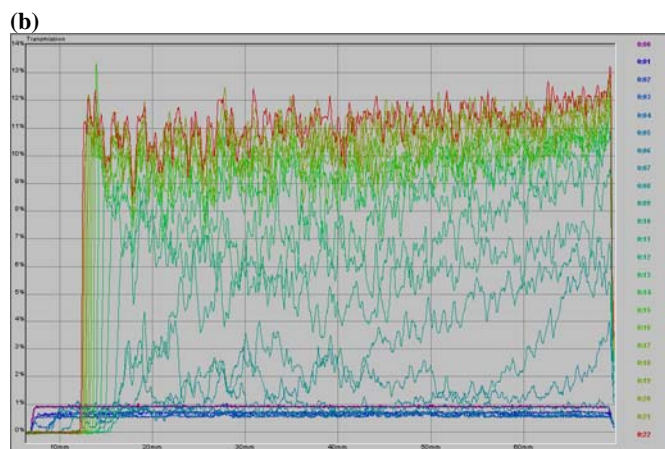


Figure 2. (a) Results from a Turbiscan measurement of an oil with a separability number of 1. (b) Results from a Turbiscan measurement of an oil with a separability number of 12. The transmittance is measured, every 0.04 mm once per minute, along the tube with sample.

It can be seen that the change in transmittance along the tube is changing much more rapidly and much more distinctly in graph 2 b, compared to graph 2 a. The top sample is showing an oil with a low separability number. The bottom graph shows the results from an unstable oil, which phase separates quickly (high separability number).

Simulation of oil storage in a tank. Shown below are results from treated and untreated fuel oil samples that have been aged in an oven.

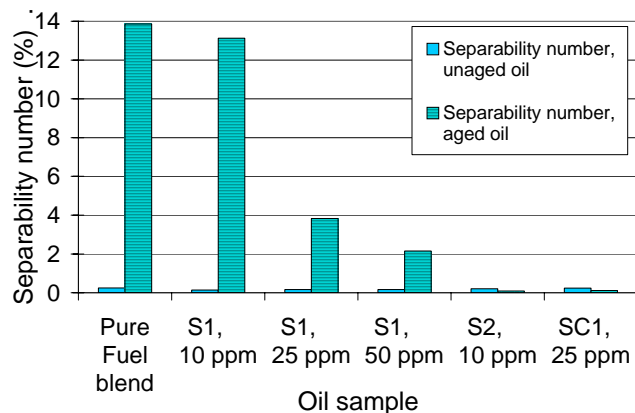


Figure 3. Separability number for fresh fuel oil blends compared to aged blends. The results in the first column are of untreated oils and the others have been treated with additives. The samples were aged for 1 week at 120 °C.

It can be seen that the stability reserve of the oil is worsened upon storage in an oven for one week. If the oil is treated with stabilizers (S1 and S2) or with an additive consisting of a stabilizer combined with a combustion catalyst the separability number remains low, indicating that the stability reserve of the oil remains intact.

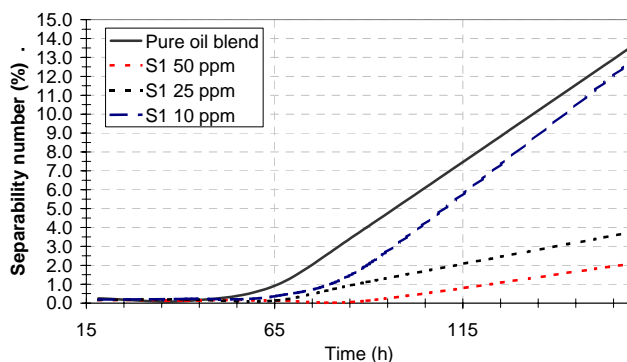


Figure 4. The change in separability number over time for the pure oil blend and for samples containing additive S1 (at various levels).

The results in Figure 4 show that the stability reserve of a fuel oil decreases during storage. During one week of storing at 120 °C the pure fuel oil blend is degraded from being a fuel oil with a high stability reserve and a separability number of 0.3, to becoming a very unstable fuel with a separability number of 13.9. The refinery that produced the fuel oil reported that they experienced degradation of the fuel after about 5 days of storage, which correlates well with the results obtained in this study. Upon addition of stabilizing additive (S1), this process was slowed down. It is seen that, while the pure fuel was starting to become unstable already after 55 h, the mixture containing additive 50 ppm of the additive S1 remained stable also after 75 h. It is interesting to note that the increased dosage of S1 extends the time before degradation of the oil starts, which means that the additive has a stabilizing effect on the fuel. The dosage level, however, is critical for optimal benefit. It is also worth noting that a rather low dosage rate was needed, to obtain a benefit from the additive. This is most certainly due to the oil being a rather good one from the beginning.

Conclusions

This paper was aimed at explaining the Octel test method (ASTM D7061-04) and demonstrating an example of its usefulness. Specific applications are suggested, such as estimating the oil quality before bunkering and to evaluate the benefit of additives for upgrading fuel oils. It is worth noting that with common storage temperatures in the range of 50 to 80 °C, fuel oils may be destabilized already after a few days due to the heat. Such a scenario was simulated and destabilization of oils was seen to be prevented by the use of Octel additives. Measuring and monitoring the stability of the fuel oils with the Turbiscan is vital for avoiding stability problems (which may result in sludge formation in the bottom of oil tanks). The method may also be used for determining appropriate additives that can hamper negative instability effects.

References

- (1) Park, S.J.; Mansoori, G.A.; *Energy sources* **1988**, *10*, 109-125.
- (2) Taylor, S.E. *Fuel*, **1992**, *71*, 1338-1339.
- (3) Rassamdana, H.; Dabir, B.; Nematy, M.; Farhani, M.; Sahami, M. *AIChE*, **1996**, *42*, 10-22.
- (4) Buckley, J.S. *Fuel Sci. Technol. Int.*, **1996**, *14*, 55-74.
- (5) Carbognani, L.; Espidel, J.; Izquierdo, A. *Asphaltenes and Apshalts : Developments in Petroleum Science*; 1999, Yen, T.F.; Chilingarian, G.V. Eds; Elsevier Science B.V.

RELIABLE METHOD FOR DETERMINING PLASTICITY AND RANK OF COAL BY DIELECTRIC PROPERTY MEASUREMENT

Tetsuo Aida, Toyokazu Shinkai, Kiyonori Murakami,
and Paul G. Aida*

Department of Biological & Environmental Chemistry,
School of Humanity-oriented Science & Engineering,
Kinki University,
JAPAN

* Department of Agriculture, The University of Tokyo, JAPAN

Introduction

Coal contains many chemically reactive oxygen-functionalities such as hydroxyl (i.e., phenolic and alcoholic), carboxylic, carbonylic or etheric functionality which are capable to form relatively weak bonding interaction between the macromolecular network chain-structure such as a hydrogen bonding, and are thought to control the physical and chemical property of coal. Because of their polar characteristics, the nature of the molecular association must be reasonably reflected on the dielectric property.

The strategic scheme of our research project to develop a new methodology is illustrated in **Figure 1**. Namely, the measurement of dielectric property of polymeric substance such as coal under the elevated temperature condition will give us valuable information to understand the macromolecular network structure based on the polarity and mobility.

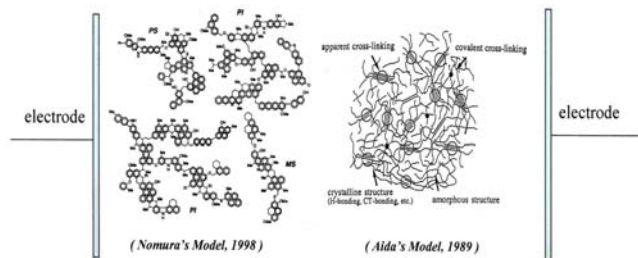


Figure 1. Strategic scheme for studying macromolecular network structure coal by dielectric property measurement

In this paper, we will present the recent progress of our research concerning the development of a reliable method for characterizing the macromolecular network structure of coal with the dielectric property.

Experimental

Coal Samples and chemicals. The Argonne Premium Coal Samples (> 100 mesh) were used in this research, simply because of the reasonable quality, which were dried under vacuum at room temperature overnight and stored under nitrogen atmosphere, in order to minimize the unnecessary effect on the chemical and physical property of coal by heating and oxidation. Commercially available polyethylene terephthalate (PET) was used after dried under vacuum at room temperature overnight as the model compound.

Instrument and Procedure: Dielectric property measurement was carried out by means of the instrument composed by ourselves, which are capable to handle not only liquid sample, but also gaseous and solid samples with a wide range of frequencies (10mmHz to 1.0MHz). A typical procedure for measuring the capacitance of coal sample is as follows: Coal was thoroughly ground by using mortar, and then shaped as a disk (diameter: 10mm, thickness: 0.2mm) by using a 1 ton handy-press, and which was sandwiched between the

electrode under Ar-atmosphere in quartz tubing electric furnace. The capacitance of coal was measured under elevated temperature with 5.0 °C / min. rate.

Results and Discussion

We have investigated whether this method is capable to determine a delicate molecular interaction generated phase transition phenomena in the macromolecular network structure like a glass-transition and melting of polymeric substance by using model polymer.

Figure 2 shows the capacitance of polyethylene terephthalate (PET) measured as a function of temperature, of which glass-transition temperature and melting temperatures are already known as 81°C and 265°C, respectively.

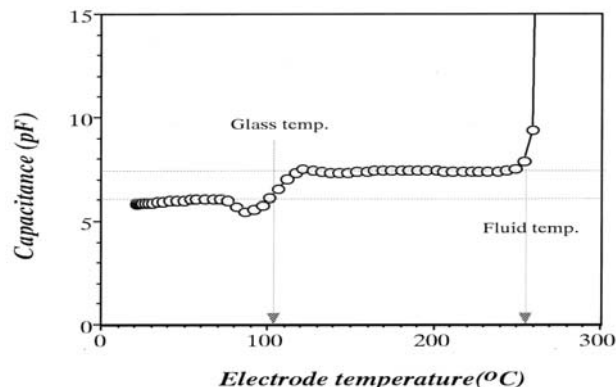


Figure 2. Thermal behavior of dielectric property of PET

Expectedly, those literature values were consisted with the temperature determined on the characteristic capacitance pattern shown in this figure. At the same time we can get very valuable information concerning the polarity between the glassy phase-transition as a capacitance, indicating that the higher temperature macromolecular phase will be more polar than that of lower temperature one.

We have conducted a series of experiment using the Argonne Premium Coal Samples, based on the result of the preliminary experiment described above.

Figure 3 demonstrates as a typical example of the dielectric property measurement of Illinois No. 6 coal.

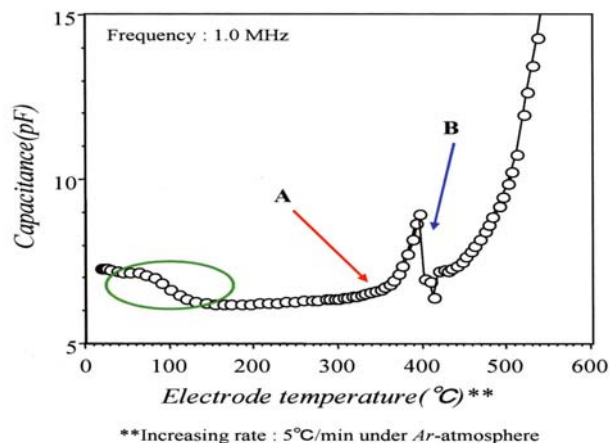


Figure 3. Thermal behavior of dielectric property of Illinois No. 6 coal.

There are some interesting features in this figure, comparing with the case of PET. Particularly, the sharply declining change (B) of the capacitance appearing around 400°C is very impressive and mysterious. In order to understand the mechanism of these phase transitions, it will be helpful to compare the literature data⁽¹⁾ concerning the plasticity of coal determined by the *Gieseler's plastometer* which are available in the *Users Handbook for the Argonne Premium Coal Sample*, the initial softening temperature and fluidized temperature of Illinois No.6 coal are 367 °C and 417 °C, respectively. Obviously, these values are identical to those determined from the pattern (A and B) in **Figure 3**. This fact may be strongly suggesting that this method will be more reliable than ever in terms of its physical meanings.

We have also learned that this particular capacitance pattern can be used as a fingerprint of coal.

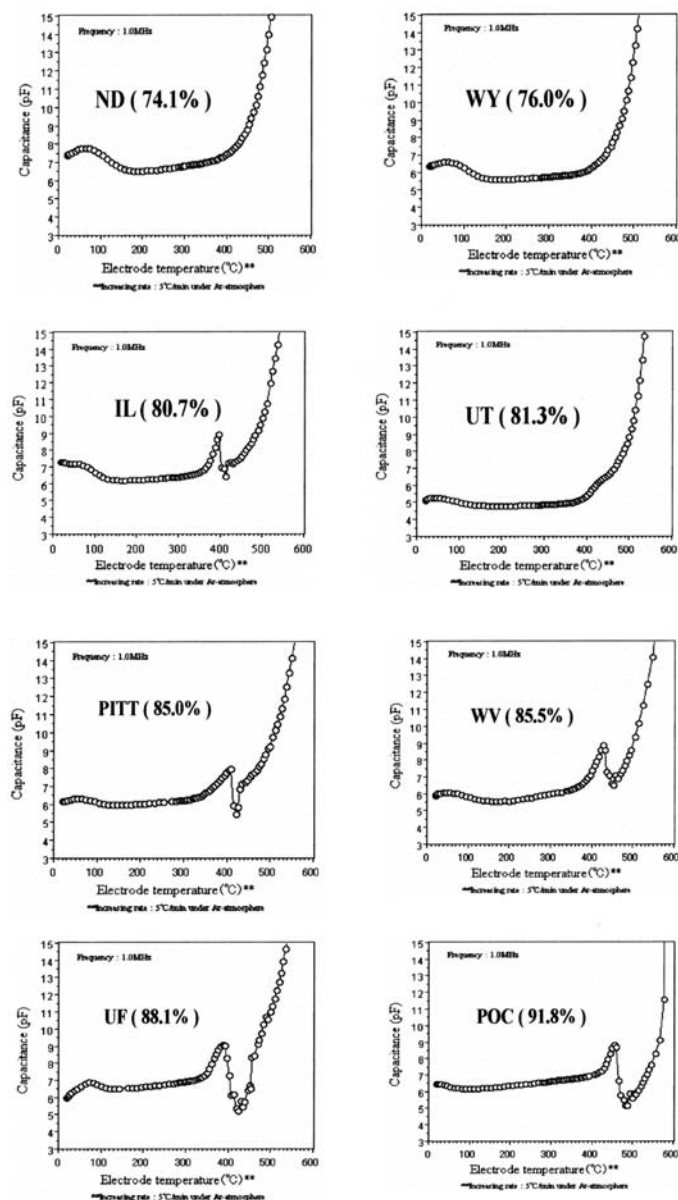


Figure 4. Coal Rank (C-cont. %) dependence of thermal behavior of dielectric property

In **Figure 4**, the coal rank dependency on the dielectric behavior is demonstrating with experimental data obtained from all of *Argonne Premium Coal Sample*. The most striking feature on these data will be that the coal rank seems to depend upon the peak between the Point-A and B demonstrated in **Figure 3**. Namely, this peak can not observe in the lower rank coal like a lignite (ND and WY), and those of the higher rank coal seem to be shifted to higher temperature range, suggesting that the coalification process is depending on the macromolecular chain orientation (secondary cross-linking formation) based on such cohesive force as hydrogen bonding, charge-transfer bonding etc. As far as our data, the rank between IL and UT must be replaced each other.

In order to elucidate the role of hydrogen bonding interaction in the macromolecular network structure, we have initiated a series of controlled experiment. In **Figure 5**, the effect of methylation of hydroxyl functionality of Illinois No.6 coal, which was carried out by using the O-methylated coal sample performed by means of *Liotta's* method.⁽²⁾ The content of carboxylic acid functionality and phenolic hydroxyl functionality after the methylation were determined by chemical method recently developed by us⁽³⁾ as 95% range of completion.

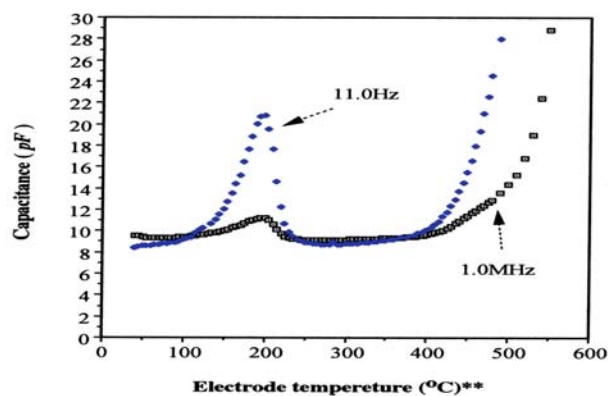


Figure 5. Effect of methylation of hydroxyl functionality in Illinois No.6 coal on the dielectric property

Very interestingly, the methylated coal could not generate the characteristic peak at around 400 °C any more, and instead of it a new peak appeared at around 200 °C. These behaviors observed on the capacitance seem to be consistent with the disappearance of molecular association due to hydrogen bonding by methylation, and the appearance of relatively weak molecular association due to *van der Waals* force between the methoxyl functionality in coal accompanying with the different sensitivity towards frequency on the new peak. The detailed explanation about the effect of frequency will be discussed in our presentation.

Acknowledgement

A part of this work was supported by the Japanese Government through the 148 Committee of the Japan Society for the Promotion of Science.

References

- (1) K.S. Vorres, *Users handbook for the Argonne premium coal sample*, 37(1993)
- (2) R. Liotta, K. Rose, and E. Hippo, *J Org. Chem.*, **46**, 277(1981)
- (3) T. Aida, et al., *Prepr.-Pap, Am. Chem. Soc., Div. Fuel Chem.*, **47**,723(2001)